MULTIFERROIC COFE2O4-PB(ZR0.53TI0.47)O3 THICK FILMS FOR MAGNETOELECTRIC APPLICATION

CHEN WEI

SCHOOL OF ELECTRICAL & ELECTRONIC ENGINEERING

A thesis submitted to the Nanyang Technological University in fulfillment of the requirement for the degree of Doctor of Philosophy

2012-5-18

ACKNOWLEDGMENTS

First and foremost, I would like to express my deep and sincere gratitude to my supervisor, Professor Zhu Weiguang. His wide knowledge and his logical way of thinking have been of great value for me. Professor Zhu, with an unselfish personality, has good knowledge and high standards, and also has a scientific and responsible attitude on research works. It is greatly beneficial for me in my PhD study and research work, in my career and in my future life.

In addition, I also highly appreciate Professor Tan Ooi Kiang for his support and help when I need them most. Most importantly, his way of flexibility and easy-going makes me more confident and comfortable.

I wish to thank Dr. Sun Lingling for her much assistance on my initial research work. Thank Dr. Wang Zhihong, Dr. Kong Lingbin and Dr. Chen Xiaofeng for their valuable advice.

I wish to express my appreciation for the help provided by all my colleagues. The assistance provided by all the technical staff of Sensors and Actuators Laboratory is highly appreciated.

Finally, I owe my loving thanks to my wife Zhang Zhuan for her understanding and support all the time, which motives me to go to today.

TABLE OF CONTENTS

SUMMARY

Recent theoretical breakthroughs in understanding the concurrence of magnetic and electrical ordering, combined with advances in thin film growth techniques and experimental methods for observing magnetic and electric domains, have generated a flurry of research activity on magnetoelectric (ME) multiferroics [1, 2]. Theoretical studies have shown that the usual atomic-level mechanisms driving ferromagnetism and ferroelectricity are mutually exclusive, because they require partially and empty filled transition metal orbitals, respectively [3]. This recognition has prompted a search for alternative ferroelectric mechanisms that are compatible with the occurrence of magnetic ordering. As a result, previously unknown multiferroic materials have been discovered.

In the past few years, combining ferromagnetism and ferroelectricity in one material and coupling between ferromagnetism and ferroelectricity were two big challenges in multiferroics. With the developments in magnetoelectricity (ME) theory and the renovation of deposit technique, multiferroic $CoFe_2O_4$-$Pb(Zr_{0.53}Ti_{0.47})O_3$ (CFO-PZT) system is experiencing a renaissance recently due to its attractive ME effect and potential applications in multifunctional devices. However, much attention has been paid on CFO-PZT thin films and their bulk ceramics. The exploration on multiferroic thick films was nearly being on vacuum, which severely restricted the development of multiferroic materials on micro-electro-mechanical systems (MEMS) applications. In the present thesis, we are aiming to investigate the CFO-PZT

thick films comprehensively, especially focusing on their ME coupling development, so as to find their possible applications on MEMS devices. A series of works along this direction are hence presented as three main parts in this thesis.

Screen printing method has been attempted to fabricate CFO-PZT composite thick films. This is a simple and cost-saving method which has been widely applied in industry and research lab. With this method, CFO-PZT composite thick films were fabricated on alumina substrate at a low sintering temperature with thicknesses up to hundreds of micrometers. The ferromagnetic and ferroelectric properties of these thick films were characterized. However, the porosities of these thick films degraded severely their ferroelectric properties and lowered the potential ME coupling effect. Hence, we had to develop another method to prepare CFO-PZT composite thick films.

A hybrid sol-gel processing has been developed to deposit CFO-PZT composite thick film. This method inherently has advantages in making biphasic nanocomposites which exhibit concurrent ferromagnetic and ferroelectric properties. Before preparing the CFO-PZT composite thick films, pure CFO thick films realized by this method are studied in the second part, which includes the preparation of nano-sized CFO particles, synthesis of CFO sol-gel solution, and proper combining of CFO nanoparticles and sol-gel solution for uniform CFO slurry as well as the deposit tips by spin coating technique. 10 μm of cobalt ferrite composite thick films were deposited on platinum covered silicon wafers via this hybrid sol-gel processing. Phase structures revealed a critical annealing temperature above which the pure spinel

phase was obtained. The measurement of magnetization versus magnetic field demonstrated a saturated magnetization and coercive magnetic field comparable to those of a CFO thin film deposited by other chemical or physical techniques. A more interesting phenomenon was observed in their impedance spectra, where a dielectric relaxation behavior, similar to those noticed in manganese and nickel ferrites bulk materials, had been studied through frequency and temperature dependence of impedance spectra, electrical modulus, dielectric spectra and AC conductivity spectra. Ion motion and jump mechanism in cobalt ferrite thick films were investigated and discussed in detail.

The last part presents the preparation of CFO-PZT multiferroic composite thick films, including their fully characterizations, mechanisms analysis, consistent optimization and applications evaluation. A hybrid sol-gel process was adopted to deposit CFO-PZT composite thick films. Thick films in the desired thickness range (3~5 μm), along with a concurrence of ferromagnetic and ferroelectric properties, were achieved. Subsequently, we studied the effect of polyvinylpyrrolidone (PVP) on microstructures, ferromagnetic, and ferroelectric properties of CFO-PZT composite thick films. It was observed that PVP benefited to enhance the film thickness remarkably and avoid the cracks probably induced by different thermal expansion coefficients or lattice mismatch between different materials. However, the disadvantage of PVP was that it diluted the ferroelectric properties and reduced the ME coefficients of the composite thick films. To deal with this issue, PZT sol infiltration was introduced to enhance the ferroelectric and dielectric properties of the composite thick films. It was found that enough sol infiltration between slurry

layers dramatically improves the densification of the microstructure as well as the ferroelectric and dielectric properties. Through further combining PVP and sol infiltration, ferromagnetic properties were also promoted. With a dense microstructure and enhanced ferroelectric and ferromagnetic properties, a strong ME effect was expected in CFO-PZT composite thick films. Furthermore, dielectric studies of CFO-PZT thick films were conducted in detail. Dielectric relaxation was observed in multiferroic system and its physical mechanism was investigated.

LIST OF FIGURES

LIST OF TABLES

CHAPTER 1 INTRODUCTION

1.1 MOTIVATION

Magnetic and electronic materials permeate every aspect of modern technology [2]. For example, the vast amount of data generated by consumer electronic products is often stored as regions of opposite magnetic polarization in ferromagnets (materials with a spontaneous magnetic polarization that can be reversed by a magnetic field). The sensors industry relies heavily on a related class of materials known as ferroelectrics (materials with a spontaneous electric polarization that can be switched by an applied electric field). Many ferroelectrics are also ferroelastic—that is, a change in their electric polarization is accompanied by a change in shape. As a result, they are used to convert sound waves into electrical signals in sonar detectors, and to convert electrical impulses into motion in actuators. Such materials, which combine two or more "ferroic" properties in the same phase, are known as multiferroics [4].

The term multiferroic was first used by H. Schmid in 1994 [4]. His definition was referred to multiferroics as single phase materials which simultaneously possess two or more primary ferroic properties. Today the term multiferroic has been expanded to include materials which exhibit any type of long range magnetic ordering, spontaneous electric polarization, and/or ferroelasticity, as can be seen in Figure 1-1.

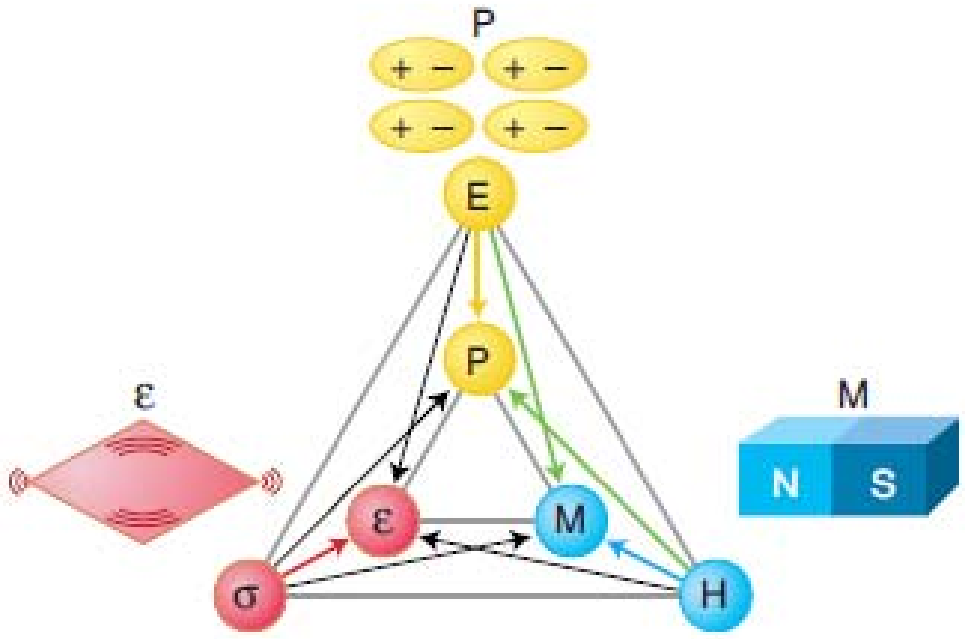

Figure 1-1 Phase control in ferroics and multiferroics. The electric field *E*, magnetic field *H*, and stress σ control the electric polarization P, magnetization M, and strain ε, respectively. In a ferroic material, P, M, or ε are spontaneously formed to produce ferromagnetism, ferroelectricity, or ferroelasticity, respectively. In a multiferroic, the coexisitence of at least two ferroic forms of ordering leads to additional interactions. In a magnetoelectric multiferroic material, a magnetic field may control P or an electric field may control M (green arrows) [2].

Working under this expanded definition the history of magnetoelectric (ME) multiferroics can be traced back to the 1960s [5]. In the most general sense the field of multiferroics was born from studies of ME systems. After an initial burst of interest, research remained static until early 2000. In 2003 the discovery of large ferroelectric polarization in epitaxially grown thin films of $BiFeO_3$ [6] and the discovery of strong magnetic and electric coupling in orthorhombic $TbMnO_3$ [7] and $TbMn_2O_5$ [8] re-stimulated activity in the field of multiferroics, as can be seen in Figure 1-2.

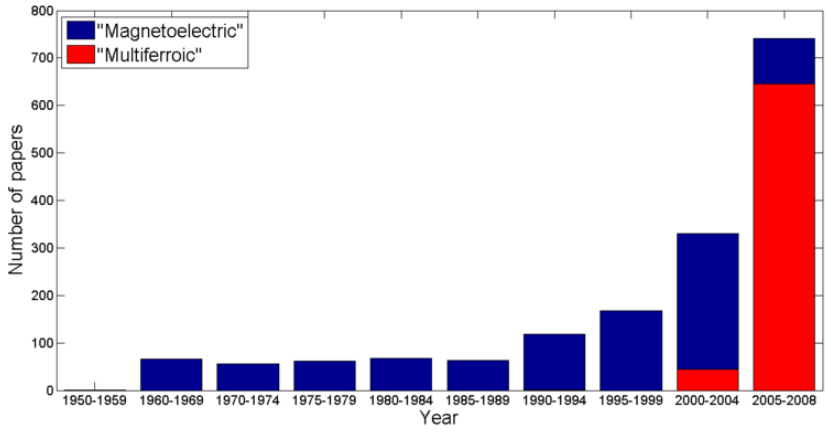

Figure 1-2 Number of papers from 1950-2008 using keywords magnetoelectric or multiferroic (as cited by Web of Science).

From the view of material constituents, multiferroic ME materials can be divided into two types: single-phase [9, 10] and composite [11]. In the past ten years, multiferroic materials with the coexistence of at least two ferroic orders [ferroelectric, (anti-)ferromagnetic, and ferroelastic] have drawn ever-increasing interest due to their potential applications as multifunctional devices [1, 4, 12]. Furthermore, these new multiferroics were in turn proving to be a rich source for exploring the fundamental science of phase control and ME interactions. In multiferroic materials, the coupling interaction between the different order parameters can produce additional functionalities, such as a ME effect, which was discovered more than a century ago [1]. The ME effect has been observed as an intrinsic effect in some natural material systems, which have been under intensive study recently [9, 10, 13], motivated by potential applications in information storage, spintronics, and multi-state memories. For example, huge ME effects have been observed recently in the form of ferroelectric phase transitions induced by magnetic fields in perovskite

manganites [7] and ferromagnetism induced by electric fields in hexagonal manganites [13]. ME memory effects and magnetic switching of ferroelectric domains (and the converse process) have been demonstrated. An optical technique has been developed that allows separate access to both concurrent domain structures of a multiferroic in the same experimental setup; with this method, coupling between magnetic and electric domains has been observed [1].

So far, over ten different compound families have been widely investigated as multiferroic ME materials such as well-known $BiFeO_3$ (BFO) and rare-earth manganates [14, 15]. Although the intrinsic ME effect exists in the single-phase compounds, most multiferroic compounds exhibit low Curie temperatures (below room temperature), and a high inherent ME coupling (especially above room temperature) has not yet been found in the single-phase compounds. Among them, $BiFeO_3$ is unique with high Curie and Neel temperatures far above room temperature, and thus most widely investigated in recent few years [16]. However, $BiFeO_3$ is G-type antiferromagnetic or only very weakly ferromagnetic. The low critical temperatures and/or weak ME coupling of the single-phase compounds hinder their practical applications.

Since none of the existing single phase multiferroic materials combine large, robust electric and magnetic polarizations at room temperature, the difficulties associated with uniting electrical and magnetic ordering in a single phase have been circumvented by forming two-phase composite multiferroics that consist of a ferroelectric constituent and a ferromagnetic constituent [17]. In such composites, the ME effect arises from the interaction of the elastic components of the ferromagnetic and ferroelectric constituents. An electric

field induces strain in the ferroelectric; this strain is then passed on to the ferromagnet [18], where it causes magnetization (vice versa), as can be seen in Figure 1-3.

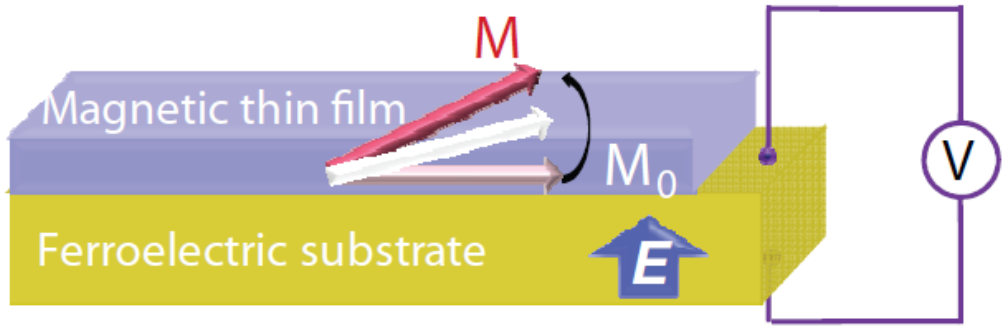

Figure 1-3 Schematic illustration of the electric field induced magnetization switching in a 2-2-type heterostructure with a magnetic thin film grown on a ferroelectric substrate. M_0 denotes the initial in-plane magnetization orientation, and M indicates the magnetization reorientation away from the in-plane with an electric field e applied across the ferroelectric layer.

In a crude way the ME effect displayed by this type of composite can therefore be written as [11]:

$$Direct\,ME_H\,effect = \frac{magnetic}{mechanic} \times \frac{mechanic}{electric} \qquad (1\text{-}1)$$

$$Converse\,ME_H\,effect = \frac{electric}{mechanic} \times \frac{mechanic}{magnetic} \qquad (1\text{-}2)$$

This is a coupled electrical and magnetic phenomenon via elastic interaction. Thus, the ME effect in composites is extrinsic, depending on the composite microstructure and coupling interaction across magnetic-piezoelectric interfaces. In comparison with single-phase multiferroic ME materials, the large ME response at room temperature can be achieved in the

ME composites, though the ME effect in the composites is extrinsic. As can be seen in Table 1-1, it summarizes some current ME bulk composites.

Table 1-1 Some ME bulk composites and their ME coefficients.

ME Composite	ME coefficient (mV/(cm·Oe))	Reference
NZFO/PZT	155 @ 1 kHz	[19]
NCZF/PZT/NCZF	782 @ 1 kHz	[20]
Terfenol-D/PMT-PT	10.3×10^3 @ 1 kHz	[21]
Terfenol-D/PVDF	1.43×10^3	[22]
FeBSiC/PZT-fiber	22×10^3 @ 1 Hz	[23]
FeBSiC/PVDF	21.46×10^3 @ 20 Hz	[24]
FeCoSiB/AlN	3.1×10^3 @ 1 Hz	[25]
CFO/P(VDF-TrFE)	40 @ 5 kHz	[26]

Thus the appearance of the ME composites made the practical applications by utilizing the ME effects in materials becomes true [19-46]. Due to technologically viable ME response observed in multiferroic ME composites above room temperature, various ME composites in different systems have been investigated in recent years, from bulk materials to thin films. A large number of combinations of ferroelectric oxides and magnetic oxides were chosen to get bulk ME ceramic composites usually via co-sintering at high temperature [19, 20]. Although bulk ME ceramic composites were considered to exhibit promising larger ME effect, the ME effect so far observed in high-temperature co-fired ceramic composites was about ten times or more lower than that predicted, mainly due to their inherent preparation problems, such as atomic interfacial inter-diffusion and reaction problems during high temperature processing.

Compared with bulk ME composites, multiferroic composite thin films have unique superiorities. Different phases could be combined at atomic-level,

and by precise control of the lattice matching, epitaxial or superlattice composite films can be designed, facilitating understanding of ME coupling at atomic scale [47]. So far, a number of multiferroic ME thin films of ferroelectric [e.g., BTO, $PbTiO_3$ (PTO), PZT, and BFO] and magnetic [e.g., CFO, NFO, Fe_3O_4, LSMO, and metals] with different nanostructures have been prepared via physical deposition technique and chemical processing. However, several questions in multiferroic thin films remained to be answered. For example, what happens in the ME composite films which could suffer large constraint from a stiff substrate? Is the ME coupling still strain-mediated as in the bulk composites? How can we get a large ME response from a ME thin films?

To reduce the effect from substrate and keep a strain-mediated ME effect, we are going to focus on multiferroic composite thick films, which have been much less studied compared with multiferroic bulks and thin films. It is known that the piezoelectric thick films, in particular those with thickness in the range of 3~10 μm, are still the important candidates in piezoelectric MEMS devices [48, 49]. The success in fabricating multiferroic thick films would stimulate the potential applications on multifunctional MEMS devices. Furthermore, compensating the gap between bulk ceramics and thin films is also a big challenge in multiferroic field.

In this thesis, we chose $CoFe_2O_4$ (CFO) and $Pb(Zr_{0.53}Ti_{0.47})O_3$ (PZT) as ferromagnetic and ferroelectric phase of multiferroic thick films, respectively. This is because of the high magnetostriction constant of CFO and large piezoelectric coefficient of PZT [11, 50-54]. They are able to achieve extrinsic

magnetoelectricity depending on the composite microstructure and interaction across magnetic-piezoelectric interfaces [55]. Followed by this, a hybrid sol-gel processing, which was used for preparing PZT composite thick films [56], was introduced to synthesize the CFO-PZT multiferroic thick films. It is known that the premise for a ME effect is holding the strong ferromagnetic and ferroelectric properties in multiferroic materials as well as a dense microstructure [57, 58]. Therefore, the achievement of large ferromagnetic and ferroelectric properties would be the main objective in this thesis.

1.2 OBJECTIVES

In this thesis, the primary goal was to fabricate CFO-PZT multiferroic composite thick films for potential ME application. The thesis includes the development of deposition techniques of multiferroic thick films as well as the continuous optimizations on structure and multiferroic properties, followed by detailed studies on their structure characterization and property analysis. Furthermore, the physical mechanisms for the observed phenomenon are analyzed and the feasibility of multiferroic thick films for ME application is discussed. Before proceeding to multiferroic thick films, pure CFO composite thick films were investigated, including their fabrication and property characterization. Interesting electrical relaxation and conductive mechanism observed in CFO thick films were also analyzed. In a word, this thesis was directed towards four primary objectives:

1. Attempt of screen printing method to prepare CFO-PZT thick films.

2. Development of a hybrid sol-gel processing for CFO-PZT thick films fabrication.
3. Magnetic and electrical investigation on CFO thick films.
4. Multiferroic CFO-PZT thick films and their optimization process for ME coupling application.

1.3 MAJOR CONTRIBUTION OF THE THESIS

The major contributions achieved in this research work are summarized as follows:

1. Multiferroic CFO-PZT composite thick films with thickness up to 100 μm were prepared onto alumina substrate using a screen printing method. Room temperature ferromagnetic and ferroelectric properties were studied. Through detailed characterizations on their structure and quantitative analysis on their properties, the advantages and disadvantages of screen printing method were determined and discussed.
2. A hybrid sol-gel processing was developed to deposit magnetic CFO thick films and multiferroic CFO-PZT thick films by spin coating technique. This processing included the preparation of nano-sized powder, synthesis of sol-gel precursor and xerogel, the combination of different slurries as well as the deposition tips. Thermal analysis, size distribution, X-ray diffraction (XRD), scanning electron microscope (SEM), and transmission electron microscope (TEM) were employed to study this processing and thick films structure. Ferromagnetic, ferroelectric, and leakage current behavior were also investigated.

3. Based on the preparation of CFO sol-gel solution and its nano-sized particles, CFO composite thick films were prepared on Pt/Ti/SiO_2/Si substrate by the hybrid sol-gel processing. Through annealing at different temperatures, the phase structure of CFO composite thick films was studied in terms of XRD pattern. Furthermore, the dependence of the saturation magnetization and magnetic coercivity on the annealing temperature was studied. An interesting impedance relaxation behavior was observed at low frequency, which could be modeled with a Nyquist semicircular arc in the impedance spectra. In addition, the related A.C. conductivity behavior was analyzed via the universal dynamic response law. Finally, an optimized annealing temperature which could provide a beneficial dielectric property of CFO thick film was obtained.
4. Further analysis on impedance spectroscopy and conductivity spectra from 25 to 200^{o}C for the optimized CFO thick film was carried out in detail. Two relaxations were observed in the impedance spectra corresponding to both semicircular arcs in Nyquist plots. The high frequency semicircular arc was induced by co-effect of grains and grain boundaries, whereas the low frequency semicircular arc was due to the electrode polarization effect. Electrical modulus studies demonstrated that the grain effect was decisive below 100^{o}C, while the grain boundary effect was playing a more important role above this temperature. Non-Debye relaxation was subsequently observed in dielectric spectra, and imaginary dielectric constant spectra further indicated two segments of frequency independent conductivity, which were demonstrated in real conductivity spectra. In the conductivity

spectra, on one hand, the D.C. plateau at high frequency obeyed the double power law along with two similar power parameters, indicative of the comparative contribution from grains and grain boundaries. The peak in temperature dependent power parameters suggested the crossover from grain effect to grain boundary effect. Moreover, the D.C. conductivity well obeyed the Arrhenius law and the estimated activation energy was the same as the one calculated from high frequency imaginary impedance peaks. On the other hand, the other plateau at low frequency obeyed the power law, and its power parameter was 1.12, suggesting a localized or reorientational hopping motion probably induced by Au/Ti layer. In addition, the activation energy calculated from its fitted D.C. conductivity showed the same value as the one from low frequency imaginary peaks, demonstrating the electrode polarization contribution to the low frequency Nyquist semicircular arc.

5. Crack-free CFO-PZT multiferroic composite thick films (above 5 μm) with CFO content ranging from 0.36% to 4.58% were deposited onto $Pt/Ti/SiO_2/Si$ substrate by a sol-gel processing assisted by organic additive. The additive enhanced the film thickness dramatically and avoided the cracks on film surfaces. Through studies on the microstructure and properties of multiferroic thick films, it was concluded that with proper CFO content of 1.8%, a ME coupling effect in this thick film could be predicted. Direct ME measurement demonstrated this expectation.
6. Through introducing sufficient PZT sol infiltration in CFO-PZT multiferroic composite thick films during the sol-gel deposition process,

their ferroelectric and dielectric properties were enhanced as well as the breakdown voltage strengthened. *Ps* and *Pr* could reach 42.6 μC/cm^2 and 17.22 μC/cm^2 with 4 layers of PZT sol layers. The dielectric constant was also enhanced to 869 at 100 kHz with a reduced loss of 0.017. Magnetic property kept a controlled decrease with increasing sol infiltration. All of them were attributed to the promoted film densifications.

7. Based on the optimization of CFO-PZT composite thick films by introducing sol infiltration and proper PVP, CFO magnetic content was increased to 20 wt% in PZT matrix. However, experimental results showed that when the magnetic content was controlled at 8 wt% and with proper deposition sequence, balanced ferroelectric and ferromagnetic properties could be achieved. A significant ME coupling effect in these composite thick films was hence predicted.
8. Besides the multiferroic analysis, dielectric and conductive mechanisms of multiferroic CFO-PZT composite thick films were investigated in the temperature range of 25-275^{o}C with the frequency ranging from 100 Hz to 1 MHz. Impedance spectroscopy and electrical modulus analysis indicated the contributions from grains and grain boundary effect at different frequencies and temperatures, resulting in two different grain boundary effects being observed in modulus spectra. Activation energy calculated from two methods kept in good agreement with each other. Dielectric spectra revealed a polaron relaxation below 150^{o}C and above this temperature, a D.C. conductivity region and two nearly constant loss regions were observed, which was demonstrated in A.C. conductivity

spectra. Furthermore, ion hopping and transport were also revealed by A.C. conductivity analysis. Jump relaxation mode was well used to clarify them.

1.4 Organization of the Thesis

This thesis comprises of seven chapters:

Chapter 1 gives a general introduction to the thesis.

Chapter 2 provides background knowledge on multiferroics, followed by detailed introduction on multiferroic composite bulk materials and thin films as well as a latest progress of CFO-PZT multiferroic system.

In Chapter 3, the experimental procedures used in this research work are presented, including high energy ball milling technique, sol-gel processing and spin coating technique. Furthermore, characterization tools are also introduced in this chapter, such as XRD, SEM, TEM, vibrating sample magnetometer (VSM), ferroelectric measurement analyzer, impedance analyzer and their work principles.

Chapter 4 presents the preparation of CFO-PZT multiferroic thick films by screen printing method at low sintering temperature. Property analysis was carried out and the evaluation of this process was also made.

Chapter 5 details the preparation of magnetic CFO thick films by a hybrid sol-gel process and their magnetic and electrical properties. The influence of the annealing temperature on structure, magnetic and electrical properties is studied. Dielectric relaxation and conductivity mechanism in CFO thick films are discussed.

Chapter 6 presents the deposition of CFO-PZT multiferroic thick films by the hybrid sol-gel processing as well as their characterizations results. To satisfy the requirements of ME effect, continually optimization process for promoting film quality and multiferroic properties of CFO-PZT thick films was specifically investigated. Detailed dielectric behaviors of the multiferroic thick films are presented finally to end this chapter.

Lastly, the conclusions and recommendations for the CFO-PZT multiferroic system are given in Chapter 7.

CHAPTER 2 BACKGROUND

This chapter introduces the background of two-phase multiferroics. After that, we focus on the multiferroic bulk ceramics and thin films and presented their development history. Subsequently, recent progress of CFO-PZT multiferroic systems is presented as well as an introduction of parent CFO and PZT materials.

2.1 GENERAL DESCRIPTION OF TWO-PHASE MULTIFERROICS

Due to the practical restrictions of single-phase multiferroics [16], multiferroic composites were explored for high-sensitivity A.C. magnetic field sensors and electrically tunable microwave devices such as filters, oscillators and phase shifters, in which the ferri-, ferro- or antiferro-magnetic resonance was tuned electrically instead of magnetically [11]. In addition, trends toward device miniaturization have led to increasing interest in combining electronic and magnetic properties into multifunctional materials, so that a single device component can perform more than one task [2]. Ferromagnetic ferroelectric multiferroics were particularly appealing not only because they have the properties of both parent compounds, but also because that interactions between the magnetic and electric polarizations lead to additional functionalities. For example, the ME effect (the induction of a magnetization by an electric field; or of a polarization by a magnetic field) could yield entirely new device paradigms, such as electric field controlled magnetic data storage. The mechanism for this ME interaction is owing to the stress-mediated transformation between

electrical and magnetic orders, which has been demonstrated extensively in many material systems [17, 47]. The following parts will present the development of multiferroic bulks and thin films with this mechanism specifically [11].

According to the connectivity concept from piezoelectric composites [59], the ME composites could have various connectivity schemes. But the common connectivity schemes are 0-3-type particulate composites of piezoelectric and magnetic oxide grains, 2-2-type laminated ceramic composites consisting of piezoelectric and magnetic oxide layers, and 1-3-type fiber composites with fibers of one phase embedded in the matrix of another phase, as shown in Figure 2-1. Among them, $BaTiO_3$, $Pb(Mg,Nb)O_3$, $PbTiO_3$, etc., are usually chosen as the piezoelectric ceramic phase, and ferrites usually as the magnetic phase.

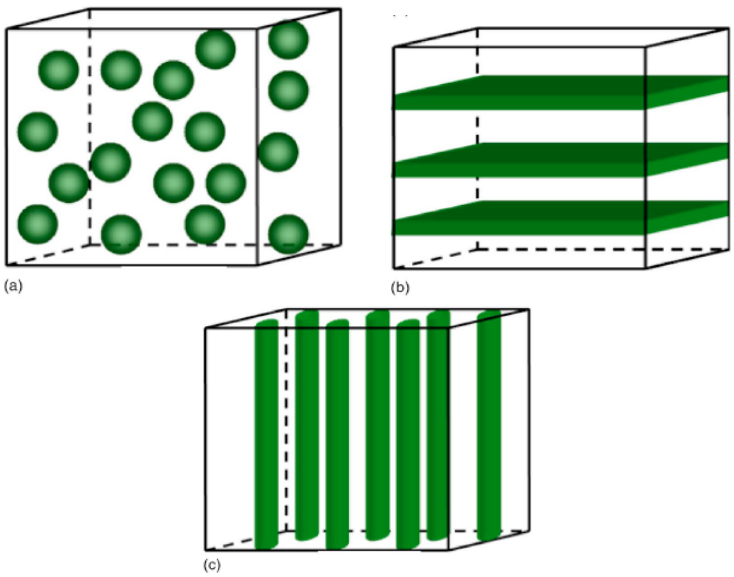

Figure 2-1 Schematic illustration of three bulk composites with the three common connectivity schemes: (a) 0-3 particulate composite, (b) 2-2 laminate composite, and (c) 1-3 fiber/rod composite [11].

Solomon proposed firstly the concept of a product property in two-phase composite materials in 1966 [60], arising from an elastic coupling between two phases of different properties. The ME effect in a composite material having one magnetostrictive and one piezoelectric phase is one such product tensor property, as described by Equation 1-1 and 1-2. In this case, the coupling is mechanical. If an input magnetic field is applied to this composite material, then

$$\frac{\partial S}{\partial H} = e_m \qquad (2\text{-}1)$$

for the magnetic phase, and

$$\frac{\partial P}{\partial S} = e \qquad (2\text{-}2)$$

for the piezoelectric phase; where S is the strain and e_m and e are, piezomagnetic and piezoelectric coefficients, respectively. As a result, this two-phase composite material can be characterized by

$$\frac{\partial P}{\partial H} = \alpha = k_c e_m e \qquad (2\text{-}3)$$

where k_c is a coupling factor $0 \le k_c \le 1$ between the two phases, and α is the ME coefficient of the composite. Thus, a new property (i.e., nonzero ME coefficient α) appears in the composite consisting of magnetic and piezoelectric phases, since neither constituent phase is magnetoelectric. This new ME product response is due to elastic coupling between the two

constituent phases. High piezomagnetic and piezoelectric coefficients and strong coupling (large k_c) favor a large ME coefficient.

Soon after the product ME property in the composite combining magnetostrictive and piezoelectric phases was proposed, scientists in Philips Laboratory experimentally found that a large ME effect could be produced in such composites [61-63]. They prepared ceramic composites of $BaTiO_3$–$CoFe_2O_4$ by unidirectional solidification of eutectic compositions in the quinary Fe–Co–Ti–Ba–O system, and obtained ME voltage coefficients as high as $\partial E/\partial H = 0.13\,\mathrm{V/(cm{\cdot}Oe)}$ at room temperature. The ME effect obtained in this way can be a hundred times larger than that in single-phase multiferroic one. But unidirectional solidification is complex and requires critical control over composition and processing. At that time, ME composites did not attract much attention, and the field of ME composite research went dormant for almost 20 years across the world. Then, in the early 1990s, Newnham's group and Russian scientists prepared particulate ceramic composites of ferrites and $BaTiO_3$ or $Pb(Zr,Ti)O_3$ (PZT) by a conventional sintering processing. The sintered ceramic composites were much easier and cost effective to fabricate in comparison to eutectic composites; and additionally provided the opportunity to combine phases with widely different crystal structures. However, these sintered ceramic composites had lower ME coefficients than the prior eutectic composites in Philips.

Although experimental studies of these ME composites in the 1990s did not represent a great step forward, the experiments did inspire significant theoretical work on ME ceramic composites. A few models, such as Green's

function approach [64, 65] and various micromechanical approaches [66-69], were developed to understand coupling between the two ferroic phases and to predict the resultant ME tensor responses in bulk ceramic composites. An upsurge in the multiferroic ME composite research appeared in the early 2000s. In the past few years, various ceramic composites with different connectivity schemes including 0-3-type particulate composites and 2-2-type laminate composites have been reported. The maximum ME coefficient in the 2-2-type laminate ceramic composites is several hundreds mV/(cm·Oe) at room temperature [70].

A milestone in the development of ME bulk composites was the appearance of the giant magnetostrictive rare-earth-iron alloy $Tb_{1-x}Dy_xFe_2$ (Terfenol-D) in 2001 [46, 71, 72]. In that year, by developing Green's function technique [72, 73], it was predicted that both particulate composites with Terfenol-D embedded in a piezoelectric polymer matrix such as poly(vinylidene fluoride-trifluorethylene) copolymer [P(VDF-TrFE)] or a piezoelectric ceramic matrix such as PZT, and laminate composites of Terfenol-D/P(VDFTrFE) or Terfenol-D/PZT, could exhibit a giant ME (GME) effect. Subsequently, the laminate Terfenol-D/PZT and Terfenol-D/PVDF composites [22] have been experimentally found to exhibit such a GME effect. In particular, since 2003, Dong and co-workers [23, 27-46] have reported various laminate composites of Terfenol-D and piezoelectric ceramics, and developed various prototype ME devices based on these bulk composites. The GME response (with a ME coefficient of >1 V/(cm·Oe)) of such Terfenol-D based bulk

composites made them particularly attractive for technological applications as ME devices.

2.1.1 MULTIFERROIC CERAMICS

2.1.1.1 0-3-TYPE CERAMIC COMPOSITES

The original work on *in situ* formation of the ME ceramic composites was done at Philips Laboratories [61-63], which were prepared by unidirectional solidification of a eutectic composition of the quinary system Fe-Co-Ti-Ba-O. Unidirectional solidification helps in the decomposition of the eutectic liquid into alternate layers of a piezoelectric perovskite phase and a piezomagnetic spinel phase. Their results showed that excess of TiO_2 (1.5 wt %) gave a high ME voltage coefficient α_E =50 mV/(cm·Oe). However, other compositions showed a lower α_E of about 1-4 mV/(cm·Oe). In a subsequent work, a high ME coefficient of 130 mV/(cm·Oe) was obtained in a eutectic composition of $BaTiO_3$-$CoFe_2O_4$ by unidirectional solidification. Unidirectional solidification requires critical control over the composition, especially in oxygen stoichiometry. Directional solidifications, such as a Bridgman technique or floating zone method using single ellipsoid furnace, are complex involving tight control over the composition, cooling rate, and temperature.

In comparison, sintering processing is much easier and cheaper for fabrication of ME composite ceramics of piezoelectric ceramic phase and ferrites. The sintered composites exhibit several advantages such as freedom in the selection of constituent phases, starting particle sizes and, processing parameters. Furthermore, sintering does not require the presence of eutectic or eutectoid transformations and also provides the opportunity to combine phases

with widely different crystal structures. By carefully controlling the sintering processing and stoichiometry, higher ME coefficients of about 10-100 mV/(cm·Oe) have been obtained recently. Figure 2-2 shows the maximum ME voltage coefficient of various compositions as a function of sintering temperature in PZT and Ni-ferrite doped bulk system [74]. A high ME voltage coefficient of 115 mV/(cm·Oe) at 1 kHz was reported for the 0-3 particulate NFO/PZT composites. This high ME coefficient was attributed to a homogeneous and well-dispersed microstructure, and large grain size of the matrix PZT phase.

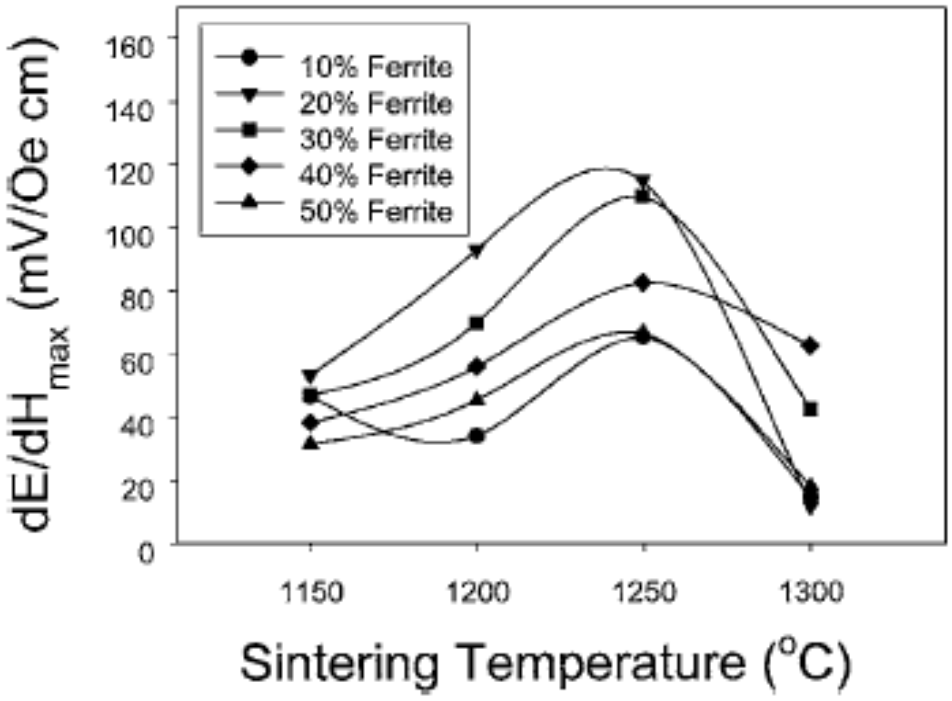

Figure 2-2 Maximum magnetoelectric voltage coefficient of the composites as a function of sintering temperature in PZT and Ni-ferrite doped bulk system [74].

The low-frequency ME coefficients of the sintered 0-3 composite ceramics vary from about 10 to 100 mV/(cm·Oe) in literature [74-77], depending on compositions, powders used and processing. Their ME coefficients can reach

up to V/(cm·Oe) orders of magnitude at resonance. So far, these measured values of the ME coefficients are lower than theoretically predicted values. In spite of the promising high ME coefficients in such simple 0-3 particulate composite ceramics, it is difficult to achieve the predicted values experimentally, which is due mainly to inter-diffusion and/or chemical reactions between the piezoelectric and ferrite phases during high-temperature sintering and to thermal expansion mismatch between two phases. The application of high sintering temperature in conventional sintering processes yields the formation of unwanted phases by solid-state reaction. For example, undesired phases such as $BaFe_{12}O_{19}$, $BaCo_6Ti_6O_{19}$, or hexagonal $BaTiO_3$ could appear in the case of $BaTiO_3/CoFe_2O_4$ composites and the inter-phase diffusion of the constitutional atoms, though difficult to verify, would lower the local eutectic point around the boundary region and thus facilitate the formation of high concentration of defects and liquid phases [77]. These would deteriorate the piezoelectricity and/or magnetostriction of constituent phases and the strain transfer between two phases. Furthermore, large thermal expansion mismatch between the piezoelectric and ferrite phases harms the densification and leads to the formation of micro-cracks.

On the other hand, the theories predict that high ME response appears in the 0-3 particulate composite ceramics with high concentration (e.g., $f > 0.5$) of ferrites (see Figure 2-4). However, the percolation (percolation: describes the behavior of connected clusters in a random graph) of high concentration of the randomly dispersed ferrite phase with low resistivity makes the electric poling of the composites become difficult and the ME properties are reduced because

of leakage problem. Therefore, good dispersion of the low-resistance ferrite particles in the piezoelectric matrix is required in order to suppress percolation. Besides, the porosity would influence the ME effect of bulk composite ceramics. For example, the results [78] show a 60%–70% decrease in the low-frequency ME effect and 96% decrease in the ME effect at electromechanical resonance, as the porosity increases from 5% to 40%.

Recently, in order to achieve sufficient bulk density while avoiding possible reactions between the constituent phases, hot pressing [79] and spark plasma sintering [80] (SPS) techniques have been employed to replace the conventional sintering. Hot-pressed and SPS samples exhibited a large improvement in the ME voltage coefficient, as compared to the conventionally sintered samples. Especially, SPS is an efficient sintering method that allows rapid consolidation (e.g., 5 min) at comparatively low temperatures, although the underlying mechanisms for an enhanced mass transport within a limited period of time still remain to be understood. This SPS method was considered to be feasible for the fabrication of the ME ceramic composites with high density (e.g., as high as 99% of theoretical density [80]) and purity. The short time and low temperature required for densification during SPS process diminish the possibility for unwanted reactions to occur.

For example, dense composite NFO-PZT ceramics with relative density of 99% have recently been prepared by SPS consolidation of mechanically mixed powder mixtures [80]. The composite ceramics via SPS exhibit dense microstructure (see Figure 2-3), and the SPS condition has an essential influence on the ME properties. In comparison to the conventional sintering,

SPS leads to an obvious improvement in the ME voltage coefficient, though the grain size in the ceramics via SPS is much smaller than that via conventional sintering.

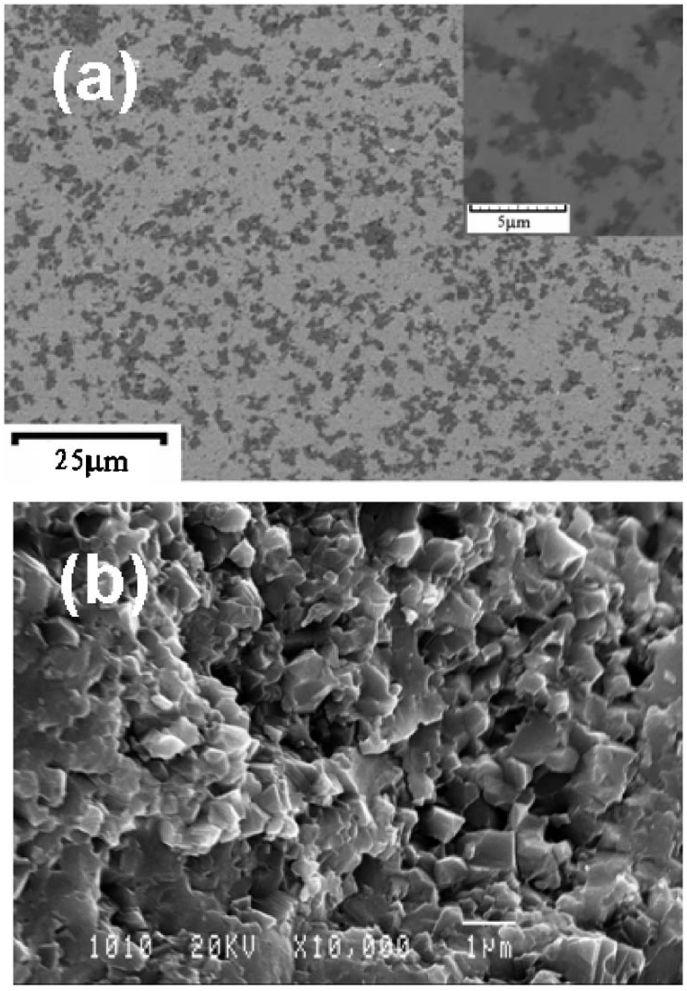

Figure 2-3 Scanning electron microscopy (SEM) images of (a) polished surface and (b) fractured surface of the NFO-PZT composite ceramics via SPS [80].

In the composite ceramics synthesized by directly mechanical mixing of the two-phase powders, the randomly mixed ferrite particles have low percolation threshold. In order to achieve good dispersion of a high concentration of ferrite particles in the composite ceramics, wet chemical processing (e.g., sol-gel method) has been employed to *in situ* synthesize the

homogeneously mixed composite powders of the piezoelectric and ferrite oxides [77, 81]. For example, Ren *et al.* [77] added cobalt ferrite nanoparticles obtained by co-precipitation into the precursor gel of BTO, allowing the *in situ* formation of ferrite-core-BTO-shell and thereby restricting the contact of the ferrite particles during sintering. The *in situ* synthesized samples showed a piezoelectric d_{33} constant approximately six times larger and a ME voltage coefficient approximately three times larger than the corresponding mechanically milled samples. The core-shell structured composites with ferrite cores and piezoelectric shell exhibit enhanced ME effect [77, 81, 82].

2.2.1.2 2-2-TYPE LAMINATE CERAMIC COMPOSITES

The leakage problem due to high concentration of the ferrite phase with low resistivity in the particulate composite ceramics can be eliminated in the laminate 2-2 composite ceramics. Laminate composite ceramics are generally fabricated by co-firing ferrite and piezoelectric ceramic layers at high temperature. ME behavior in laminate composite ceramics has been reported for various material couples (see Table 2-1) including PZT or $Pb(Mg,Nb)O_3$–$PbTiO_3$ (PMN-PT) layers laminated with Ni-ferrite (e.g., NFO), or Co-ferrite (e.g., CFO), or $(La,Ca)MnO_3$ (LCMO) ones. A laminate composite ceramic exhibits higher ME response than that of its corresponding particulate composite ceramic.

Table 2-1 Various constituent phases used for ME ceramic composites.

Piezoelectric phase	Magnetic phase
$BaTiO_3$ (BTO)	Ni ferrites (e.g., NFO)
PZT	Co ferrites (e.g., CFO)

$Pb(Mg, Nb)O_3$ (PMN)	Li ferrite (LFO)
$PbTiO_3$ (PTO)	Cu ferrite, Mn ferrite
$(Sr, Ba)Nb_2O_5$	Yttrium iron garnet (YIG)
$(Sr, Ba)Nb_2O_5$	$(La, M)MnO_3$ (M=Ca, Sr)

Srinivasan *et al.*[70] prepared such laminate composite ceramics by tape-casting technique. Both bilayers and multilayers of ferrite piezoelectrics were synthesized from thick films prepared by tape casting. The process involves: (i) preparation of submicron size powder of NFO and PZT, (ii) thick film tapes by doctor-blade techniques, and (iii) lamination and sintering of bilayers and multilayers. Ferrite powder obtained by standard ceramic techniques and commercial PZT were used. For tape casting, powders of ferrite or PZT were mixed with a solvent (ethyl alcohol) and a dispersant (Blown Menhaden Fish Oil) and ball milled for 24 h, followed by a second ball milling with a plasticizer (butyl benzyl phthalate) and a binder (polyvinyl butyral) for 24 h. The slurries thus obtained were cast into tapes on silicon coated Mylar sheets using a tape caster consisting of a pair of stationary micrometer controlled blades and a movable casting bed. It was possible to obtain 10×20 cm^2 tapes with the thickness in the range of 10-200 μm. The tapes were arranged to obtain the desired structure, laminated under high pressure (3000-5000 psi) and high temperature (400 K), and heated at 1000 K for binder evaporation. The final sintering was carried out at 1400–1500 K.

A high ME voltage coefficients of up to 0.4 V/(cm·Oe) was observed on a laminate NFO/PZT multilayer stack, where NFO was considered to exhibit nearly ideal interface coupling (k = 1) with PZT. Therefore, an important parameter in the selection of the composite constituent phases is interface

coupling between the piezoelectric and ferrite phases, which can vary significantly with the dopant concentration. But the composites with cobalt ferrite or lanthanum manganite and PZT exhibit lower ME effects that are attributable to poor interface coupling ($k \leq 0.1$). The interface coupling parameter is dependent on surface inhomogeneity and solid-state reaction between constituents during sintering as well as misfit strains.

The most common 2-2 laminate ME composite is a simple bilayer structure of a ferrite and piezoelectric ceramic layer, or sandwich structure, with a ferrite layer (or piezoelectric ceramic layer) sandwiched between two piezoelectric (or ferrite) ceramic layers, which is easily obtained by a conventional solid-state reaction method. The bilayer and sandwich composite ceramics presented similar dependence of the ME voltage coefficients on the magnetic bias field to the multilayer composite ceramics, but with ME voltage coefficient a few times smaller than that of the latter. The ME voltage coefficients of the sandwich ceramics are strongly dependent on their relative thicknesses of the two phases.

As in composite ceramics, there would still be some inter-diffusion or solid-state reactions that may occurred easily [55, 70] between the piezoelectric and ferrite layers in the high temperature sintering process (Figure 2-3), which leads to the change in the properties of the piezoelectric and magnetic phases. Different sintering behaviors of two phases lead to porosities in the ceramics (Figure 2-4). All these deteriorate the ME response of the composite ceramics.

In order to suppress the inter-diffusion and solid-state reaction and to improve the quality of the laminate composites moderately, the hot-pressing

technique [79] has also been employed. Using this technique, the ME response of PZT/NFO bulk composites was enhanced by more than one order of magnitude, while a 100% increase was achieved in PZT/NZFO multilayers.

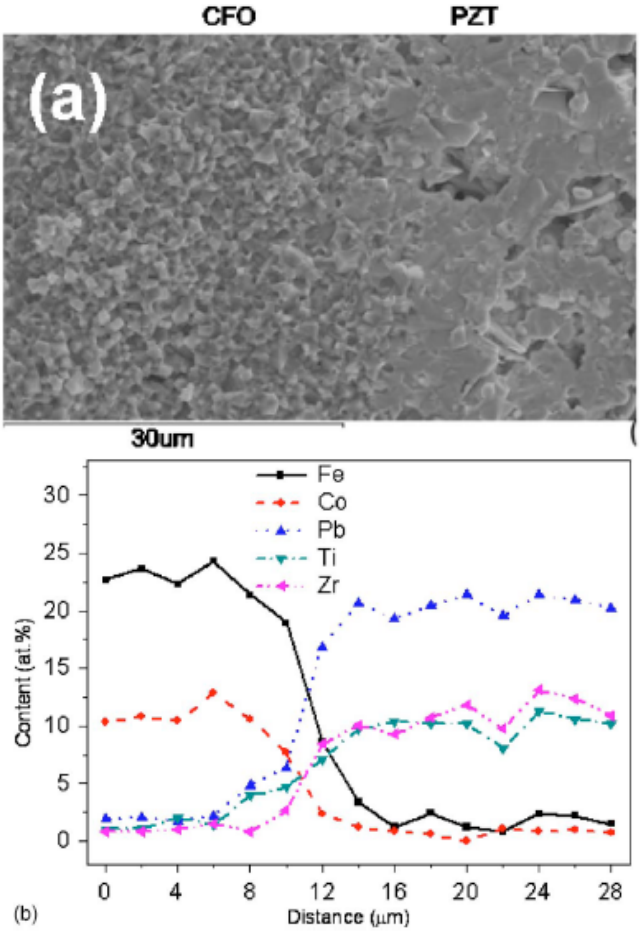

Figure 2-4 Element distribution across the boundary between CFO and PZT in the sandwich PZT/CFO/PZT ceramics [55].

Compared with the particulate composite ceramics, the laminate composite ceramics exhibits high ME coefficients due to elimination of leakage. However, high temperature co-firing processing of the piezoelectric and ferrite ceramic layers is still a big challenge due to different shrinkages, thermal expansion mismatch, and atom inter-diffusion and/or solid-state reactions between two ceramic layers during the high-temperature sintering process. Recently, a

simple bilayer ceramic composite has been prepared by simply bonding PZT and ferrite ceramic layers together with epoxy [83], not by co-firing at high temperature. In this case, the ME effect is strongly dependent on the interfacial binder.

2.1.2 MULTIFERROIC THIN FILMS

Very recently, nanostructured composite thin films with magnetic and ferroelectric oxides have been developed. In 2004, Zheng *et al.*[58] reported a pioneering experiment on nanostructured films of the $BaTiO_3/CoFe_2O_4$ system with 1-3 or 2-2 connectivity schemes. In the last five years, a series of experimental [54, 57, 84-90] and theoretical work [91-95] on such multiferroic nanostructured films of ferroelectric and magnetic oxides have been reported. Such multiferroic nanostructures have become the topic of the day in the multiferroic composites field [96], and they promise potential applications of ME composites in microelectronic devices.

In comparison to bulk multiferroic ME composites, the nanostructured thin films provide more degrees of freedom, such as lattice strain or interlayer interaction, to modify the ME behavior. They also offer a way to investigate the physical mechanism of ME effect at nanoscale. The coupling between two oxides in the multiferroic nanostructures is still due to elastic interaction, similarly to the bulk composites. However, the mechanical constraint arising from the film on substrate and the good bonding between the two phases in the nanostructured composite films could significantly affect the ME coupling interactions.

Similarly to bulk ceramic composites shown in Figure 2-3, according to the microstructure of the nanostructured composite films, there are also three kinds of nanostructured composite films, i.e., (1) 0-3-type structures with magnetic spinel nanoparticles (e.g., CFO and NFO) embedded in the ferroelectric films (e.g., PZT), (2) 1-3-type heterostructures (vertical heterostructures) consisting of magnetic spinel pillars (e.g., CFO) vertically embedded into a ferroelectric films (e.g., BTO, PTO, or BFO), and (3) 2-2-type heterostructures (horizontal nanostructures) consisting of alternating layers of a ferroelectric perovskite and magnetic oxide.

Few works were reported on the 0-3-type nanostructure [54, 85]. Wan *et al.* [85] prepared a PZT-CFO composite thin film using sol-gel spin-coating process. The phase separation of CFO and PZT phases in the films was verified by X-ray diffraction. The films exhibited both good magnetic and ferroelectric properties, shown in Figure 2-5 and the ME effect of these films was found to be strongly dependent on the magnetic bias and magnetic field frequency.

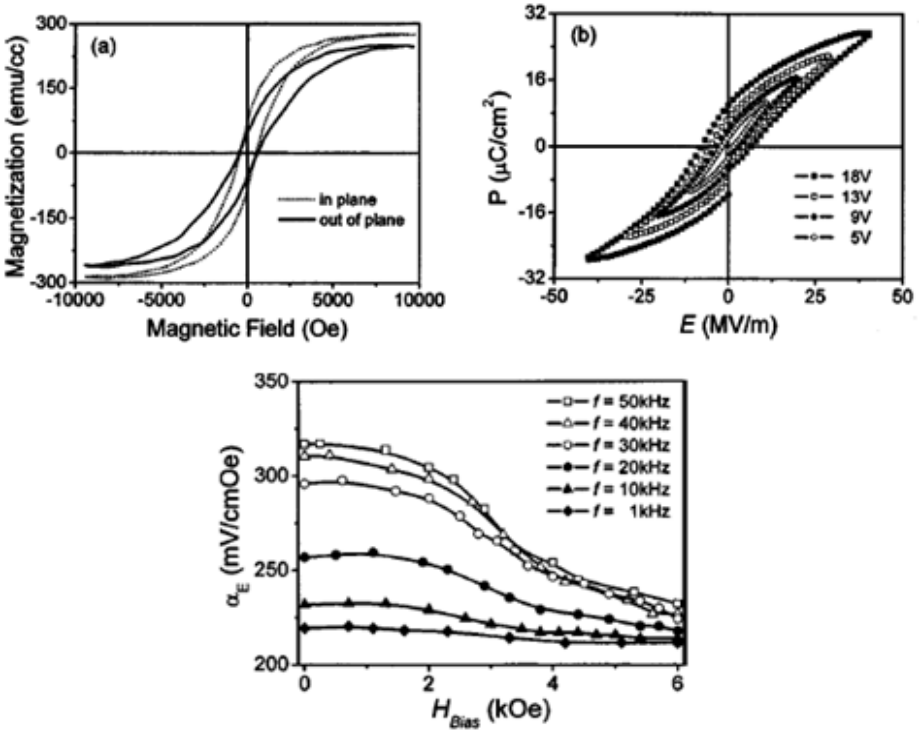

Figure 2-5 Ferromagnetic (a), ferroelectric (b) behaviors of CFO/PZT thin film with 0-3-type and its magnetoelectric coefficient (c) [85].

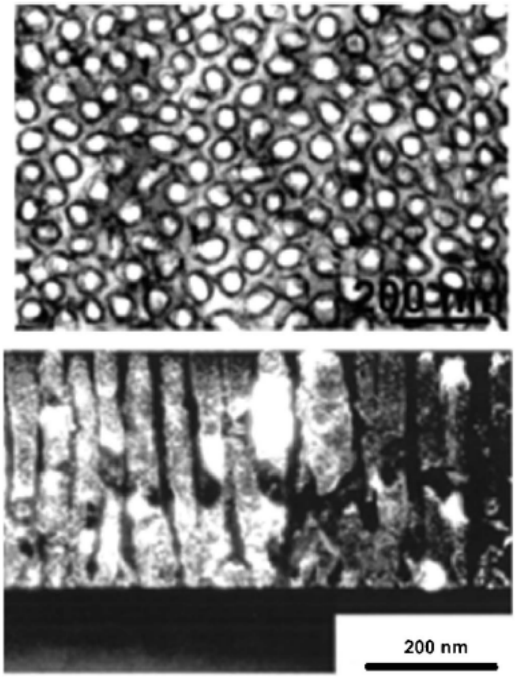

Figure 2-6 Plan view TEM image and cross-sectional dark field TEM image of $CoFe_2O_4$ nanopillars embedded in the $BaTiO_3$ matrix [84].

In comparison, more publications have focused on 1-3 and 2-2 heterostructures, seen Figure 2-6. The prototypical 1-3 vertical heterostructure consists of a magnetic spinel phase epitaxially embedded into the ferroelectric matrix. The first example was reported by Zheng *et al.* [58], where arrays of magnetic CFO nanopillars with diameters of 20-30 nm were embedded in a ferroelectric BTO matrix films.

Recent work has demonstrated substantial ME coupling in such nanostructures through switching of the magnetization on reversal of the ferroelectric polarization [97, 98], which was attributed to (1) the reduced clamping effect by the substrate in the vertical architecture, and (2) efficient strain coupling resulting from a larger interfacial surface area and intrinsically heteroepitaxial in three dimensions. Detailed studies suggest that the switching is mediated by strong mechanical coupling between the two lattices, which leads to a time dependent modulation of the magnetic anisotropy in the nanopillars. But controllable switching of the magnetization can only be achieved if an additional weak magnetic field is superimposed to lift the time-reversal symmetry.

Although the ME coupling has been observed via microscopy in such vertical nanostructures [97, 98] by switching the magnetization on reversal of the ferroelectric polarization, the ME coefficients could not be directly measured in the 1-3-type vertical heterostructures because of leakage resulting from the low resistance of the magnetic pillars penetrating through the films or the magnetic matrix. The leakage problem would erase the promising direct ME effect in the vertical nanostructures.

In comparison with the vertical nanostructures, the 2-2-type horizontal heterostructures exhibit strong ME effects due to the large in-plane constraint from substrates [95]. Moreover, the horizontal nanostructures are easier to be fabricated, and eliminate the leakage problem due to the ferroelectric layers shutting off circuit, which could lead to visible ME effect.

Different 2-2-type combinations of ferroelectric perovskites (e.g., BTO, PZT) and magnetic oxides (e.g., $CoFe_2O_4$, $NiFe_2O_4$, and $La_{1.2}Sr_{1.8}Mn_2O_7$) have been grown via pulsed laser deposition and sol-gel spin-coating method [57, 86, 88]. These layered films have shown good concurrence of ferroelectric and ferromagnetic behaviors. For example, Figure 2-7 shows a simple BTO-NFO bilayer nanocomposite film and the obvious ME response of the heterostructured film [99]. As seen from Figure 2-7, when an in-plane alternating magnetic field signal δH is applied, there is no ME output δV produced in the single-phase BTO and NFO films. In comparison, the heterostructured NFO/BTO film clearly demonstrates the ME output following the switch of the magnetic excitation signal δH. The observation of the ME coupling in the heterostructures can only be achieved as a weak A.C. magnetic field δH is superimposed to lift the time-reversal symmetry.

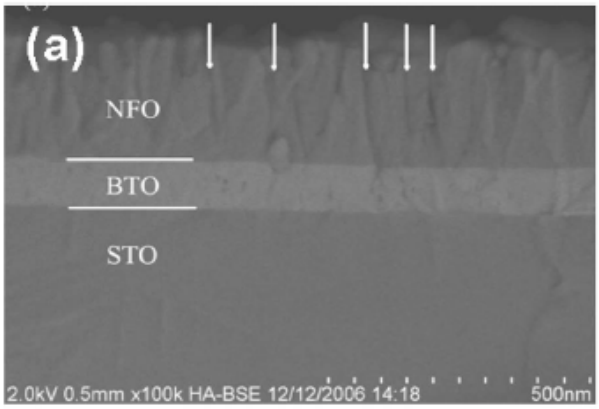

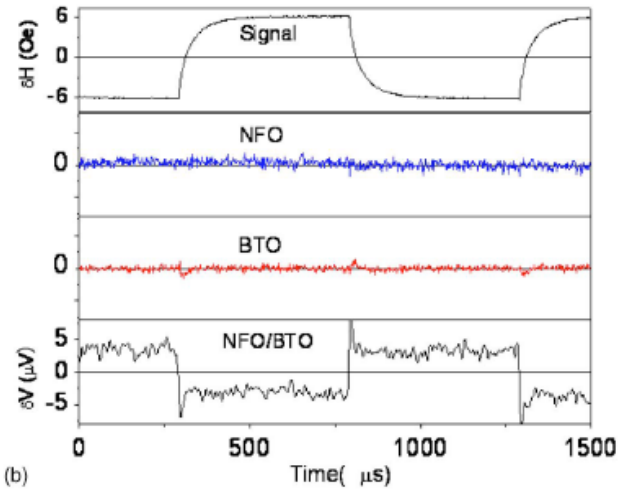

Figure 2-7 (a) A cross-sectional SEM image of the heterostructured NFO/BTO composite film grown in STO substrate; and (b) the ME response (induced ME voltage δV) of this film when the in-plane magnetic field is applied (ac magnetic field δH at 1 kHz with a bias magnetic field of 100 Oe). For comparison, the results for pure NFO and BTO films are also shown [99].

2.2 CFO-PZT MULTIFERROIC SYSTEM

The earliest investigation on CFO-PZT multiferroic materials can be tracked to ten years ago, when a method for calculation of the electromechanical characteristics was outlined for CFO-PZT composite ceramics [100]. However, the large interest in this system was mainly attributed to the development of CFO-BTO and CFO-BFO systems [58, 101, 102], which stimulated the revival of the CFO-PZT system. Compared with its counterparts in the CFO-BTO or CFO-BFO systems, the piezoelectric coefficient of PZT is stronger and a larger strain can be obtained under the same electric field. This is also why more and more techniques have been introduced to synthesize the CFO-PZT composite [54, 103-107], including pulsed laser deposition [86], composition spreads [108], and sol-gel processing [85] as well as the

conventional solid-state sintering for CFO-PZT bulk ceramics [109]. Table 2-2 presents the consistent development of CFO-PZT system in past five years.

2.2.1 FERROELECTRIC PZT PHASE

The materials exhibiting of spontaneous polarization and a demonstrated reorienting of the polarization are called ferroelectric materials. Usually, ferroelectric materials can be divided into four types according to their unit-cell structures: (1) the tungsten–bronze group, (2) the oxygen octahedral group, (3) the pyrochlore group, and (4) the bismuth layer–structure group. Of these, the second group (ABO_3 perovskite type) is by far the most important category, economically. The families of compositions listed ($BaTiO_3$, PZT, PLZT, PT (lead titanate), PMN, and $(Na,K)NbO_3$) represent the bulk of the ferroelectric ceramics manufactured in the world today.

Table 2-2 The progress of CFO-PZT system in past five years.

Reference	Thickness	Fabrication method	Comments
CFO-PZT composite thin films (2005) [85]	~400 nm	Sol-gel process	*Slim P-E and M-E*
CFO-PZT thick films (2006) [81]	~1 μm	PVP-assisted sol-gel method	*Broad P-E and slim M-E*
PZT/CFO composite ceramics (2006) [55]	Above 1 mm	Co-sintering technique	*Interface diffusion*
CFO/PZT composite thin films (2006) [54, 105]	~350 nm	Pulsed laser deposition	*Thickness dependent P-E and slim M-H*
CFO/PZT stacked heterostructures (2006) [110]	~150 nm	Soft electron-beam lithography	*Radially stacked "core-shell" heterostructure patterns*
CFO-PZT double-layer thin film (2006) [86]	~30 nm	Pulsed laser deposition	*Too thin to obtain enough measured points*
CFO-PZT thin films (2007) [107]	~100 nm	Modified sol-gel processing	*Nearly symmetric P-E and Slim M-H*
PZT/CFO composites (2007) [111]	Above 1 mm	Ethylenediaminetetraacetic acid-citrate gel process	*Impedance spectra analysis*
CFO/PZT disk-ring	Above 1	Solid-state sintering method	*Promising ME*

composite (2007) [109]	mm		*coefficient*
PZT-CFO thin films (2008) [53]	~300 nm	Sol-gel processing	*Preferred crystalline orientation*
CFO/PZT nanotubes (2008) [112]	□80 nm and □300 nm length is 100 μm	Sol-gel template	*Broad M-H and leaky P-E*
CFO-PZT nanofibers (2008) [104]		Sol-gel process and electrospinning	*Broad M-H and FE butterfly loops*
CFO-PZT thin films (2008) [113]	~200 nm	Pulsed laser deposition	*Broad P-E and the slimmest M-H, large leakage*
CFO-PZT thin films (2009) [114]	Below 500 nm	Combined route of RF magnetron sputtering and sol-gel process	*Broad M-H and in-plane stress affect the magnetization*
CFO-PZT composites (2009) [115]	Above 1 mm	Gel-combustion technique	*Slim M-H and dielectric studies*
PZT/CFO epitaxial multilayers (2010) [116]	~360 nm	Pulsed laser deposition	*Substrate dependent P-E and M-H*

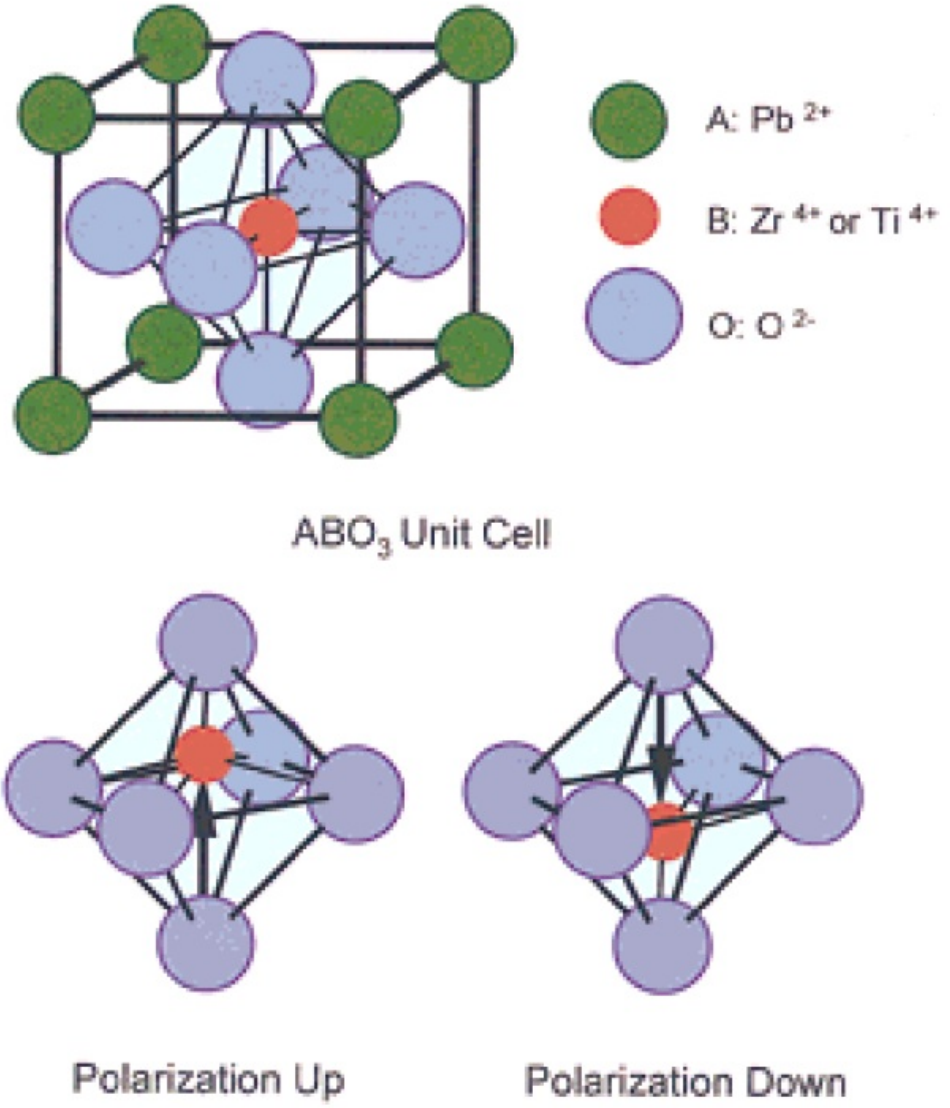

Figure 2-8 Perovskite ABO_3 unit cell for PZT, illustrating 180° polarization reversal for two of the six possible polarization states produced by displacement of the central cation in the tetragonal plane [117].

A typical ABO_3 unit-cell structure is given in Figure 2-8. For example, the PZT unit cell consists of a corner-linked network of oxygen octahedral with Zr^{4+} and Ti^{4+} ions occupying sites (B sites) within the octahedral cage and the Pb^{2+} ions situated in the interstices (A sites) created by the linked octahedral. When an electric field is applied to this unit cell, the Zr^{4+} or Ti^{4+} ion moves to a

new position along the direction of the applied field. When this ionic movement occurs, it leads to a macroscopic change in the dimensions of the unit cell and the material as a whole. The dimensional change can be as large as a few tenths of a percent elongation in the direction of the field and approximately one-half that amount in the other two orthogonal directions.

Also shown in Figure 2-8 is the reversibility of the polarization caused by the displacement of the central Zr^{4+} or Ti^{4+} ion. The displacement is illustrated here as occurring along the **c** axis in a tetragonal structure, although it should be understood that it can also occur along the orthogonal **a** or **b** axis as well. The views of "polarization up" and "polarization down" (representing 180^o polarization reversal) show two of the six possible permanent polarization positions.

When many of these unit cells, which are adjacent to each other, switch in like manner, this is referred to as domain reorientation or switching. The homogeneous areas of the material with the same polarization orientation are referred to as domains, with domain walls existing between areas of unlike polarization orientation. There exists in tetragonal materials both 90^o (strain-producing domains on switching) and 180^o domains (non-strain-producing domains), whereas the strain-producing entities in rhombohedral materials are 71^o and 109^o domains with the 180^o domains remaining as non-strain producing. Macroscopic changes occur in the dimensions of the material when strain-producing domains are switched.

It is worthy of noticing that all ferroelectrics are piezoelectric, but not all piezoelectrics are ferroelectric. PZT is not only a typical ferroelectric material,

but also a classic piezoelectric material which can produce outstanding electromechanical properties at the morphotropic phase boundary (MPB), the nearly vertical phase boundary between the tetragonal and rhombohedral regions of the phase diagram [118]. The piezoelectric strain can be caused easily in PZT under the applied electric field so as to be a good candidate for the ferroelectric part of multiferroics.

2.2.2 FERROMAGNETIC CFO PHASE

Ferromagnetic materials are those to which we commonly refer as "magnetic materials" [119]. While all materials are magnetic to some degree, many of them fall under the heading of paramagnetic or diamagnetic materials possessing only a very weak and relatively undetectable magnetic property. As such, they are not used to any extent in any practical devices but have great scientific importance. The cooperative effect called "ferromagnetism" leads to materials that have magnetic forces many orders of magnitude larger than the aforementioned materials. Ferromagnetic materials may exist as conductors, insulators or as semiconductors.

The choice of material to be used is based on the operating conditions of the device. Normally, large scale magnetic effects resulting in commercially important materials occur in atoms (an ions) of only a few metallic elements notably Fe, Co, Ni, and some of the rare earths. In alloys or oxides some materials containing these elements and some neighboring ions such as Mn, there is great enhancement of the atomic spin effect. This enhancement comes about from the cooperative interaction of large numbers of these atomic spins producing a region where all atomic spins within are aligned parallel (positive

exchange interaction). All of these materials are called ferromagnetic. CFO is a typical ferromagnetic oxide which shows a high magnetostriction constant. The mechanical motion can be produced by the magnetic excitation through magnetostriction, which is widely used in magnetostrictive transducers. It is just this intrinsic property of CFO that makes it popular in multiferroic composite.

CHAPTER 3 EXPERIMENTAL SETUP

A hybrid sol-gel processing technique is firstly introduced, in which CFO and PZT nanoparticles are dispersed into their sol-gel matrix solution for film deposition. With this technique, it was possible to coat dense, uniform and crack-free multiferroic thick films of up to tens of micrometers in thickness on a platinum coated silicon substrate.

As the hybrid processing technique is a combination of high energy ball milling and sol-gel process, both of them are presented initially in this chapter. Followed by this is the description of the equipment employed and the analysis methods used to determine the crystallization and multiferroic properties of films. The experimental approach includes three main parts:

1) Hybrid processing technology: high energy ball milling and sol-gel process;
2) Crystallization and characterization.
3) Multiferroic properties.

3.1 HYBRID PROCESS TECHNOLOGY

3.1.1 HIGH ENERGY BALL MILLING: TREAT OF PZT AND CFO POWDERS

The high energy ball milling technique was used to obtain PZT and CFO nanoparticles. In this thesis, the high energy ball milling technique was applied to reduce the powder size and promote the dispersion of nanoparticles by means of commercial organic vehicle (ESL400). The equipment employed for milling was Frisch Pulverisette 5 planetary ball-milling machine. Two closed

containers with tungsten carbide (93 wt% WC + 6 wt% Co, ρ=14.75 g/cm^3) vials and balls for each were chosen. The vial has a volume of 250 ml with an inner diameter of 75 mm and the balls have diameters of 10 mm and 20 mm.

Dry milling was employed to obtain PZT and CFO nanoparticles. Commercial PZT powder (APC850) was used with a mass ratio of 1: 20 to balls. Excess 5 wt% lead oxide was added to compensate the lead loss. The milling speed was set at 200 rpm. The milling was carried out in 15 minutes cycles: 10 minutes of milling followed by 5 minutes of pause to prevent the milling system overheating from prolonged milling. The same milling process was also applied on the synthesized CFO powder from solid-state reaction. The final PZT and CFO nanoparticles were collected after enough milling time and proper dispersion.

3.1.2 Sol-gel process: synthesis of PZT matrix

The PZT sol-gel matrix solution presented in this thesis was based on lead zirconate titanate $Pb(Zr_{0.53}Ti_{0.47})O_3$ (PZT53/47). This composition lies in the morphotropic phase boundary (MPB) region of the PZT phase diagram. It is well known that at room temperature a concurrence of tetragonal and rhombohedral structures occurs at this boundary, which leads to the maximum values of the dielectric constant and the piezoelectric coefficient of PZT material [120].

The sol-gel process generally employs metal alkoxide precursors which are often water sensitive and need to maintain close control over hydrolysis and condensation reactions. Polymeric mixed metal alkoxide species are formed to

serve as molecular building blocks for the subsequent development of a crystalline structure. There are five basic steps involved in the sol-gel process:

1) Dissolution and reaction of the cation precursors in a suitable solvent to produce a stock solution;
2) Adjusting the solution characteristics including viscosity, mole ratio, and solid content;
3) Film deposition;
4) Low temperature heat treatment for organic pyrolysis;
5) High temperature annealing for film densification and crystallization.

A chelate method, which was developed previously in our laboratory [121], was used to prepare PZT xerogel for sol-gel solution fabrication. The "chelate" method is essentially a molecularly modified alkoxide precursors (MMAP) approach to create moisture tolerant metal-organic precursors by changing the molecular structure of the precursor. The moisture tolerant precursors created in this way can be used to prepare stoichiometric and stable sols. In this thesis, acetylacetone was used as a chelating agent for titanium isopropoxide. A detailed description of this method will be given in Chapter six related to detailed experimental results.

3.1.3 SPIN COATING OF MULTIFERROIC THICK FILMS

In this thesis, most of the substrates used were (100) single crystal silicon wafer, 4 inches in diameter, coated with silicon dioxide, titanium, and the platinum bottom electrode successively. The thickness of each layer was 500 nm, 50 nm and 150 nm, respectively. Platinum is one of the most popular noble

electrode materials because it has excellent oxidation resistance. Titanium is an adhesion layer between platinum and the underlying silicon dioxide.

The substrates were cut into square pieces with the side ~ 1 inch before coating. All substrates were soaked in acetone at 80^{o}C and rinsed with isopropanol to remove oil, organic contaminants and dust from the surface. The substrates were finally rinsed with de-ionized water in the dump riser for four cycles and then dried with dry nitrogen.

Using a photo-resist spinner, a CFO-PZT multiferroic film was deposited by spin-coating at a speed of 3000 rpm for 30 seconds. Any desired thickness was reached by repeatable coating. The detailed process will be described in Chapter 6. It is worthy noticing that all preparation steps were performed in a glove box filled with nitrogen with a relative humidity controlled between 40~50%.

3.2 CRYSTALLIZATION AND CHARACTERIZATION

3.2.1 THERMAL ANALYSIS

The Differential Thermal Analysis (DTA) measures the endothermic and exothermic transitions as a function of temperature. It can determine transitions in a material's internal structure, such as glass transition temperature, melting, crystallization, curing, onset of oxidation and heat capacity. In DTA, the thermal behavior of a sample is compared with that of a standard reference material which is stable and undergoes no transition in the temperature range of interest, i.e, a thermally stable sample. In this thesis, alumina powder was used

as the standard reference, which is the most common material used in DTA analysis.

The ThermoGgravimetric Analysis (TGA) measures the amount and the rate of change in the weight of a sample as a function of temperature or time in a controlled atmosphere. Measurements are used to determine the mass change of the sample and to predict its thermal stability up to 1000°C. By comparing the DTA and TGA plots, it is possible to deduce information on the reaction kinetics and weight change of the sample as a function of temperature. Then the baking and pyrolyzing temperatures in sol-gel process can be determined.

During the sample preparation for DTA/TGA measurement, the PZT sol solution was dried in the oven at 80°C for 3 days to obtain PZT xerogel first, and then, was ground into fine powder. The DTA/TGA analysis was performed using a Perkin-Elmer 7 Series DTA/TGA Analyzer with nitrogen purged at a flow rate of 40 ml/min. The sample was heated from 35 to 1000°C at a rate of 2^{o}C/min.

3.2.2 PHASE IDENTIFICATION

The X-ray diffraction pattern is a conventional and effective technique to identify the crystalline structure of the milled powders and composite thick film samples. In this thesis, X-ray diffractometer (2400, Rigaku, CuK_{α} radiation) with a scanning speed of 2^{o}/min with a current of 40 mA and voltage of 40 kV was employed to characterize phase structure.

3.2.3 MICROSTRUCTURE CHARACTERIZATION

The microstructures of the milled powders were studied using the transmission electron microscope (TEM-JEOL2010). The TEM specimens

were prepared by dispersing the fine powder in ethanol solution using ultrasonic vibration and then sprayed onto holey carbon films, and dried in air. It was observed that the specimen was stable until irradiated by the 200 keV electron beam.

Scanning electron microscopy (SEM) is a versatile and the most commonly used technique in thin film and coating characterization to investigate the surface morphology and composition (when equipped with energy-dispersive X-ray). The surface microstructure and cross-sectional morphology of composite thick films were investigated by the field emission scanning electron microscope (FESEM-JEOL6340F) with an accelerated voltage of 5 kV. A thin layer of gold was coated for 25~35 seconds to avoid the electric charging of the samples.

3.3 MULTIFERROIC PROPERTIES

3.3.1 MAGNETIC CHARACTERIZATION

The Vibrating Sample Magnetometer (VSM) was used to measure the magnetic properties of multiferroic thick films. The principle of VSM is based upon Faraday's law according to which an *e.m.f.* is induced in a conductor by a time varying magnetic flux. In VSM, a sample magnetized by a homogeneous magnetic field is vibrating sinusoidally at a small fixed amplitude with respect to stationary pick-up coils (Figure 3-1). The resulting field change at a point *r* inside the detection coils induces voltage and is given by

$$V(t) = \sum_n \int_A \frac{\partial B(t)}{\partial t} dA \qquad (3\text{-}1)$$

where *A* is the area vector of a single turn of the coil and the summation is done over *n* turns of the coils. *B(t)* is given by the dipolar approximation, assuming small dimensions of the magnetized sample in comparison to its distance from the detection coils,

$$B(r) = \frac{\mu_0}{4\pi}[\frac{m}{r^3} - \frac{3(m \cdot r)r}{r^3}] \quad (3\text{-}2)$$

and

$$\frac{\partial B_i(t)}{\partial t} = \frac{\partial a(t)}{\partial t} \cdot \vec{\nabla}_r \{B(r)\}_i \quad (3\text{-}3)$$

$a(t)$ being the position of the dipole and $\{B(r)\}_i$, i = 1, 2, 3, the ith component of *B* at *r* due to dipole m. *V(t)* can be detected to a high resolution and accuracy by means of suitable associated electronics. For stationary pick-up coils and a uniform and stable external field, the only effect measured by the coils is that due to the motion of the sample. The voltage *V*(*t*) is thus a measure of the magnetic moment of the sample.

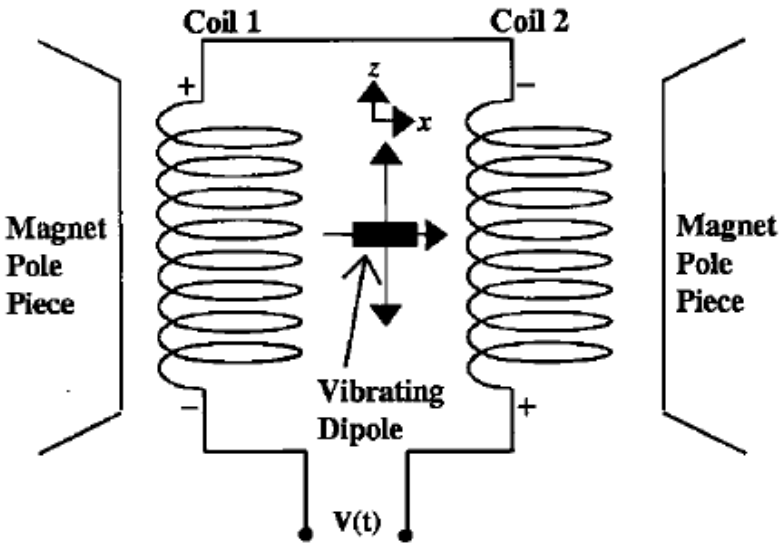

Figure 3-1 Working principle of VSM [122].

3.3.2 ELECTRICAL CHARACTERIZATION

3.3.2.1 FABRICATION OF CFO-PZT CAPACITOR FOR CHARACTERIZATION

For the purpose of characterization of the ferroelectric, dielectric properties and leakage current behavior, a metal-ferroelectric-metal (MFM) capacitor device was fabricated by thick films etching and electrode coating described as followed. A schematic of the MFM test structure was illustrated in Figure 3-2.

3.3.2.1.1 BOTTOM ELECTRODE CONTACT OPENING

Electrical contacts with the bottom platinum electrode had to be made. Multiferroic thick films were carefully etched off at a corner on the substrate to expose the bottom platinum by dipping it partially into an etchant. The etchant was made of de-ionized water, hydrochloric acid HCl and hydrofluoric acid HF in volume ratios of 50:50:0.1. An etching rate of 1 μm/min was approximately realized at room temperature. After etching, samples were rinsed in de-ionized water, dried in dry nitrogen, and then inspected under an optical microscope.

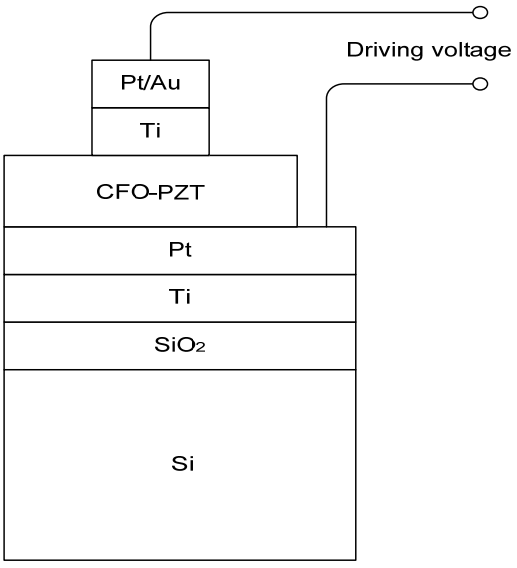

Figure 3-2 A schematic of the MFM test structure.

3.3.2.1.2 DEPOSITION OF TOP ELECTRODE

The gold top electrode was deposited on the multiferroic thick films by electron beam evaporation. Silicon shade mask or lift-off process was used to define the shape of the top electrode. 20 nm titanium and 200 nm gold films were deposited sequentially. The exact size of the top electrode was measured by an optical microscope with a scaled attachment before electrical properties measurement. The MFM capacitor was placed in a vibration-proof microprobe station and the measurement was conducted by using microprobes to contact the bottom and top electrodes.

3.3.2.2 FERROELECTRIC PROPERTY

Hysteresis loops (*P-E*) were measured using a Precision Pro Ferroelectric Analyzer (Radiant Technologies, Albuquerque, NM) with a high voltage interface. Different durations were set for the *P-E* hysteresis measurements. The hysteresis test standard was established by the CHARGE software package on the original RT66A. The stimulus takes the form of a single triangle wave. One cycle is applied to the sample to ensure that the sample starts in a known location for the measurement loop. A delay of one second allows slow parasitic effects to settle to their quiescent states. The measurement loop is then executed. Since the delay is fixed at one second, only two parameters establish the entire test: V_{Max} (the peak voltage) and the number of points to use for the test. As noted above, the number of points determines the period of the loop. The output voltage profile for the hysteresis test and three of the four parameters are shown in Figure 3-3.

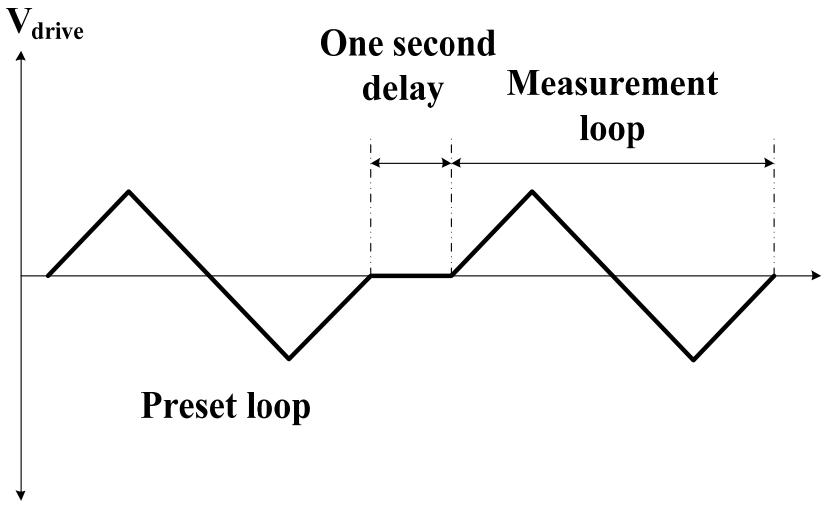

Figure 3-3 Output waveform for the hysteresis test.

In addition, in measuring *P-E* hysteresis loops several kinds of artifacts can arise. Some of these are entirely instrumental, and some arise from the effects of conductive (leaky) specimens. Hysteresis circuits do not measure polarization *P* directly. Rather, they measure the switched charge *Q*. For an ideal ferroelectric insulator

$$Q = 2P_r A \qquad (3\text{-}4)$$

where P_r is the remanent polarization and *A* is the electrode area for a parallel-plate capacitor. For a somewhat conductive sample

$$Q = 2P_r A + \sigma A E_a t \qquad (3\text{-}5)$$

where σ is the electrical conductivity per unit area, E_a is the applied field, and *t* the measuring time. Thus *Q* in a pulsed measuring system depends on the pulse width.

The four basic types of apparent hysteresis curves that are artifacts are shown in Figure 3-4.

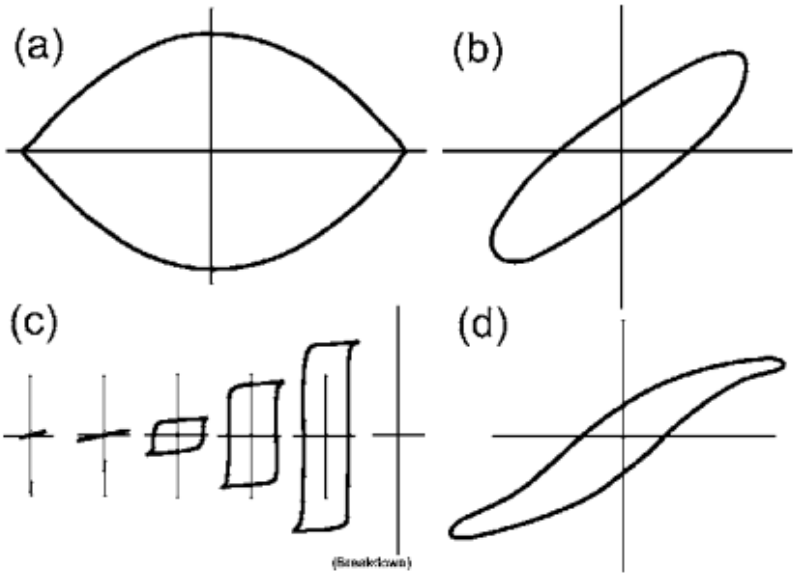

Figure 3-4 Common hysteresis artifacts: (a) dead short, (b) linear lossy dielectric, (c) saturated amplifier, and (d) nonlinear lossy dielectric [123].

Figure 3-4(a) is a dead short in a Sawyer-Tower circuit or modern variant and is discussed in the instruction documentation for Radiant testers.

Figure 3-4(b) shows a linear lossy dielectric. The points where the loops crosses $V_a = 0$ are often misinterpreted as P_r values. Actually this curve is a kind of Lissajous figure. It can be rotated out of the page to yield a straight line (linear dielectric response). Such a rotation can be done electrically and give a "compensated" curve. Here compensation means to compensate the phase shift caused by dielectric loss.

Figure 3-4(c) is more subtle. Here are two seemingly perfect square hysteresis loops obtained on the same or nominally equivalent specimens at different maximum fields. The smallest loop was run at an applied voltage of $V_a = 10$ V, and yields $P_r = 30$ $\mu C/cm^2$ and the larger at $V_a = 50$ V

and $P_r = 100\ \mu C/cm^2$. Note that both curves are fully saturated. This is impossible. If the dipoles of the ferroelectric are saturated at $P_r = 30\ \mu C/cm^2$ then there are no additional dipoles to produce $P_r = 100\,\mu C/cm^2$ in the larger loop at high voltage. What actually occurs in the illustration is the saturation of the amplifier in the measuring system, not saturation of the polarization in the ferroelectric [118].

Finally, Figure 3-4(d) is a nonlinear lossy dielectric. If it is phase compensated, it still resembles real hysteresis. One can verify whether it is real or an artifact only by varying the measuring frequency. Artifacts due to dielectric loss are apt to be highly frequency dependent [124].

All of the cases listed above should not be treated as normal ferroelectric behavior.

3.3.2.3 DIELECTRIC PROPERTY

A small applied voltage will separate the positive and negative charges in a dielectric, collecting either of charge in one plane will calculate the capacitance of the dielectric material using equation 3-6:

$$C = \frac{Q}{V} \qquad (3\text{-}6)$$

from which the dielectric constant is hence deduced,

$$\varepsilon_r = \frac{C \cdot d}{\varepsilon_0 \cdot A} \qquad (3\text{-}7)$$

where ε_r is the relative dielectric constant, ε_0 is vacuum dielectric constant, d and A are thickness and area of the detected films. In this thesis, low field

measurement of the dielectric constant and dielectric loss were carried out using an Agilent 4294A precision impedance analyzer, the measured frequency ranges from 100 Hz to 1 MHz. The AC oscillation level was set at 100 mV. The parallel circuit mode was employed during measurement.

3.3.2.4 LEAKAGE MEASUREMENT

A Precision Probe (Radiant Technologies, USA) was used to detect the leakage current of multiferroic thick films. The specific mode is Switched Linear, which can be seen in Figure 3-5. In this profile voltage increases (decreases in the case of negative V_{Max}) up to the V_{Max} value. The voltage stepping is preceded by a preset pulse in the direction of $-V_{Max}$ to ensure that the linear stepping switches the polarization of the sample. The voltage step has a uniform increase, from step-to-step of V_{Max}/((Points/2)-1). Once V_{Max} is reached, a second preset pulse in the direction of V_{Max} is performed and a linear stepped decrease (increase for $-V_{Max}$) in voltage is made. The figure details the complete voltage profile. An even number of measurement points is to be specified. If an odd number of points is specified, the software automatically resets the number of points to the specified number less one. Each of the preset pulses is followed by a one second delay before the profile leg begins. This allows any current that results from remanent or non-remanent polarization switching in the sample to settle and reach a steady-state value. Same system with that for ferroelectric measurement has been adopted and unswitched linear voltage was applied with the soak time and measure time of 500 ms and 1000 ms, respectively.

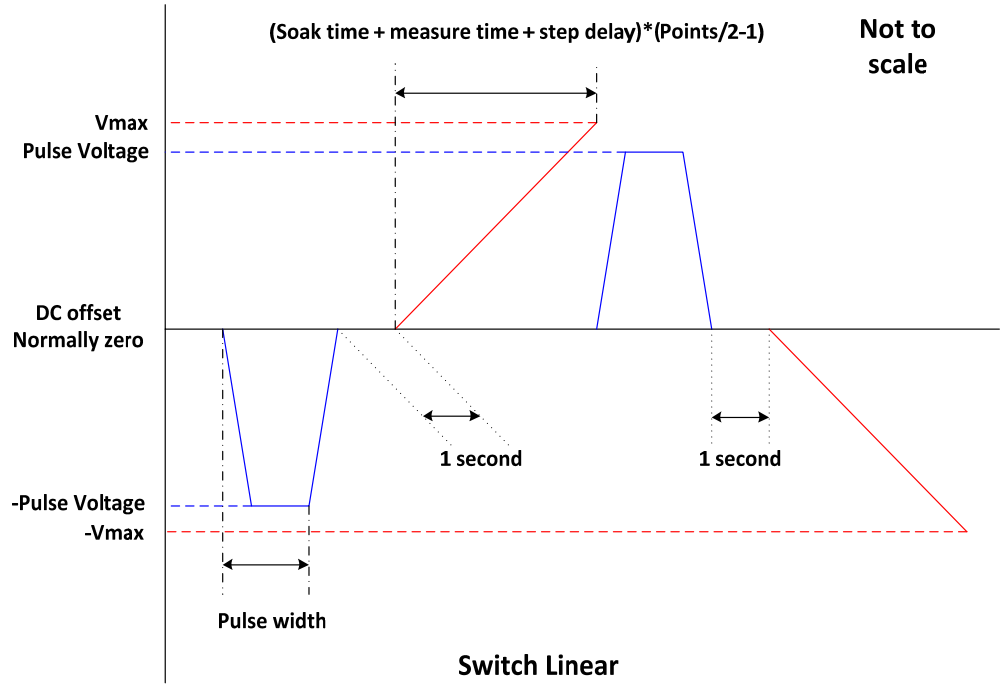

Figure 3-5 The I-V measurement process.

3.3.2.5 IMPEDANCE SPECTROSCOPY AND CONDUCTIVITY SPECTRA

Impedance spectroscopy of the thick films was primarily measured by an Agilent 4294A precision impedance analyzer over 100 Hz-1 MHz and 25-300 ^{o}C at the ac oscillation level of 100 mV. Furthermore, broader frequency spectra (0.1 Hz to 1 MHz) were obtained by employing a Solartron SI1260 (Solartron Group, Shildon, Durham County, U.K.) impedance/gain-phase analyzer. In terms of the conversion relationship between impedance and conductivity, which would be discussed in chapter 5 in details, conductivity spectra were hence presented for studying the ion motion in multiferroic thick films.

CHAPTER 4 SCREEN PRINTED CFO-PZT THICK FILMS

The screen printing method, being a most conventional and typical thick film technology, has a long history, but has not progressed smoothly. An extensive review of the early history and applications of this technology will be found in reference [125].

In its simplest terms, the technology is based on the formation of patterns through the use of woven cloth "screens" and viscous pastes. It is essentially a stencil process in which the printing medium or ink is forced through the open areas of a mesh-reinforced stencil onto the substrate of the workplace or substrate. The mesh fabric of the screen performs the dual function of holding together the various parts of the screen and also, by virtue of its thickness, metering the thickness of the ink deposit.

The ink or pastes used for thick film circuit printing consist of a suspension in an organic vehicle of finely divided metals, metal oxides, or mixture of these with a glass frit or binder. Having been deposited in the required pattern these inks, which may be formulated so as to perform the functions of conductors, resistors or insulators, is dried and fired to promote adhesion to the surface of the ceramic substrate and to develop the appropriate electrical properties.

In this chapter, $CoFe_2O_4$-$Pb(Zr_{0.53}Ti_{0.47})O_3$ (abbreviated as CFO-PZT) multiferroic composite thick films were fabricated on alumina substrates with

gold bottom electrodes by the screen printing method at a low-sintering temperature. The processing included the modification and dispersion of ferromagnetic CFO powder and ferroelectric PZT powder, the preparation of uniform pastes, and the selection of proper annealing temperatures for composite thick films. After annealing at 900^{o}C for 1 hour in air, the qualities of multiferroic thick films as well as pure CFO and PZT thick films were confirmed by tape tests. Phase structure, microstructure, magnetic, and ferroelectric properties of CFO-PZT thick films were analyzed. The feasibility of multiferroic behavior was revealed by the simultaneous observation of ferromagnetic and ferroelectric behaviors in the thick films.

4.1 SCREEN PRINTING METHOD

Modified CFO and PZT nanoparticles were used to prepare the paste. The detailed preparation procedure of modified CFO and PZT particles is described in Chapter 6. In this chapter, the modified CFO and PZT nanoparticles were mixed in a mass ratio of 1:10, and then mixed with a commercial organic vehicle (ESL400) to get the pastes via roll milling in an agate bowl for 3 hours without any other additives. The specific mixing ratio of nanoparticles and organic vehicle was listed in Table 4-1. To obtain the uniform paste, CFO-PZT paste needed less organic vehicle compared with that of pure CFO and PZT pastes.

Table 4-1 Percentage of ESL400 in different pastes and film thickness per layer.

Paste\	ESL400 (wt%)	Thickness per layer (μm)
CFO-PZT	18	25
CFO	50	10
PZT	28	19

Square plates of polycrystalline alumina with thicknesses of 0.5 mm were used as the substrate for depositing the thick films. Gold paste was firstly screen printed on the substrate and then annealed at 950^{o}C for 1 hour in a belt furnace. The thickness of the gold layer was measured as 5 μm by a surface profiler. Subsequently, three kinds of pastes (CFO-PZT, CFO, and PZT) were printed on the Au/Al_2O_3 substrates, respectively. After each printing, the thick film was kept at room temperature for 15 minutes for spreading. Then the films were moved onto a hotplate at 140^{o}C for another 15 minutes to make the films solidified before printing the next layer. After finishing the printing procedure, the films were annealed at 450^{o}C for 1 hour to evaporate the organic vehicle, and then held at 900^{o}C for 1 hour before it dropped to room temperature naturally. The heating rate was 3^{o}C/min. During this process, a tube furnace with the atmosphere air was employed.

The average thickness of each layer of the three composite thick films was measured, which can be seen in Table 4-1. CFO-PZT showed the largest thickness of 25 μm per layer and PZT was secondary, while CFO thick film was the thinnest. The difference in their thickness was closely related to the organic vehicle used. The more organic vehicle was used, the less particles were in the paste. Therefore, when the organic vehicle was evaporated at high temperature, it reduced the film thickness. The printing layers for CFO-PZT, CFO, and PZT thick films in this chapter were 4, 4, and 2 layers.

4.2 RESULTS AND DISCUSSION

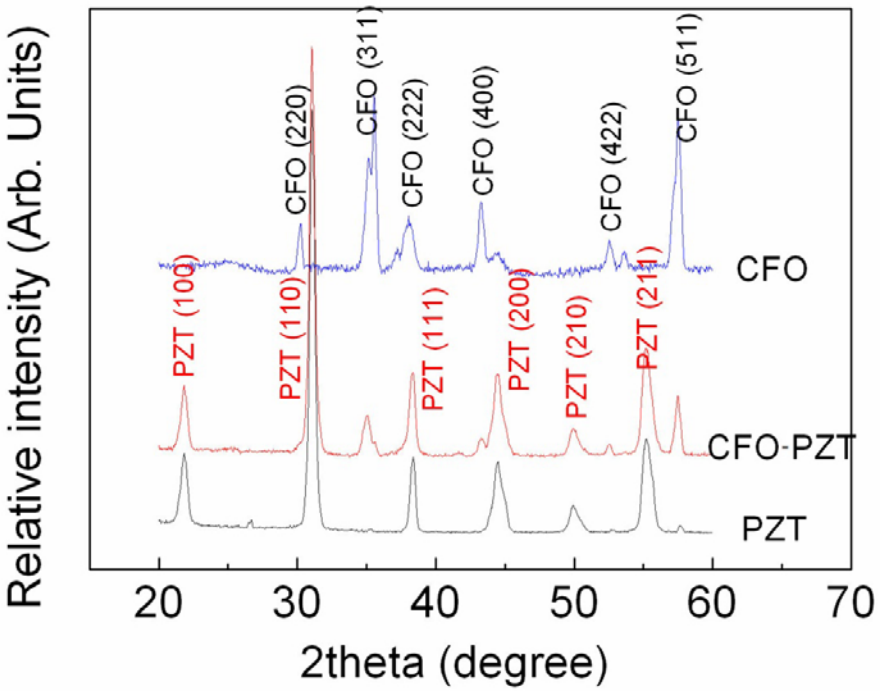

Figure 4-1 X-ray diffraction patterns of all the thick films.

Figure 4-1 shows the XRD patterns of the CFO-PZT multiferroic thick film as well as the pure CFO and PZT thick films. XRD is an efficient way to describe the phase structure of the material and distinguish different materials. The CFO spinel phase (the character peaks are described in the Figure) and PZT perovskite phase (the character peaks are described in the Figure) were observed separately in the CFO and PZT thick film. Both phases were detected in the CFO-PZT thick film, suggesting a combination of ferromagnetic and ferroelectric materials.

Surface morphologies and cross-sectional micrographs of three thick films are shown in Figure 4-2. It can be seen that CFO and PZT thick films showed homogeneous microstructures, while a heterogeneous microstructure was observed in the morphology of CFO-PZT composite thick film. Furthermore, the thicknesses of three thick films were estimated as 100 μm for CFO-PZT, 37

μm for CFO, and 35 μm for PZT thick films due to their individual dosages of organic vehicle, which were matched with the measured results by the surface profiler.

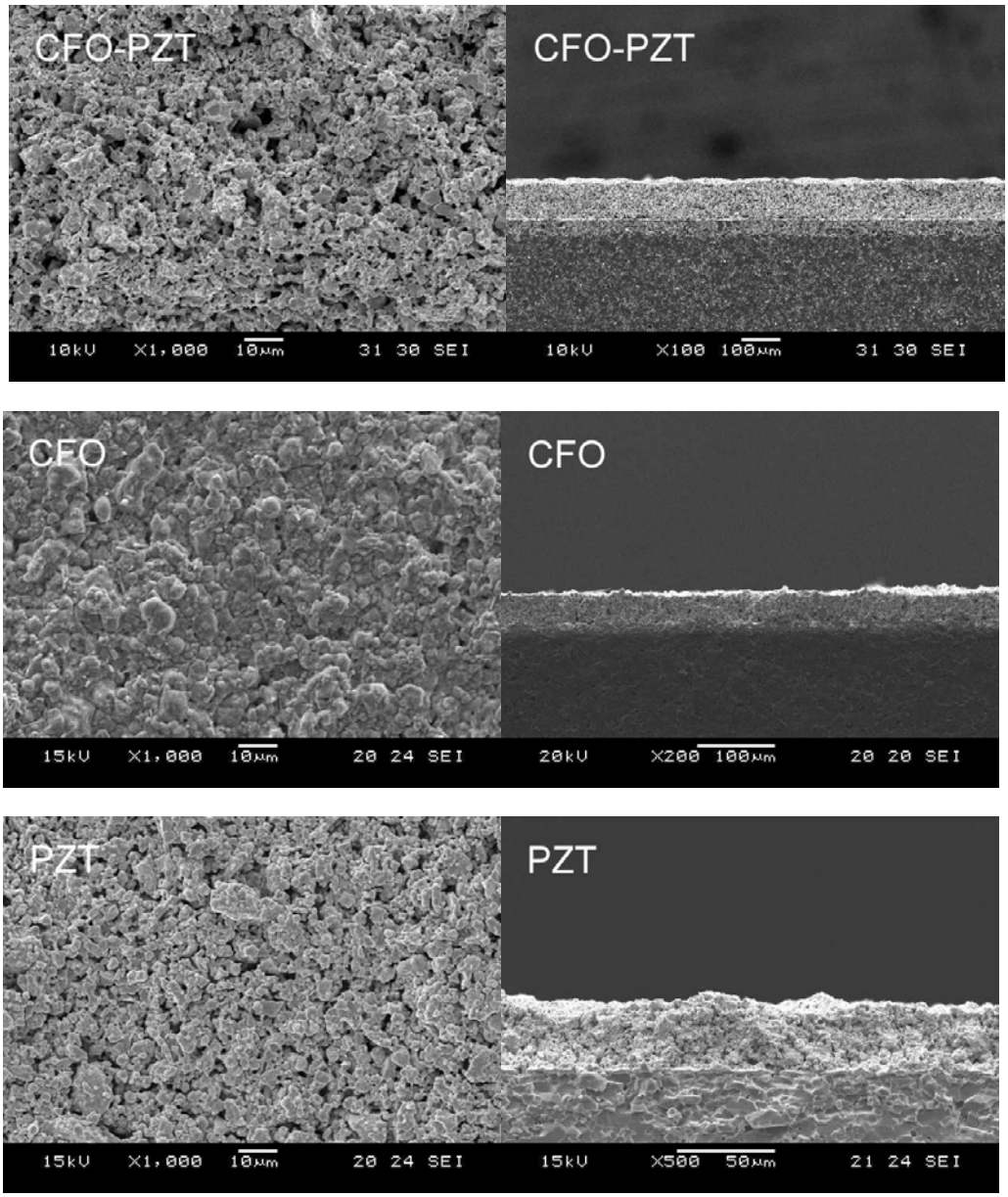

Figure 4-2 Cross-sectional micrographs and surface morphologies of three kinds of thick films.

Figure 4-3 shows the room temperature magnetic hysteresis loops of CFO-PZT and pure CFO thick films. Clearly, the saturated magnetization (*Ms*) and

the remanent magnetization (*Mr*) of CFO-PZT thick films are reduced to 14.3 emu/cm^3 and 6.7 emu/cm^3 compared with the *Ms* of 199 emu/cm^3 and *Mr* of 45 emu/cm^3 for CFO thick films.

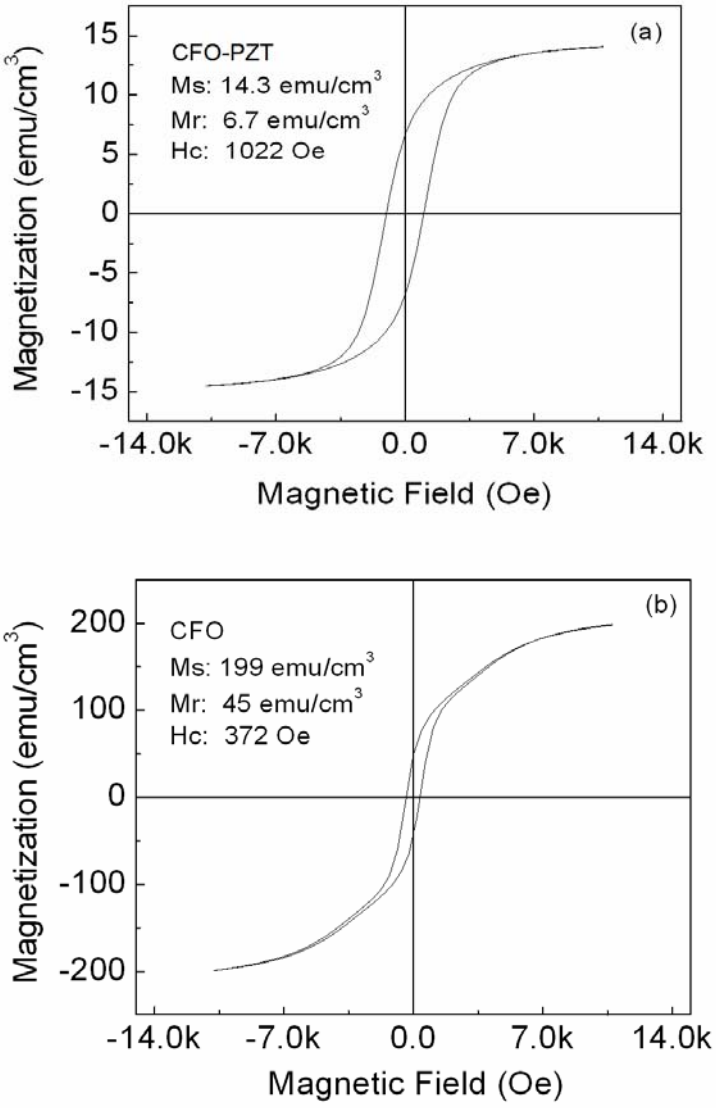

Figure 4-3 Room temperature magnetic hysteresis loops of CFO-PZT (a) and CFO (b) thick films along in-plane direction.

However, the CFO-PZT thick film showed a coercive magnetic field (*Hc*) of 1022 Oe, larger than 372 Oe of the CFO thick film. This was attributed to the

diluted effect of the PZT ferroelectric phase, which decreased the magnetization and blocked the magnetic domain wall motion and domain rotation of CFO-PZT thick film. Compared with the CFO-PZT composite thick films synthesized by sol-gel processing [126], we can see that the *Ms, Mr*, and *Hc* values of the present thick film were slightly larger than *Ms* of 13.4 emu/cm^3, *Mr* of 4.3 emu/cm^3, and *Hc* of 831.4 Oe for the sol-gel synthesized one. This is due to the larger CFO mass ratio of 10 wt% in the present case than that of 4 wt% estimated for the sol-gel case [126]. In addition, it was reported that the CFO thin films deposited on quartz substrates by spin coating [127] had a *Ms* value of 300 emu/cm^3, which is larger than the *Ms* value of 199 emu/cm^3 in the present CFO thick film, but its magnetic coercivity of 2820 Oe was also far larger than that of our film. It is also reasonable, because the porosities in the present thick film cause the decrease of *Ms* value of CFO thick film, while the reduced *Hc* value is attributed to the multi-domain configuration of the CFO particles [128].

Ferroelectric hysteresis loops of three kinds of thick films are shown in Figure 4-4 with the maximum applied voltage of 500 V. Normal ferroelectric behavior was observed in PZT thick film but only a narrow loop was found in CFO-PZT thick film, which was due to the effect of CFO which reduced the PZT's influence on ferroelectric behavior of our film [129]. The wide ferroelectric hysteresis loop of the overall CFO thick film shown in Figure 4-4(c) was generally believed to be induced by the large leakage current due to the low resistivity of CFO ferrite [128]. The remanent polarization (*Pr*) of the PZT thick film was measured as 12.5 μC/cm^2, which is smaller than the value

reported in literature after sintering at a higher temperature. It can be seen in this figure that the *Pr* value of the CFO-PZT thick film was only 1.7 μC/cm^2, far smaller than that of the PZT thick film.

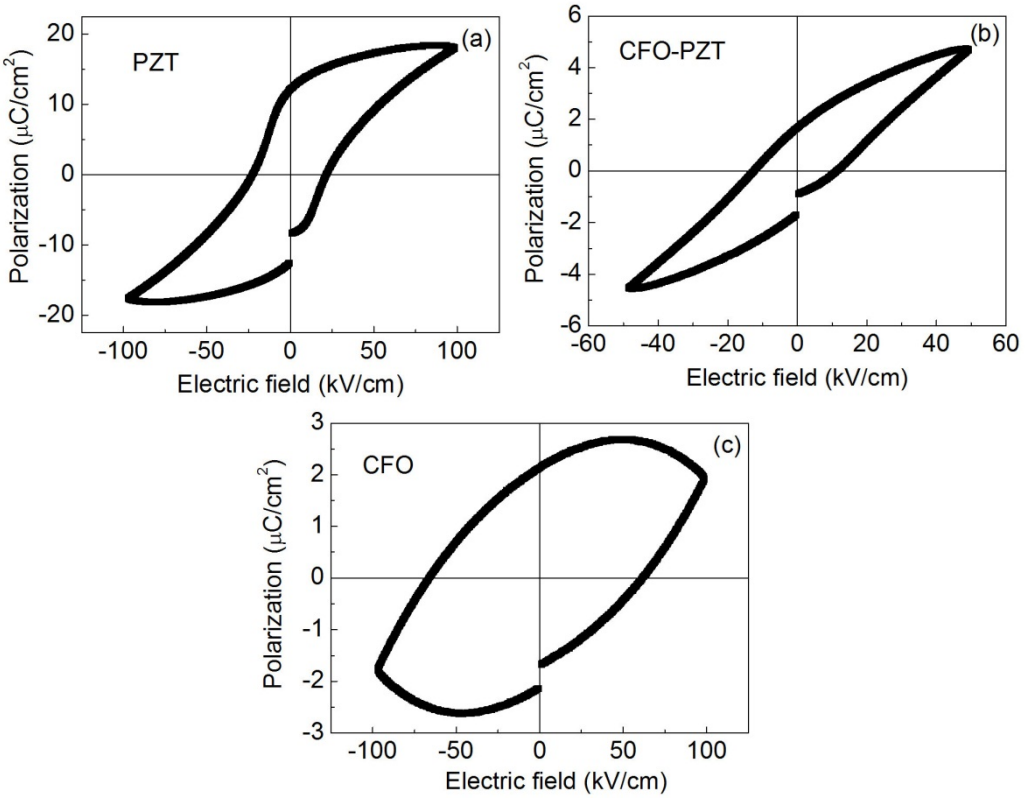

Figure 4-4 Room temperature ferroelectric hysteresis loops of three kinds of thick films at 100 Hz.

It is known that the dipole moments causing remanent polarization in the PZT ferroelectric thick film results from ion displacement, which produces a local electric field in the crystal that increases faster than the elastic-restoring forces. The introduction of the CFO phase acts against this local electric field due to the electron exchange $Fe^{2+} \leftrightarrow Fe^{3+} + e$, which exists commonly in ferrites [130]. A local electron displacement reverse to the local electric field induced by ion displacement is hence formed in multiferroics by this electron

exchange, finally reducing the dipole moments and weakening the remanent polarization. Another reason for the small *Pr* value in the CFO-PZT thick films was attributed to their large porosity. Sol infiltration or proper doping are believed to be good ways to fill in these pores and improve the ferroelectric properties of thick films [131].

From the results observed above, we can see that ferromagnetic and ferroelectric properties existed in CFO-PZT thick film simultaneously at room temperature. Compared with the sol-gel synthesized CFO-PZT thin films [107], the saturation magnetization of our CFO-PZT thick film (14.3 emu/cm^3) was far smaller than the reported 118 emu/cm^3. The main reason for this was the large CFO ratio in the reported CFO-PZT thin film with the volume ratio of 1:2, far above the mass ratio of 1:10 in our CFO-PZT thick film, which indeed indicates that the saturation magnetization is strongly dependent on the CFO fraction [129]. It had also been reported in other works on CFO-PZT thin films made by pulsed laser deposition [54] that the saturation magnetization was measured as 26 emu/cm^3 based on an approximately 23% of CFO volume fraction. Furthermore, a magnetic coercivity of 960 Oe was observed in these films, which is close to the value of 1022 Oe in our work, indicating that the coercivity is less dependent on the magnetic phase content.

On the other hand, the present ferroelectric polarization is smaller than the widely reported values of CFO-PZT films realized using spin coating and pulsed laser deposition [54, 107, 129], because our film obtained using screen printing is too thick to avoid the air porosity introduced during the printing processing. Furthermore, this porosity increased with the continually increase

of film thickness and finally degraded the polarization dramatically. This is a common effect generated by screen printing. Although optimizations of this method, such as sol infiltration [131] and additional glass powder [132], can reduce these porosities and improve the ferroelectric property, the film thickness from this method was beyond our expectation. An alternative processing route was hence needed to satisfy the required film thicknesses for multifunctional MEMS applications.

4.3 SUMMARY

Multiferroic CFO-PZT composite films with an average grain size of submicron-meter were prepared on alumina substrates using a screen printing method and sintered at a relatively low temperature of 900^{o}C. Thicknesses up to hundreds of micrometers were achieved. XRD analyses indicated the concurrence of the CFO and PZT phases in the film. The microstructures of the pure CFO and PZT films were also studied by SEM. Ferromagnetic and ferroelectric properties were observed at room temperature in CFO-PZT thick film simultaneously, but the ferromagnetic and ferroelectric parameters were lower than their individual parent. Compared with CFO-PZT thin films, quantitative analyses indicated that the multiferroic properties of our composite thick films were degraded, which was mainly due to the porosity of our composite thick film. This showed the shortcoming of this deposition technique, and a hybrid sol-gel process was hence introduced to replace it, as will be detailed in the follow in the following chapter.

CHAPTER 5 DEPOSITION OF CFO THICK FILMS AND PROPERTIES CHARACTERIZATIONS

Chapter 4 showed the shortcoming of the screen printing method in the preparation of CFO-PZT thick films. In the present chapter, we describe another process that would avoid this drawback. Before proceeding to the CFO-PZT thick films, we need to learn the properties of CFO and PZT thick films first. Since PZT thick films have been widely discussed earlier [56, 133], our focus will be on the preparation of CFO composite thick films.

A hybrid sol-gel process was adopted to fabricate magnetic $CoFe_2O_4$ composite thick films onto $Pt/Ti/SiO_2/Si$ substrates by spin coating. The process included the chemical synthesis of $CoFe_2O_4$ sol-gel solution, the modification of the $CoFe_2O_4$ particles via high energy ball milling and the synthesis of a uniform $CoFe_2O_4$ hybrid slurry. Thermogravimetric Analysis/Differential Thermal Analysis (TGA/DTA) studies indicated that the baking and pyrolysis temperatures were 140^{o}C and 300^{o}C, respectively. After annealing at 550-700^{o}C in the air, pure $CoFe_2O_4$ spinel phase was observed above 600^{o}C in the X-ray diffraction pattern. The resultant thick films were measured to be 10 μm thick by a surface profiler and cross-sectional photos taken with the scanning electronic microscope. The increase in annealing temperature increased the grain size of our $CoFe_2O_4$ composite thick films, which increased their magnetic coercivity and saturation magnetization. Furthermore, electric measurements indicated the dependence of the impedance relaxation on the annealing temperature in the frequency range of 10 Hz-10 kHz. Above 10 kHz,

impedance curves merged together; while below 10 Hz, diffusion was observed. This was not observed in $CoFe_2O_4$ bulks or thin films. Further investigations of A.C. conductivity spectra demonstrated the nature of ion motion in the composite thick films. The annealing temperature was optimized as 650^oC for the fabrication of $CoFe_2O_4$ composite thick films with promising electrical properties.

5.1 PREPARATION OF COBALT FERRITES THICK FILMS AND THEIR MAGNETIC AND ELECTRICAL PROPERTIES

5.1.1 INTRODUCTION

In recent years, spinel ferrites have shown interesting electrical conductivity and dielectric properties in nanocrystalline form compared with those having micrometer-sized grains [134-136]. Typical examples of Ni-Zn ferrites and Co-ferrites have been extensively investigated. It was found that dielectric constant of nanostructured Ni-Zn ferrite is smaller than that of bulk ceramics [137], while it is the other way around for the Co-ferrites [138]. Fortunately, the dielectric loss is reduced for both the previously mentioned nanostructured ferrites compared to their bulk counterparts. Furthermore, a non-Debye type of dielectric relaxation was observed in these ferrites, which was described by electrical modulus [137-139]. However, not much work has been done on the cobalt ferrite thick film which is one of the potential candidates for magnetic and magneto-optical recording media [140, 141]. Much attention has been paid to the synthesis of nanostructured cobalt ferrite particles as well as bulk ceramics or thin films [126, 142-146] and the characterization of their magnetic properties. Their dielectric properties, which can provide important

information on the behavior of localized electric charges, and hence facilitates a better understanding of the mechanism of dielectric polarization, have drawn little interests except a few reports on the nanostructured $CoFe_2O_4$ powder [138, 147]. Recently, more attention has been paid to the electric properties of the double-phase multiferroic composites, such as CFO-PZT and CFO-BTO [148, 149] or their doping systems [150]. In contrast, similar data on pure $CoFe_2O_4$, especially its thick film structures which is critical for potential MEMS designs, have not been found in literature.

In order to explore the fabrication process of cobalt ferrite thick films and their electrical properties for potential MEMS applications, the present work has adopted a fabrication method similar to that used typically for PZT ferroelectric thick films [151]. Cobalt ferrite composite films with 10 μm were prepared via a hybrid sol-gel processing. The effects of annealing temperature on the phase structures, microstructures, magnetic and electrical properties were characterized. Furthermore, A.C. conductivity spectra analysis was employed to investigate the nature of ion motion in $CoFe_2O_4$ composite thick films and the possible physical mechanism underlying it was then discussed.

5.1.2 Synthesis and deposition

$CoFe_2O_4$ (abbreviated as CFO) sol-gel solution was prepared by mixing cobalt acetate, ferric nitrate, and polyvinylpyrrolidone together at 60^{o}C according to the molar ratio of 1: 2: 2 until a clear solution was obtained. Then 40 ml of 2-methoxyethanol was added to get 0.125 M of CFO sol-gel solution. The pH value of resultant dark-red CFO sol-gel solution was 4.2. In addition, modified CFO particles were prepared by a high energy ball milling method as

reported previously [151], which resulted in an average particle size of 233 nm. Next, the modified CFO particles were dispersed in the CFO solution with a mass ratio of 2:3. The process is similar to the fabrication of hybrid PZT slurry [148], to get the uniform CFO slurry via an agate ball milling for 15 hours. The collected CFO slurry showed a black color and was immediately spin coated onto the Pt/Ti/SiO_2/Si substrate with CFO sol-gel solution to obtain the dense CFO film. After coating each layer, the film was baked at 140^{o}C for 3 minutes to dry the solvent and then held at 300^{o}C for another 3 minutes to burn up the organic components. The obtained thick films were annealed in air at 550^{o}C, 600^{o}C, 650^{o}C, to 700^{o}C for 1 hour, respectively, and their thicknesses were measured via a surface profiler to be around 10 μm.

5.1.3 Structural characterization

TGA/DTA analysis of the CFO slurry dried at 110^{o}C for 24 hours is shown in Figure 5-1. TGA yielded a weight loss of 21 wt% before 300^{o}C, and then remained approximately stable until 800^{o}C. In the DTA curve, two exothermic peaks were observed: one at 126^{o}C due to the organic solvent evaporation and the other at 300^{o}C representing the decomposition and combustion of the bound organic species in the CFO slurry. Since the CFO powder had been presintered at a high temperature of 1200^{o}C before high energy ball milling, it had almost no effect on TGA/DTA analysis. The observations of weight loss in TGA and exothermic peak in DTG were presumably attributed to the sol-gel part of the composite film. That was why 140^{o}C and 300^{o}C were selected after each coating processing.

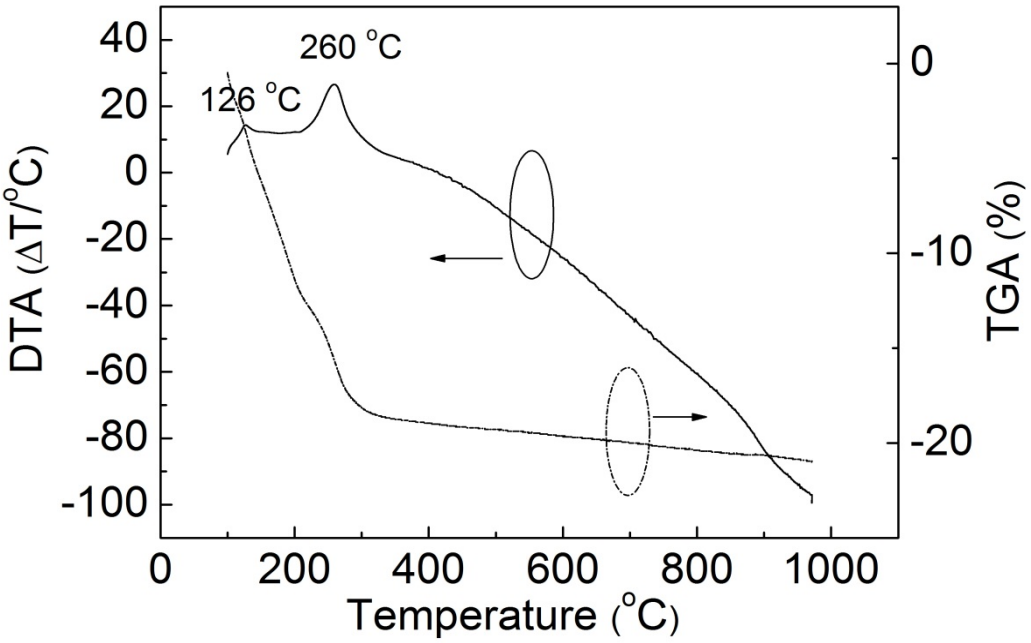

Figure 5-1 DTA/TGA curves of the dried CFO slurry.

X-ray diffraction patterns of the resultant CFO thick films annealed at different temperatures were shown in Figure 5-2. Although major peaks for $CoFe_2O_4$ were observed for the film annealed at 550°C, additional peaks (marked) due to Fe_2O_3 were also observed, indicating the process of CFO formation was not complete. With the rise of the annealing temperature, the complete formation of spinel phase was observed for films annealed above 600°C. Furthermore, these characteristic peaks of CFO phase became narrow, indicating an increase of their grain size with the increasing annealing temperature.

Typical surface morphology and cross-sectional picture of CFO composite thick films annealed at 700°C were shown in Figure 5-3. It can be seen from Figure 5-3(a) that the thick films have a rough surface due to agglomeration as in the case of synthesized CFO thin films reported in the literature [152]. The

roughness was attributed to the large thickness close to 10 μm, evidenced by its cross-sectional picture in Figure 5-3(b). It was far beyond the thickness of the reported ferrite films [126, 128].

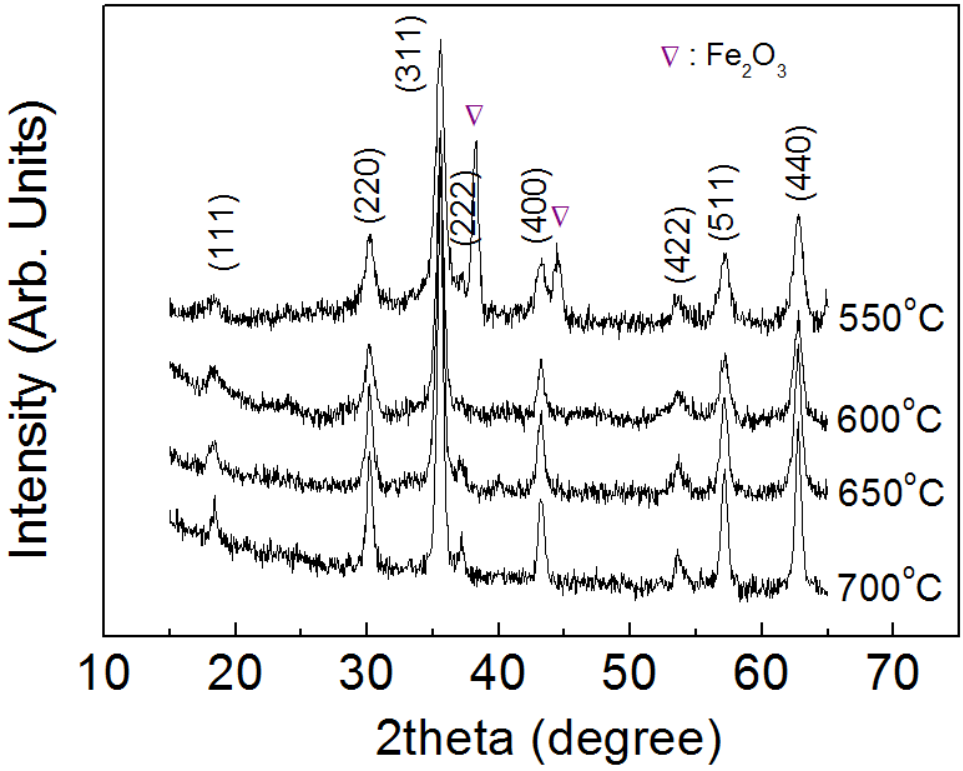

Figure 5-2 XRD patterns of CFO composite thick films annealed at different temperatures.

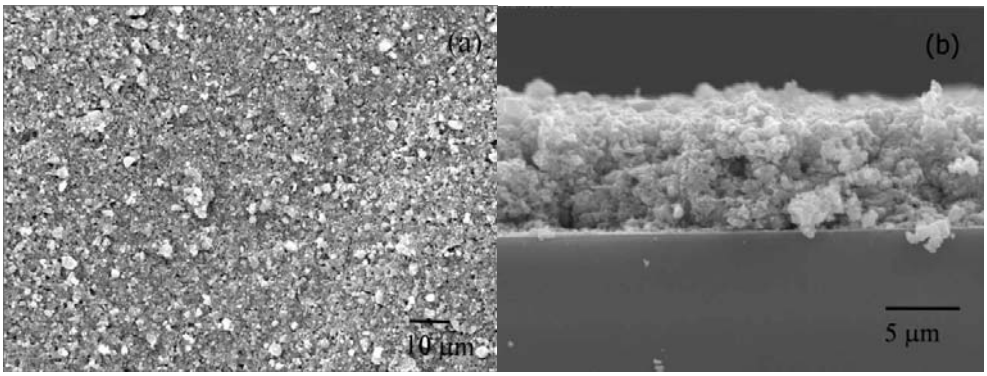

Figure 5-3 Typical surface morphology (a) and cross-sectional image (b) of CFO composite thick films annealed at 700°C.

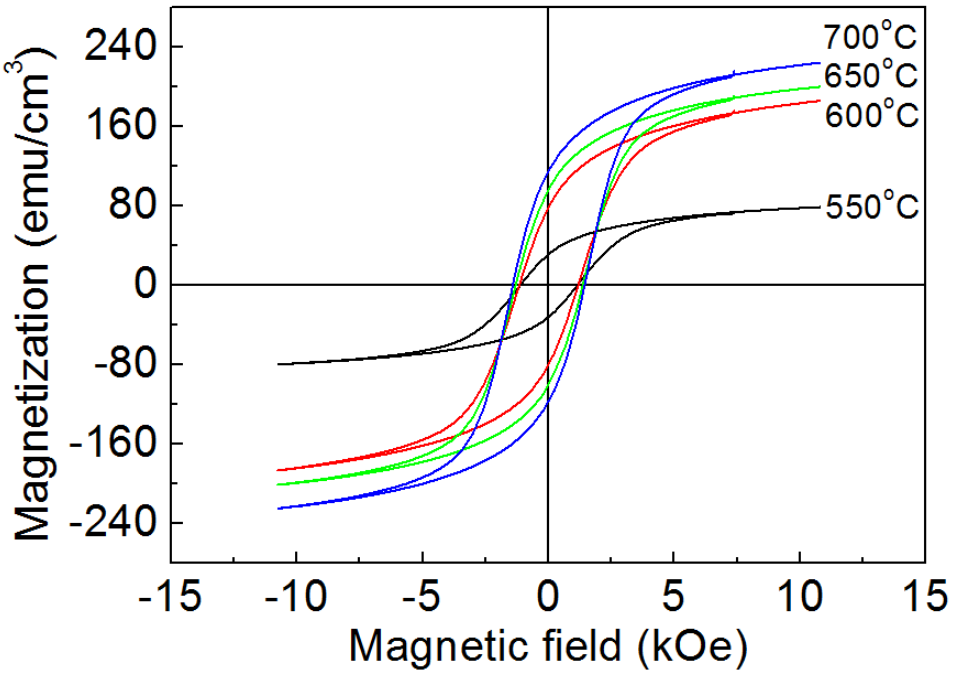

Figure 5-4 Magnetic hysteresis loops of CFO composite thick films annealed at different temperatures.

5.1.4 MAGNETIC HYSTERESIS LOOP

In-plane magnetic hysteresis loops are shown in Figure 5-4. It can be seen that all the films reach saturation below 8 kOe, because the CFO ferrite thick films were in a quasi-free state with negligible shear stress from the substrates compared to chemical synthesized CFO thin films [126] or pulse laser deposited CFO epitaxial thin films [153]. Furthermore, the present composite thick films showed the dependence of saturation magnetization (*Ms*) and magnetic coercivity (*Hc*) on the annealing temperature. With increasing annealing temperature, both *Ms* and *Hc* values exhibited a monotonic increase. The enhanced *Ms* values from 79 to 225 emu/cm^3 were due to the enlargement of average cobalt ferrite grains, which had been demonstrated in CFO bulks and thin films [126, 154]. In the CFO thin films [126], the *Ms* value was reported as

300 emu/cm^3. Compared with the present composite thick films, the higher *Ms* value of the CFO thin film was mainly caused by the higher annealing temperature.

The particles used in CFO composite thick films included two parts: one was the sol-gel synthesized particles with a small particle size of dozens of nanometer, and the other comprised CFO particles with a large average size of about 233 nm modified by high energy ball milling. Since the latter had been presintered at 1200^{o}C, the growth rates of both kinds of CFO particles under the annealing temperature of 700 ^{o}C were different, which resulted in the rough surface caused by non-uniform segregation and the increase of coercivity of CFO composite thick films from 1130 to 1434 Oe. Generally speaking, high coercivity can be obtained in systems with nanostructures or preferred orientations, such as thin films with preferred crystal textures or nanoparticles with a single domain diameter [155]. Furthermore, the single domain diameter of CFO was about 40 nm [155], which was much smaller than the average diameter of the present CFO composite thick films (above 100 nm). Therefore, the observed *Hc* in the composite thick film was mainly attributed to the magnetic multi-domain configuration of the CFO particles in the composites [155, 156].

5.1.5 ELECTRICAL CHARACTERIZATION

Room temperature impedance spectroscopy data for the CFO composite thick films are shown in Figure 5-5 for frequencies of 0.1 Hz to 1 MHz. Figure 5-5(a) shows a step-like decreasing trend for all the samples from 10 Hz to 10

kHz, and their specific impedances values were reduced by nearly three orders of magnitude.

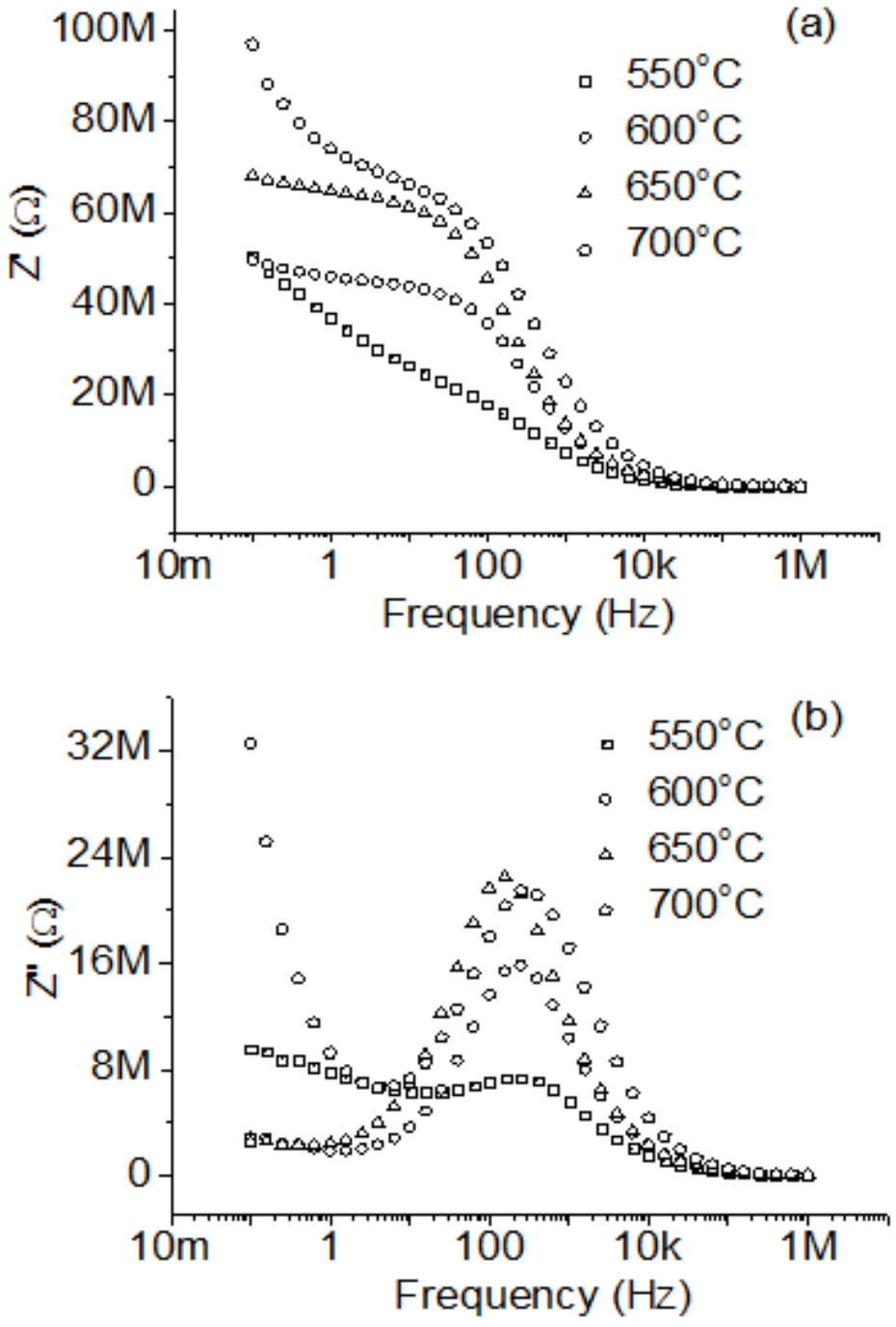

Figure 5-5 Frequency dependence of: (a) real and (b) imaginary parts of the complex impedance of CFO composite thick films at room temperature from 0.1 Hz to 1 MHz.

An apparent imaginary impedance peak appeared in all the samples and its amplitude roughly increased with increasing the annealing temperature from 550 to 650^{o}C, and almost keep stable with further increasing annealing temperature to 700^{o}C, as shown in Figure 5-5(b). It can be seen that the peak frequency was around 300 Hz, which was in the middle point of the step-like decreasing curve in real impedance spectra, indicating a relaxation behavior. This phenomenon had not been reported in the literature on CFO ferrite, but recent studies on multiferroic $BiFeO_3$ thin films and $BiFeO_3/CoFe_2O_4$ bilayer thin films showed a similar behavior [157, 158]. The relaxation peak was initially observed in $BiFeO_3$ thin films at 150^{o}C [157], but 100^{o}C for $BiFeO_3/CoFe_2O_4$ thin films [158], indicating that CFO was beneficial to shift this relaxation peak to the low temperature side. This was also the reason that we observed the present relaxation behavior at room temperature. Furthermore, the present composite thick films showed a similar characteristic frequency maxima (f_{max}), indicating the relaxation time was independent of the annealing temperature. Additionally, above 10 kHz, both real and imaginary curves merged together irrespective of the annealing temperature, while apparent dependence of diffusion phenomena on annealing temperature was observed below 10 Hz. Normally, the grain effect results in the high frequency impedance behavior, while grain boundary effect causes the low frequency phenomena [159]. The impedance spectroscopy independent of annealing temperature at high frequency side for the present composite thick films revealed that CFO grains were insensitive to the fast switch of applied A.C. electric field. However, low frequency diffusion behavior indicated a

remarkable grain boundary effect, which should be attributed to the increased aggregation caused by the higher annealing temperature.

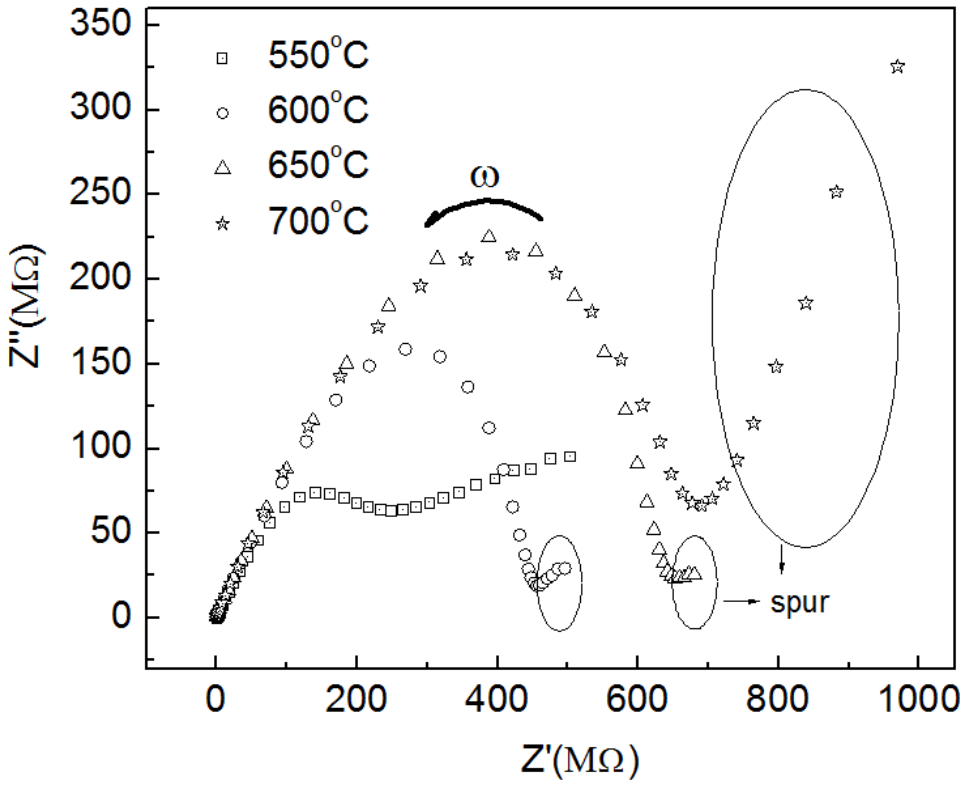

Figure 5-6 Nyquist plots of CFO composite thick films annealed at different temperatures, measured in the frequency range from 0.1 Hz to 1 MHz.

In order to further investigate the effect of grains and grain boundaries of CFO composite thick films, Nyquist plots (relation between real and imaginary impedance) at room temperature for all samples were shown in Figure 5-6. The irregular shapes of CFO thick films annealed at 550°C should be attributed to the mixture of the second phase. For the sample annealed above 600°C, it can be seen that an approximate semicircular arc was formed at the high frequency side. This semicircular arc was gradually expanded with increasing annealing temperature until 650°C, where it was nearly the same as the one annealed at 700°C, and the absolute value of impedance also reached the maximum,

indicating that CFO grain effect reached a stable state. On the other hand, the "spur" which appeared at the low frequency side was almost unchanged at 600 and 650°C. This "spur" became very large for the sample annealed at 700°C, revealing an increased grain boundary effect caused by more aggregation as mentioned above.

From the impedance spectroscopy analysis, we expected 650°C to be an optimized temperature for promising electrical properties. However, to further understand the mechanism in ion motion of the three different regions in Figure 5-5, A.C. conductivity spectra were deduced from the impedance spectroscopy data, and the results are presented and discussed below.

It is known that the A.C. conductivity of a composite thick film can be estimated from its impedance and phase angle through the following relationship,

$$\sigma^* = \frac{d}{AZ^*} = \frac{d}{A(Z'+iZ'')} = \frac{d(Z'-iZ'')}{A|Z|^2} \quad (5\text{-}1)$$

$$\sigma' = \frac{d\cos\theta}{A|Z|} \quad (5\text{-}2)$$

where d and A are the sample thickness and its effective area, θ is the impedance phase angle and $|Z|$ is the absolute value of impedance, Z' and Z'' are real and imaginary impedance, and σ^* and σ' are the complex conductivity and its real part, respectively, with the latter usually known as the A.C. conductivity. In terms of equation 5-2, we can obtain the frequency dependence of the A.C. conductivity in the whole measured frequency range.

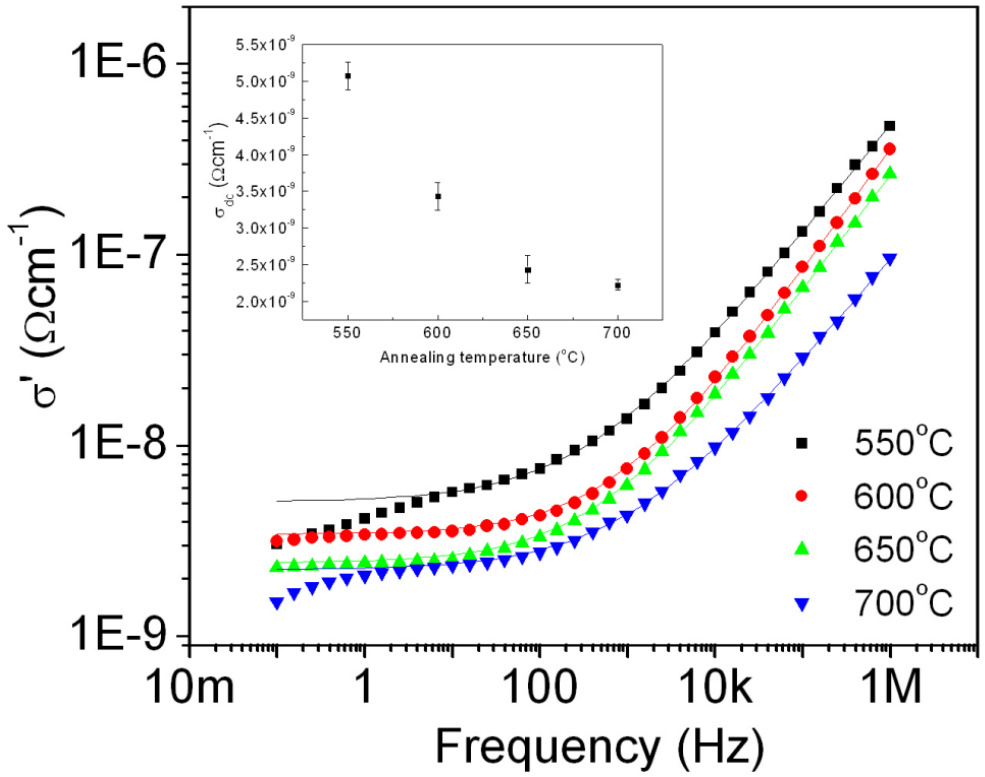

Figure 5-7 AC conductivity spectra of CFO composite thick films annealed at different temperatures. The inset is the estimated DC conductivity dependence on annealing temperature.

As can be seen in Figure 5-7, three different regions were observed in the A.C. conductivity spectra, which is consistent with the three zones mentioned in the impedance spectra. They are corresponding to the three effects that contribute to the D.C. conductivity [160]: (1) low frequency electrode effects, (2) intermediate frequency A.C. plateau, and (3) high frequency A.C. conductivity effect. It is clearly seen that low frequency electrode effects, represented by the deviation from the flat region of conductivity, were especially remarkable for the thick film annealed at 700°C, but very weak for the thick films annealed at 600 and 650°C. In addition, for the A.C. conductivity spectra at intermediate and high frequency ranges, the difference

in the trend decreased with increasing annealing temperature due to the increased impedance values. This can be attributed to the improved crystallization of composite thick films. Furthermore, the D.C. conductivity estimated from the power law [147] also showed a decrease with increasing annealing temperature, as can be seen in the inset of Figure 5-7. More detailed investigations on A.C. conductivity spectra will be presented in the following section.

Due to the lack of detailed impedance spectroscopy analysis of CFO thin films and bulk materials in literature, the data on $BiFeO_3/CoFe_2O_4$ bilayered thin films is introduced for comparison to our results [158], where the D.C. plateau and nearly constant loss (NCL) regime were also observed and both of them moved to high frequency with increasing measured temperature. This is similar to the present case of CFO composite thick films. However, the decreased dependence of $BiFeO_3/CoFe_2O_4$ bilayered thin films on measured temperature at high frequency side was attributed to the introduction of low conductive $BiFeO_3$. This hypothesis is confirmed by similar data for PZT/CFO multilayered thin films [106] in which insulating PZT was combined with CFO. Detailed analysis of electrical properties of CFO composite thick films will be presented in the following section.

5.1.6 BRIEF SUMMARY

Cobalt ferrite composite thick films were prepared on $Pt/Ti/SiO_2/Si$ substrates by a hybrid sol-gel processing. Through annealing at different temperatures, XRD spectra indicated that pure spinel phase was formed above 600^oC. A thickness of 10 μm was confirmed by cross-sectional SEM imaging.

Furthermore, with increasing annealing temperature, saturation magnetization and magnetic coercivity were increased. Room temperature impedance spectroscopy analysis indicated a relaxation behavior from 10 Hz to 10 kHz, and this relaxation behavior was strengthened with increasing annealing temperature. Complex Z' - Z'' plots revealed that the grain effect was the main contribution to the relaxation behavior for all the samples. Investigation on conductivity spectra via the universal dynamic response law indicated the appearance of the electrode polarization effect after annealing at 700^{o}C.

5.2 IMPEDANCE RELAXATION AND CONDUCTIVITY MECHANISM OF COBALT FERRITE COMPOSITE THICK FILMS

In the last section, an impedance relaxation behavior was observed in thick film structures of $CoFe_2O_4$ at room temperature. To understand more about this system, this section presents the detailed electrical investigations of cobalt ferrite thick films annealed at 600^{o}C in the frequency range 100 Hz-1 MHz and temperature range between 25 and 200^{o}C. Real and imaginary parts of impedance (Z' and Z'') in the above frequency and temperature domains suggested the concurrence of two relaxation regimes: one was induced by electrode polarization, and the other was attributed to the co-effect of grains and grain boundaries. The latter is totally different from its counterpart of bulk materials and has not been reported for other ferrites. Electrical modulus (M' and M'') further showed the crossover from the grain effect to the grain boundary effect with increasing temperature under the suppression of electrode polarization. A non-Debye relaxation behavior and two segments of frequency

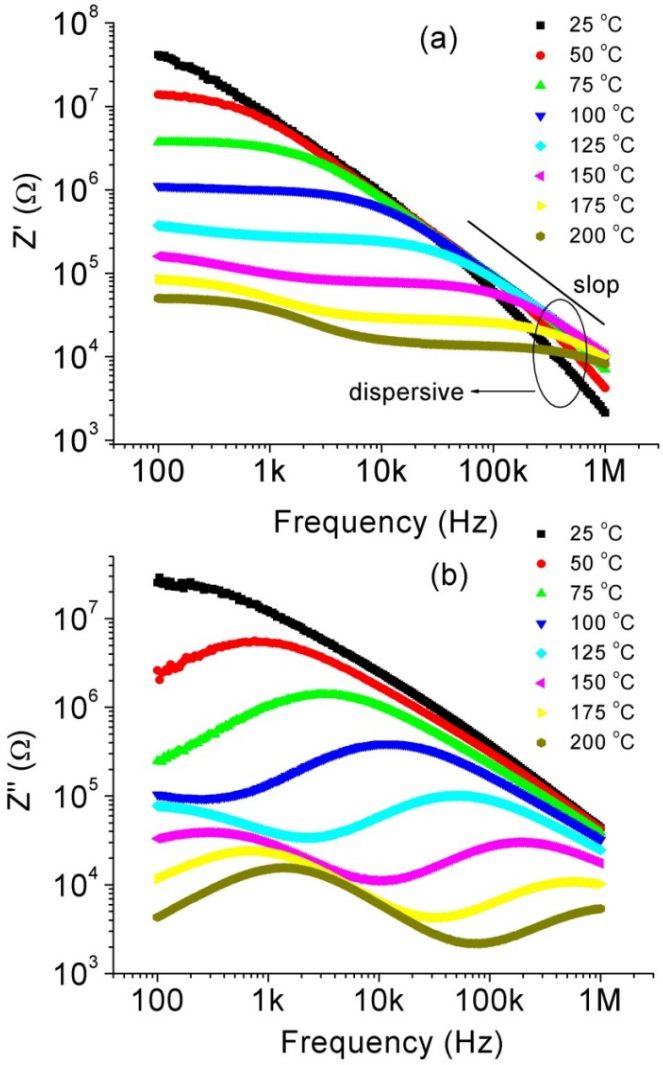

Figure 5-8 Frequency dependence of real impedance (a) and imaginary impedance (b) for $CoFe_2O_4$ composite thick film from 100 Hz to 1 MHz and between 25 and 200°C.

independent conductivity were observed in the dielectric spectra, which were also consistent with the results of A.C. conductivity spectra. In the conductivity spectra, double power law and single power law were separately applied to the co-effect from grains and grain boundaries and the electrode polarization effect. Moreover, the D.C. conductivity from both effects obeys the Arrhenius law well and their activation energies were matched to the ones calculated from imaginary impedance peaks.

5.2.1 IMPEDANCE RELAXATION BEHAVIOR

Figure 5-8(a) and (b) shows the variation of real and imaginary parts of impedance (Z' and Z'', respectively) in the frequency range from 100 Hz to 1 MHz and temperatures between 25 and 200^{o}C. A temperature-dependent Z' plateau was observed at the low frequency region at 50^{o}C followed by a negative slope at the high frequency side, indicating a crossover from the low frequency relaxation behavior to the high frequency dispersion phenomenon. Furthermore, the segment of nearly constant real impedance became dominant with increasing temperature, suggesting a strengthened relaxation behavior. This is similar to the behavior observed in multiferroic $BiFeO_3$ thin films above 150^{o}C, where a clear relaxation behavior was smoothed into the frequency window from the low frequency side due to the rising temperature [157]. When the measured temperature was above 100^{o}C, another step-like impedance behavior was smoothed into the frequency window from the low frequency side. In the meanwhile, it pushed the previous high frequency dispersive behavior out of the frequency window. Both these remarkable relaxations were hence concurrent above 100^{o}C. This phenomenon has never been found in ferrites, but an extremely weak impedance relaxation and another strong one were observed separately in different temperature ranges for recent PZT/CFO layered thin films, in which the strong relaxation found at high temperatures was attributed to the thermal activation mechanism [106].

Figure 5-8(b) shows a broad imaginary impedance peak appearing at 50^{o}C that is constantly shifted to higher frequencies with increasing temperature and finally is moved almost completely out of the frequency window at 200^{o}C.

Meanwhile, another broad peak appeared at low frequencies above 100°C and is also shifted to higher frequencies, which corresponded to both plateau relaxations observed in the real impedance spectra. The Arrhenius law was hence applied for both relaxations,

$$\tau = \tau_0 \exp(-\frac{E_a}{k_B T}),\ \tau = \frac{1}{2\pi f_p} \qquad (5\text{-}3)$$

where τ_0 is the characteristic relaxation time, E_a is the activation energy for the relaxation process, k_B is the Boltzmann constant, T is the absolute temperature and f_p is the peak frequency of imaginary impedance. The estimated activation energies from their respective imaginary peaks are 0.675 eV and 0.483 eV, and the characteristic relaxation times τ_0 are 8.01×10^{-15} s and 4.16×10^{-10} s, respectively.

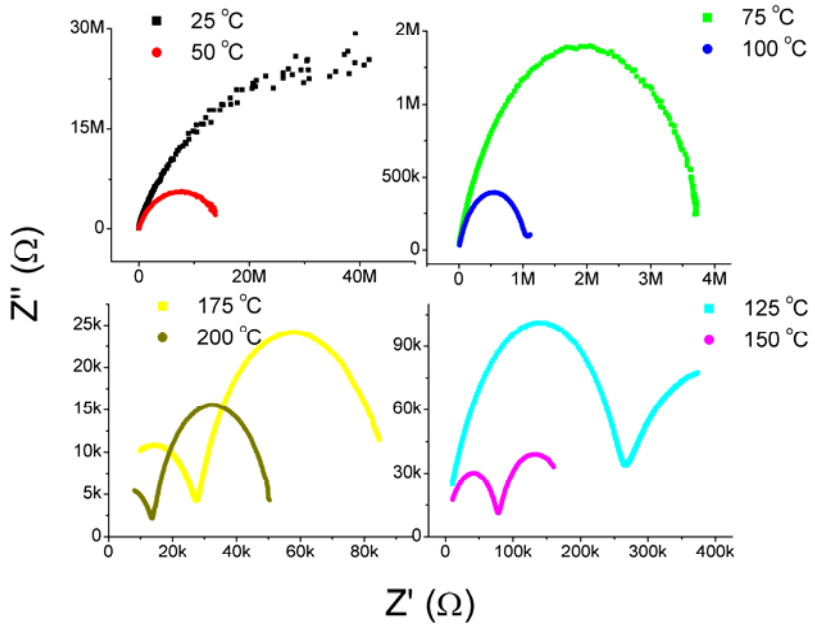

Figure 5-9 Nyquist plots of real and imaginary impedance for $CoFe_2O_4$ composite thick film at all measured temperatures.

Nyquist plots of the impedance data at different temperatures are shown in Figure 5-9. At 25^{o}C, a semicircular arc was observed and it became a whole semicircular arc at 75^{o}C, which should be attributed to the grain effect in CFO thick film. Beginning at 100^{o}C, another segment of arc appears from low frequency side. Furthermore, this arc is gradually spreading till 150^{o}C, where both arcs are comparable, corresponding to the two peaks appearing in imaginary impedance spectra. When the temperature finally reaches 200^{o}C, it can be seen that the second arc nearly transforms into a whole semicircular arc at the low frequency side and the initial semicircular arc degenerates into a segment of arc. This suggests a process in which the grain effect is gradually replaced by the grain boundary effect with increasing temperature. Additionally, during this process, the impedance decreases by four orders of magnitude due to the thermal activation mechanism. The rise of temperature caused the increase in conductivity and hence the decrease in impedance.

While the two Nyquist semicircular arcs in Figure 5-9 might lead us to think that the grain effect and grain boundary effect causing them are similar to those observed in other systems [106, 157], the activation energies estimated from Arrhenius law for both semicircular arcs suggest a different situation. Normally, the activation energy from grain boundaries is larger than that of grains [106]. This is also the reason why the grain boundaries could play a blocking effect in many ionic oxides due to their high potential energy barrier. In contrary, the so-called activation energy produced by grains in this study was higher than that of grain boundaries, which completely cancelled the barrier effect of grain boundaries. Therefore, we hypothesize that both grain boundary

and grain effects in the thick films co-contribute to the initial semicircular arc and the second semicircular arc that appears at high temperature is due to electrode polarization effect.

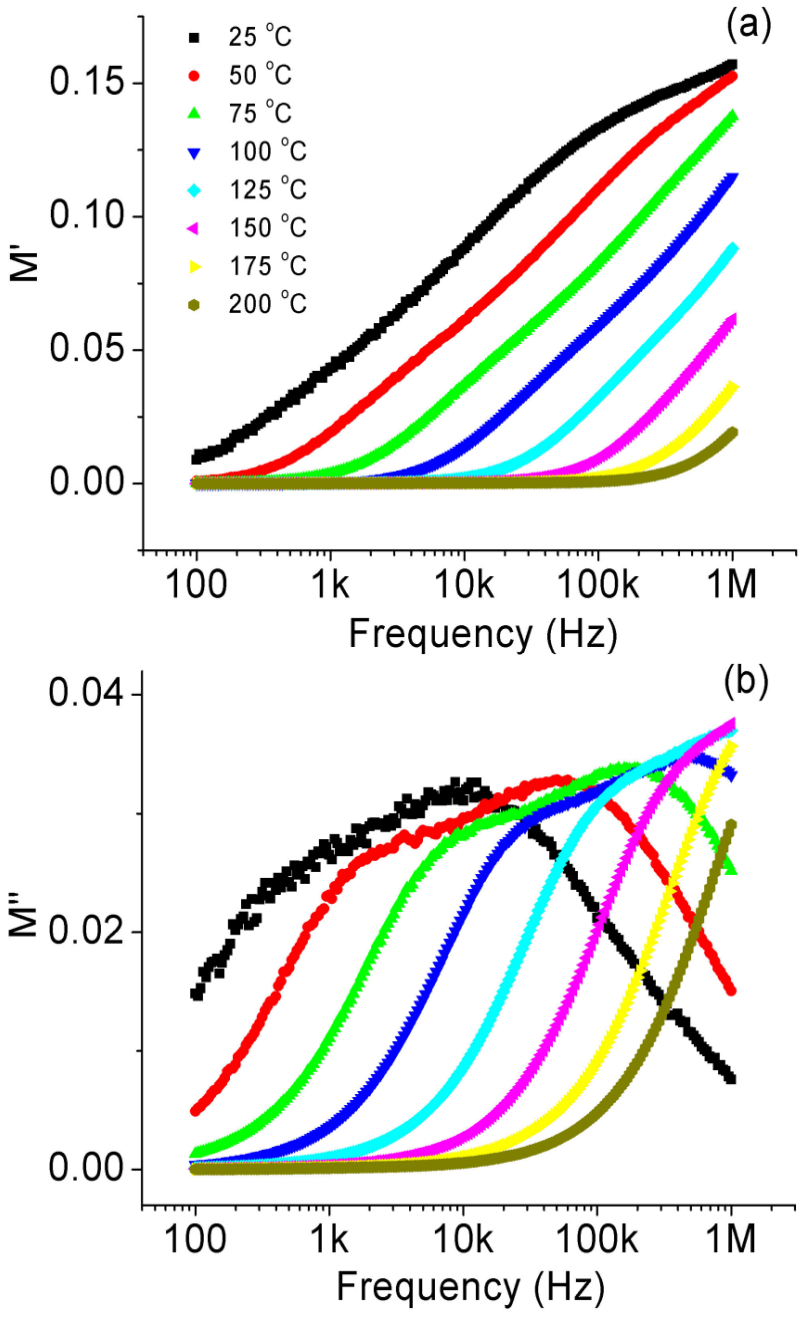

Figure 5-10 Frequency dependence of real (a) and imaginary electrical modulus (b) of $CoFe_2O_4$ composite thick film from 25 to 200°C.

5.2.2 ELECTRICAL MODULUS ANALYSIS

In order to demonstrate this point, electrical modulus formalism had been introduced due to its special advantage of suppressing the electrode polarization effects [161]. The electrical modulus is calculated from the following equation:

$$M^* = M' + jM'' = j\omega C_0 Z^* = j\omega C_0 (Z' - jZ'') \qquad (5\text{-}4)$$

where ω is the angular frequency and the geometrical capacitance is $C_0 = \varepsilon_0 A/d$ (d is the sample thickness, A is the electrode area, and ε_0 is the permittivity of vacuum, $8.854\times10^{-14} Fcm^{-1}$). Using equation (5-4), we can calculate the values of M' and M'' using the relationship $M' = \omega C_0 Z''$ and $M'' = \omega C_0 Z'$. The frequency dependence of M' and M'' at all temperatures are presented in Figure 5-10. Unlike the impedance spectroscopy with two well-separated relaxation behaviors, the real modulus in Figure 5-10(a) shows a nearly single relaxation behavior featured mainly by a positive slope shifting to high frequencies with the increase of temperature. Figure 5-10(b) shows broad peaks can be observed for temperatures from 25 to 100^{o}C. They also exhibit the same shift to high frequencies with increasing the temperature so that beyond 100^{o}C, the peak degenerates and finally disappears above 150^{o}C. This behavior demonstrates that the high temperature electrode polarization reflected in impedance spectra was completely suppressed here [138, 157]. Additionally, we noticed an inflexion point in the middle of the increasing real modulus for the samples measured between 25 and 100^{o}C, while the broad peak in imaginary modulus showed a depressed behavior in its central part. This was different from the modulus peaks of the other kinds of ferrites, including CFO

ferrite [138], Ni-Zn and Mn-Zn ferrites [137, 162], in which only a clearly and smooth relaxation behavior was observed. The present behavior indicates that this broad peak consists of two incomplete relaxation peaks, which are nearly merged together. This is also why we proposed that the impedance semicircular arc was caused by the combined effects from grains and grain boundaries effects. In the modulus curves, the relaxation peak at the low frequency side was caused by the grain boundary effect and the one at the high frequency side was induced by the grain effect.

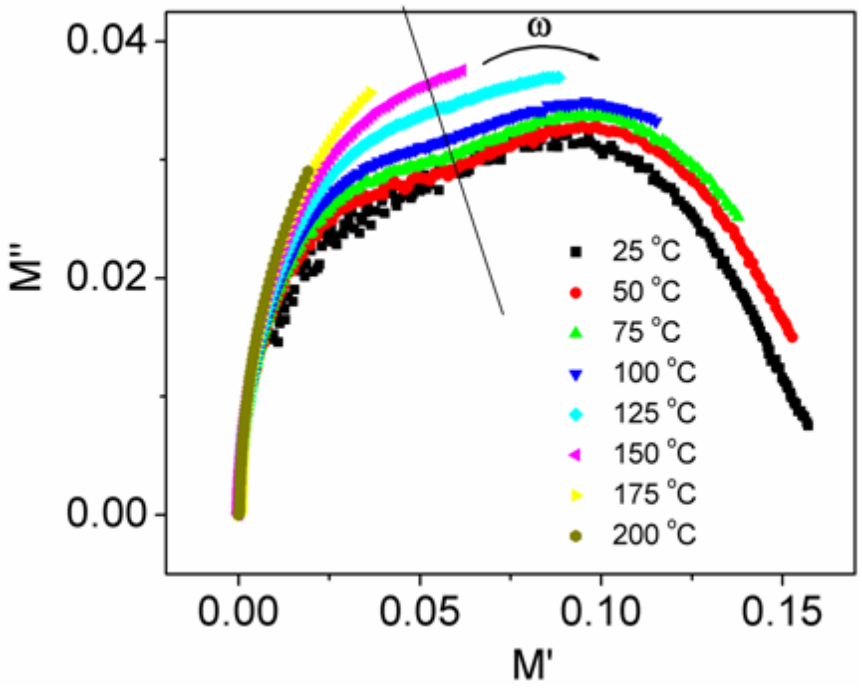

Figure 5-11 Real vs imaginary modulus plots of $CoFe_2O_4$ composite thick film at all measured temperatures.

Figure 5-11 shows the complex modulus of CFO thick films at all temperatures. Two incomplete semicircular arcs form a broad semicircular arc in the temperature range of 25-100^{o}C. With further increasing temperature, only a segment of the arc is left at the low frequency side, which is attributed to the

grain boundary effect induced by higher temperature. In the whole temperature range, we can see that the increase of measured temperature strengthens the grain boundary effect gradually and weakens the grain effect at the same time. This is similar to many materials [163, 164] with ions stimulated by higher temperature to hop over their barrier layers instead of hopping within their own sites.

From the results presented above, we can see that two impedance relaxations were initially observed in the CFO thick films, especially the concurrence phenomena above 100^{o}C, which was never reported in literature. The estimated activation energies from the two relaxations indicate that the effects of both grains and grain boundaries on the impedance relaxation appeared at a low temperature. Usually, both the grain and grain boundary effects are located at specific frequency and temperature ranges for homogeneous materials [157]. However, the present films showed an abnormal relaxation behavior, remarkably expressed in electrical modulus spectra, where the electrode polarization was suppressed.

Unlike the a single modulus peak found in other nanostructured ferrites [137, 138, 162], a temperature dependent crossover between the two peaks was observed, which might be induced by the hybrid microstructure consisting of two kinds of differently sized CFO particles. A similar phenomenon reported in literature for multiferroic PZT/CFO layered thin films confirmed this hypothesis [106]. Two electrical modulus relaxations were observed, but both were located in different temperature ranges without any overlapping. This should be attributed to the large conductivity difference between insulting PZT

and low resistivity CFO films. While the present CFO thick film was composed of the same CFO phase with different particle sizes, it was hence speculated that this special hybrid microstructure could be the main reason for the double relaxation behavior observed in our films.

5.2.3 DIELECTRIC SPECTRA STUDIES

Figure 5-12 shows the real and imaginary dielectric constants and the dielectric loss (ε', ε'' and tanδ) plotted against the frequency for all temperatures. As it can be seen in Figure 5-12(a), a strong dispersion is exhibited by the real dielectric constant at low frequencies. In addition, a weak relaxation was initially observed above 1 kHz for the sample below 100^{o}C and then gradually disappeared at high frequency when the temperature reached 100^{o}C. With further increasing temperature, a step-like relaxation behavior, which was similar to a Debye relaxation, was smoothed into the frequency window from the left side. In the meanwhile, a corresponding dielectric loss peak was observed in Figure 5-12(b) above 100^{o}C. Furthermore, this peak was moving to the high frequency side along with a reduced peak loss value. It was noticed that the temperature dependent peak frequency in this figure did not obey Arrhenius equation as other materials, suggesting this step-like relaxation to be of non-Debye type.

The imaginary dielectric constant versus frequency is shown in Figure 5-12(c), where no peak was observed in the measurable frequency range, but two weak relaxation behaviors were observed in the temperature range of 25-100^{o}C and 125-200^{o}C located at different frequency ranges, respectively. Besides, two negative slopes of the straight lines in the log-log plot were observed in Figure

5-12(c). Moreover, both of them were moving to the high frequency side with increasing temperature. This was the result of the frequency independent conductivity [165].

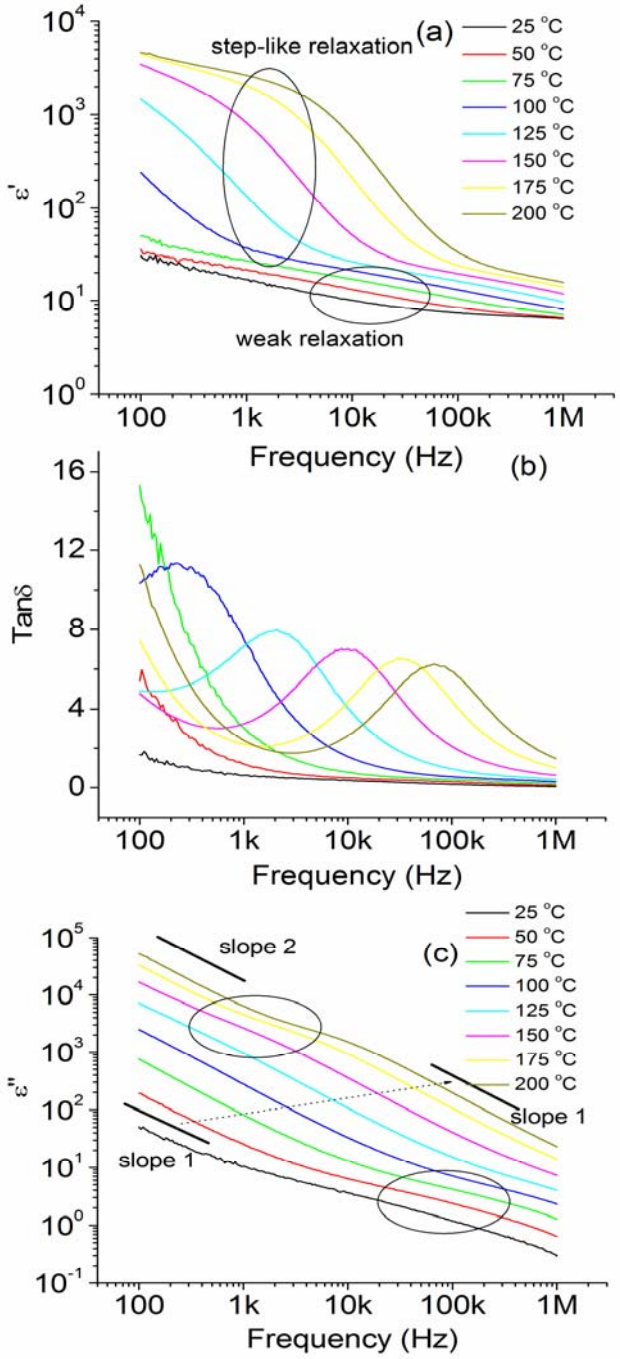

Figure 5-12 Frequency dependence of real dielectric constant (a), dielectric loss (b), and imaginary dielectric constant for $CoFe_2O_4$ composite thick film from 25 to 200°C.

5.2.4 AC CONDUCTIVITY MECHANISM

The real conductivity measurements are usually adopted for studying the ion motion of ionic oxides, glasses or melts, which can be estimated using Equation 5-2. The real conductivity spectra are presented in Figure 5-13(a). A monotonously increasing conductivity curve is observed at 25^{o}C and a plateau is smoothed into the frequency window from the left side above this temperature, which corresponds to the slopes in Figure 5-12(c), demonstrating a constant conductivity at low frequency. At high frequency, there was an exponentially increasing conductivity that moved to the right side of this frequency window along with the conductivity plateau in all temperature ranges, which is usually called the nearly constant loss regime (NCL) in literature [166, 167], also reflected in Figure 5-12(c). According to the jumping relaxation mode [168], the frequency independent plateau at a low frequency for higher temperatures is attributed to the long-range translational motion of ions that causes the D.C. conductivity. According to this model, the conductivity in the low frequency region is associated with the successful ion hopping to its neighboring vacant site due to the long time available for this event happened; such successive jumps result in a long-range transitional motion of ions contributing to the D.C. conductivity. At higher frequency (>10 kHz), two competing relaxation processes may be visualized: one is due to the same ion jumping back to its initial position, i.e., unsuccessful hopping, and the other is the relaxation of neighboring ions with respect to the ion's position, i.e., successful hopping. The increase in the ratio of successful to unsuccessful ion

hopping results in a more dispersive conductivity at higher frequency. For the present conductivity plateau, the data were fitted to a double power law [168],

$$\sigma' = \sigma_{dc} + Af^{n_1} + Bf^{n_2} \qquad (5\text{-}5)$$

where σ' is the real conductivity, σ_{dc} is the transitional hopping giving the long-range electrical transport in the long time limit, and the coefficients A, B and exponents n_1, n_2 are constants dependent on the temperature and intrinsic material properties [168, 169]. The terms Af^{n_1} and Bf^{n_2} characterize the contributions from grains and grain boundaries, respectively. As it can be seen in Figure 5-13(a), the solid lines are perfectly fitting to the experimental data. Moreover, the estimated σ_{dc} also obeys the Arrhenius-like law,

$$\sigma_{dc} = \sigma_0 \exp(-\frac{E_a}{k_B T}) \qquad (5\text{-}6)$$

where σ_0 is a constant, E_a is the activation energy, k_B is the Boltzmann constant, and T is the absolute temperature, as can be seen in Figure 5-13(b). This indicates that the ions are more inclined to hop to their nearest neighbor. Furthermore, the activation energy calculated here was close to 0.675 eV as mentioned above from the imaginary impedance. In addition, the values of the parameters n_1 and n_2 are mostly located in the range of (0,1), which corresponds to a short-range transitional hopping motion. The temperature dependences of n_1 and n_2 are presented in Figure 5-13(c); it is clear that both values are very close, due to the comparable grain and grain boundary effects. Furthermore, both of them exhibit a peak in the temperature range from 75 to 125^{o}C, which

corresponds to the onset of the crossover from the grain contribution to grain boundary contribution which is supported by frequency and temperature dependent modulus plots. It must also be highlighted that both parameters are close to or larger than 1 at 100 and 125^{o}C, which corresponds to just a few localized or reorientational hopping motion [169].

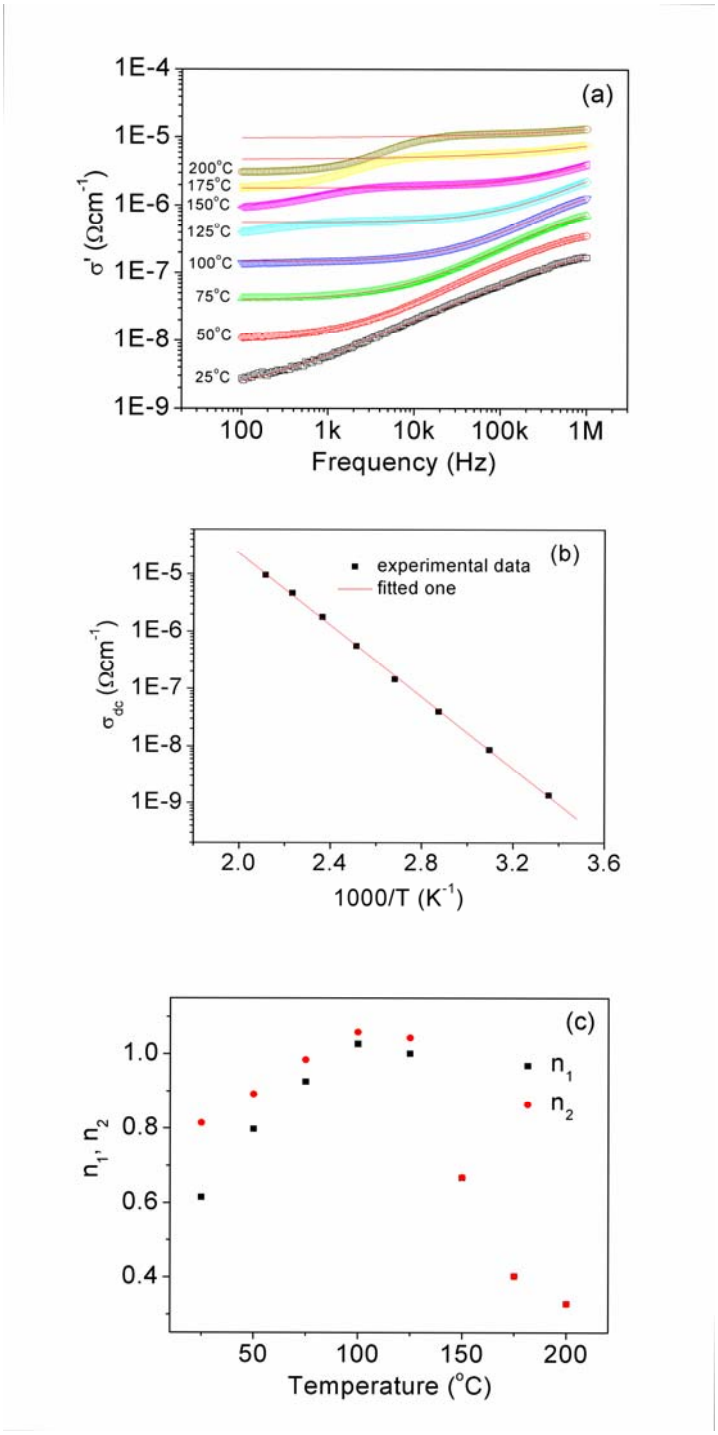

Figure 5-13 Frequency dependence of real conductivity and its fitting curves from double power law (a), temperature dependent of dc conductivity and its fitting curve from Arrhenius law (b), and double power parameters at all measured temperatures (c).

Additionally, when the temperature was above 100°C, a conductivity tail appeared at the low frequency side, such as the situation happening at 125°C,

which was usually believed to be the electrode polarization effect [170, 171]. Following this tail, another plateau was observed at low frequencies with further increasing temperature. This behavior has never been reported before. This is the reason why a whole Nyquist semicircular arc on electrode polarization effect was rarely found in literature. For the present case, we can see that the impact of this electrode polarization effect on the real conductivity is similar to behavior of the conductivity spectra resulted from the co-effect of grains and grain boundaries. Its D.C. plateau, which is corresponding to the slope 2 in the imaginary dielectric constant, was also moving to the high frequency as well as the NCL regime with the rise of temperature. Because this part is mainly contributed by the electrode polarization effect, a single power law was hence applied,

$$\sigma' = \sigma_{dc} + Af^{n} \qquad (5\text{-}7)$$

It was noticed that the fitted *n* value from Figure 5-13(a) was 1.12, indicating a localized or reorientational hopping motion, which should be attributed to the Au/Ti electrode layer. Furthermore, its D.C. conductivity was also fitted to the Arrhenius law and the estimated activation energy was nearly the same as the value calculated from the imaginary impedance, demonstrating again the contribution of electrode polarization to the low frequency semicircular arc in Nyquist plots.

5.2.5 Brief summary

Detailed studies of temperature- and frequency-dependent impedance of the typical CFO composite thick film were conducted. Two relaxations were

observed in the impedance spectra corresponding to the two semicircular arcs in Nyquist plots. The high frequency semicircular arc was induced by the co-effect of grains and grain boundaries, whereas the low frequency semicircular arc was due to the electrode polarization effect. Electrical modulus studies demonstrated that the grain effect was decisive below 100^{o}C, while the grain boundary effect played a more important role above this temperature. Non-Debye relaxation was subsequently observed in the dielectric spectra, and imaginary dielectric constant spectra further indicated two segments of frequency independent conductivity, which was demonstrated in the real conductivity spectra. In the conductivity spectra, on the one hand, the D.C. plateau at high frequency obeyed the double power law along with two similar power parameters, indicating the comparative contribution from grains and grain boundaries. The peak in temperature dependent power parameters further suggested the crossover from the grain effect to the grain boundary effect. Moreover, the D.C. conductivity well obeyed the Arrhenius law and the estimated activation energy was the same as the one calculated from high frequency imaginary impedance peaks. On the other hand, the other D.C. plateau at low frequency obeyed the power law, and its power parameter was 1.12, suggesting a localized or reorientational hopping motion probably induced by the Au/Ti layer. In addition, the activation energy calculated from its fitted D.C. conductivity showed the same value of grain effect to the one from low frequency imaginary peaks, demonstrating the contribution of electrode polarization to the low frequency Nyquist semicircular arc.

CHAPTER 6 DEPOSITION OF MULTIFERROIC THICK FILMS AND PROPERTIES STUDIES

This chapter is divided into six sections to present the process of fabricating CFO-PZT thick films, properties characterizations and physical mechanism, thick films structural optimization, ferroelectric and dielectric properties improvement, ferromagnetic properties optimization, dielectric relaxation and conductivity mechanism. All of them will be discussed one by one.

6.1 PREPARATION AND CHARACTERIZATION OF $CoFe_2O_4$-$Pb(Zr_{0.53}Ti_{0.47})O_3$ COMPOSITE THICK FILMS BY HYBRID SOL-GEL PROCESSING

6.1.1 INTRODUCTION

In Chapter Four we described our attempt to synthesize CFO-PZT thick films realized using screen printing, and multiferroic behavior has been observed in these films. However, the intrinsic restriction of this method was that the films fabricated using this method exhibited lots of porosities, which degraded their ferroelectric properties. A hybrid sol-gel process was hence adopted to replace screen printing.

In this section, we present the fabrication and characterizations of CFO-PZT multiferroic thick films realized using hybrid sol-gel and nanoparticle technique as well as their phase structural, ferromagnetic and ferroelectric

properties. Experimental results will show the strong effect of annealing temperature on these above mentioned properties. Discussion and explanations will also be presented.

6.1.2 Fabrication process

6.1.2.1 Preparation of PZT and CFO nanoparticles

PZT commercial powder (APC-850) was firstly dry milled for 20 h using high energy ball milling (HEBM) and then milled for another 4 h with addition of 5 wt% organic vehicle (ESL400) as dispersion agent. CFO powder was prepared from solid-state reaction using Fe_2O_3 and Co_3O_4 as raw materials. Both powders were first mixed together and milled for 1 h by HEBM, then annealed at 1100^{o}C for 2 h after pressed as a bulk disk. The calcined body ceramics were crashed into powder using roll-milling and subsequently high-energy ball milling for 20 h to obtain nanoparticles. Five weight percent organic vehicle (ESL400) was added into the resultant nanoparticles and milled for another 4 h to adjust powder dispersion.

X-ray diffraction (XRD) results of these nanoparticles are shown in Figure 6-1. It is clearly seen from the figure that the peaks could be broader and that their amplitudes also change, showing that the respective preferential orientations are modified by the high energy ball milling. The powder size was calculated according to the equation below:

$$d = \frac{K * \lambda}{B * \cos\theta_B} \qquad (6\text{-}1)$$

where d is the size of crystallite, K is constant dependent on crystal shape (0.89), λ is the X-ray wavelength, B is the full width at half maximum (FWHM) and θ_B is the Bragg angle. Using the data shown in Figure 6-1, the average crystal size can then be deduced to be about 203 nm for the CFO nanoparticles and 460 nm for the PZT nanoparticles.

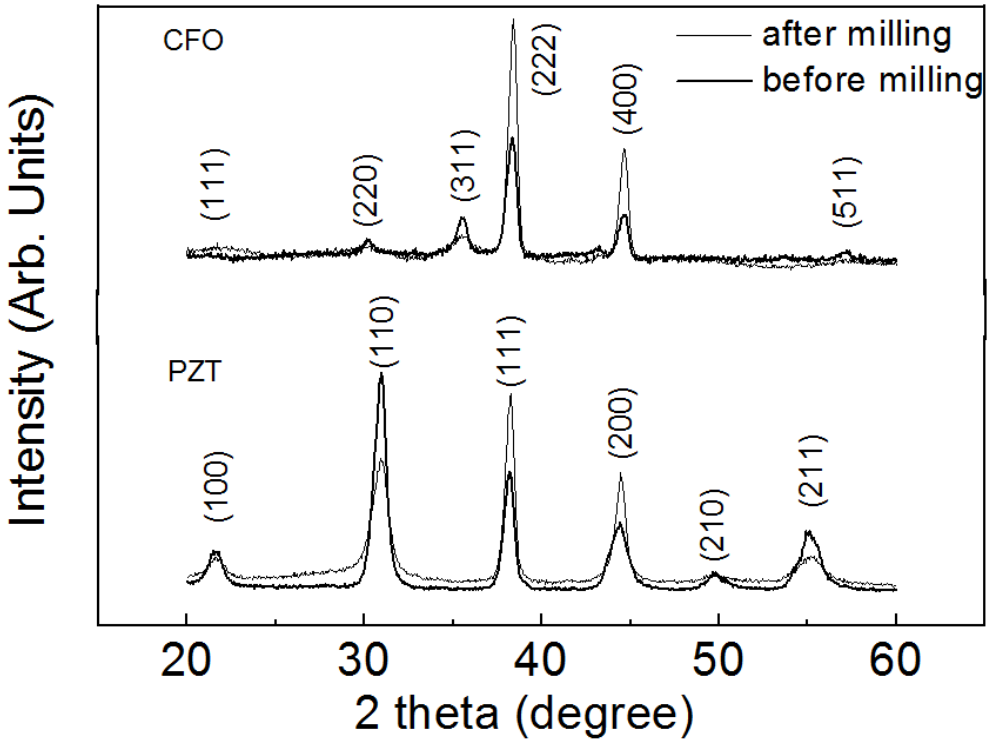

Figure 6-1 The effect of high energy ball milling on the X-ray diffraction patterns of CFO and PZT powder.

To decrease the nanoclusters in the milled green powder, the organic vehicle ESL400 was used to make the particle dispersion. Firstly, a solution of 5 wt% of ESL400 was added into PZT powder and CFO powder respectively before further milling. The dispersed particles were then dissolved into ethanol with a ratio of 5 mg: 30 ml and ultrasonically mixed for 30 min for good dispersion. After having kept statically for 4-6 h, the dispersed particles were

measured by Zeta Sizer (Nano-ZS), and the obtained particle size distributions of both PZT and CFO nanoparticles are given in Figure 6-2. It can be seen that the PZT nanoparticles are distributed in a wide range from 70 to 600 nm with a peak location at around 200 nm. On the other hand, the CFO nanoparticles are distributed from 90 to 400 nm, with a narrower range than that of PZT nanoparticles and the distribution peak at less than 200 nm, which are consistent with the results calculated from FWHM.

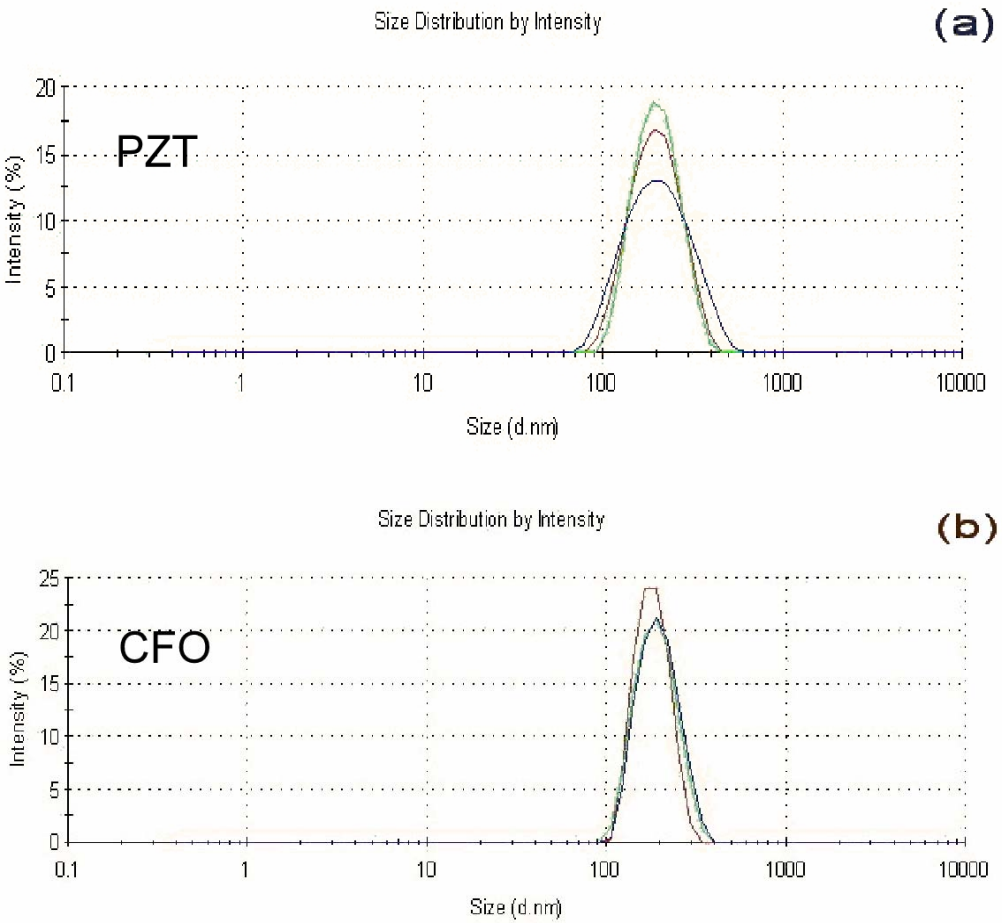

Figure 6-2 Size distribution of PZT and CFO particles dispersed into ethanol as measured using the Zeta Sizer (Nano-ZS).

Furthermore, the direct size evidence of two kinds of nanoparticles size can be seen in Figure 6-3. These nanoparticles were observed using

transmission electron microscope (TEM-JEOL2010), and the results are in good agreement with the ones from size distribution analysis and XRD calculation.

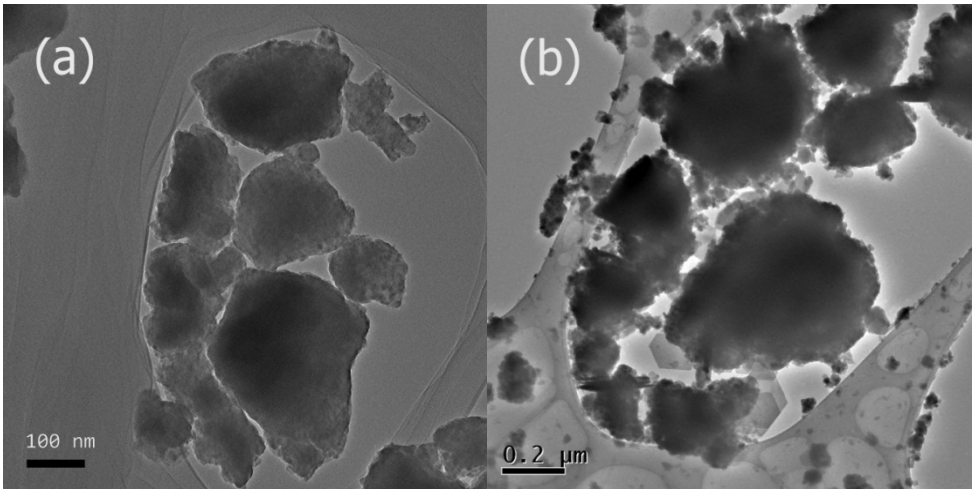

Figure 6-3 Typical transmission electronic microscopes of CFO (a) and PZT (b) nanoparticles.

6.1.2.2 PREPARATION OF PZT SOL-GEL SOLUTION

Tetraisopropyl titanate ($[(CH_3)_2CHO]_4Ti$) and acetylaceton ($CH_3COCH_2COCH_3$) were firstly mixed and stirred at 80^{o}C for 10 min. Lead acetate ($(CH_3COO)_2Pb{\cdot}3H_2O$) with additional 10 mol% was added into the solution to compensate the lead loss during annealing. After stirring for another 10 min at 120^{o}C, zirconium acetylacetone ($[CH_3COCH{=}C(O\text{-})CH_3]_4Zr$) was added into the above solution and stirred at 220^{o}C for 10 min. The resultant solution was yellowish and clear. The solution was transferred into the vacuum oven to keep for 4 h at 100^{o}C to obtain a PZT xerogel. Subsequently, the PZT xerogel was dissolved into 2-methoxyethanol ($CH_3OC_2H_4OH$) to get 0.3 M of PZT sol-gel solution.

6.1.2.3 PREPARATION OF PZT AND CFO SLURRY

To prepare the PZT slurry, PZT nanoparticles were mixed with the PZT sol-gel solution with the mass ratio of 2: 3 and milled for 15 h in an agate bowl, and the yellowish sticky PZT slurry was then collected. By using the PZT slurry, the thickness of films which can be obtained is increased up to several dozens of micrometers [172, 173]. The PZT slurry was further utilized to avoid the negative effect of the low resistivity exhibited by the CFO phase on the ferroelectric and dielectric properties in multiferroic thick films.

CFO nanoparticles were dispersed into the PZT sol-gel solution with the mass ratio of 1: 15 and milled for 15 h in the agate bowl. The mass ratio of CFO to PZT was kept low to avoid possible negative effects to dielectric and ferroelectric properties of the final films. On the other hand, the selected CFO percentage should be high enough to produce a detectable magnetic signal. After milling, a black CFO slurry was obtained. In this process, the PZT sol-gel solution acted as the matrix to disperse and carry the CFO nanoparticles.

6.1.2.4 DEPOSITION OF LAYERED THICK FILMS

The flow chart detailing the fabrication process of CFO-PZT multiferroic thick films is given in Figure 6-4. Three kinds of solutions and slurries were spin-coated on the $Pt/Ti/SiO_2/Si$ substrate according to the sequence in the schematic diagram depicted in Figure 6-5. Two CFO slurry layers and three PZT slurry layers were alternatively deposited as well as two PZT thin films layers as the initial buffer layer and the final cap layer. The spin coating speed and time were 3000 rpm and 30 s followed by baking at 250^{o}C and pyrolyzing at 500^{o}C for 2 min, respectively.

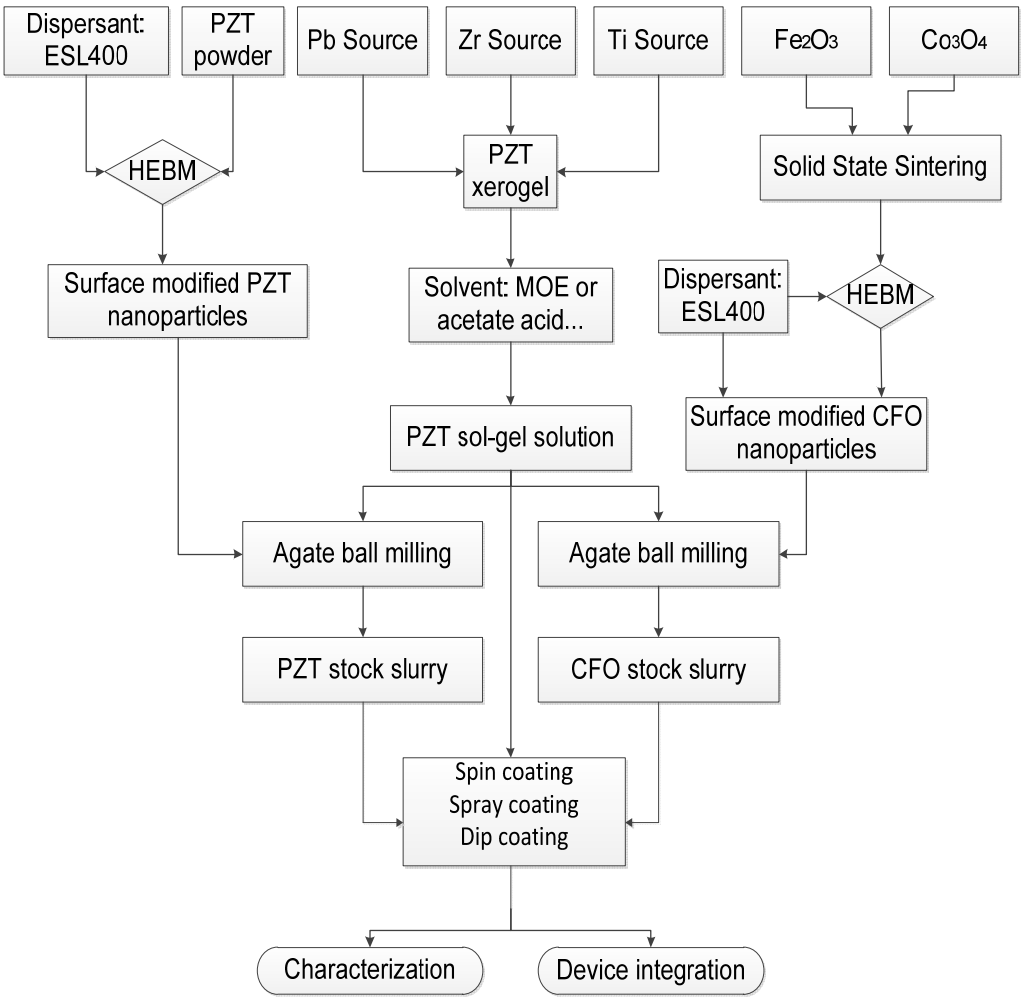

Figure 6-4 The flow chart of the hybrid process of fabricating multiferroic CFO-PZT thick films.

6.1.2.5 Fabrication and characterizations of thick films

The thick films were annealed from 600°C to 750°C for 1 h in air. Gold was then sputtered onto the thick films as top electrodes with each size of 0.5 mm × 0.5 mm. It is noticed that the surface of thick films is not as smooth as that of thin films. As such, the gold electrode was deposited to 200 nm for proper measurements of electric properties. In addition, the adhesion-promoter Ti layer between our CFO-PZT thick films and the Au electrode was also deposited to 20 nm in order to ensure a more effective adhesion.

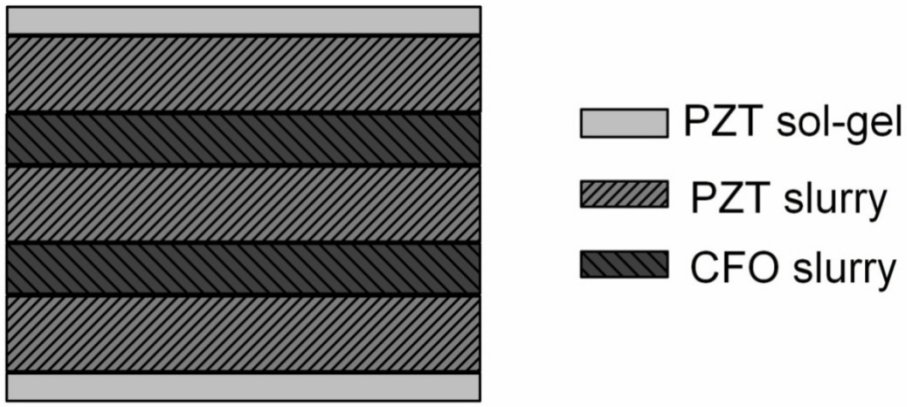

Figure 6-5 Schematic diagram of CFO-PZT layered structures.

6.1.3 RESULTS AND DISCUSSION

The thickness of one sol-gel coated PZT layer was about 60 nm as measured by the surface profiler, much less than the average size of CFO nanoparticles of ~200 nm. As a direct consequence, the spin-coated single CFO film would not be smooth due to the CFO particle size which is larger than the thickness of the sol-gel coated thin film, resulting in large film surface roughness. For this reason, spin-coating PZT slurry on the top of the CFO layer was adopted to reduce the interfacial roughness. Since the thickness of the PZT slurry-formed film was of about 600 nm per layer, which was about three times of that of CFO slurry formed film, the CFO layer between two PZT slurry layers was largely submerged. In addition, the PZT slurry was also used for adjusting the total thickness of resultant films. In the early work on hybrid techniques [56, 117], adjusting the ratio of sol-gel solution and nanoparticles was used to realize thick films so as to meet different requirements. Finally, a PZT sol-gel solution was coated as a top cap layer to reduce the concentration of air pores in the final CFO-PZT multiferroic thick films.

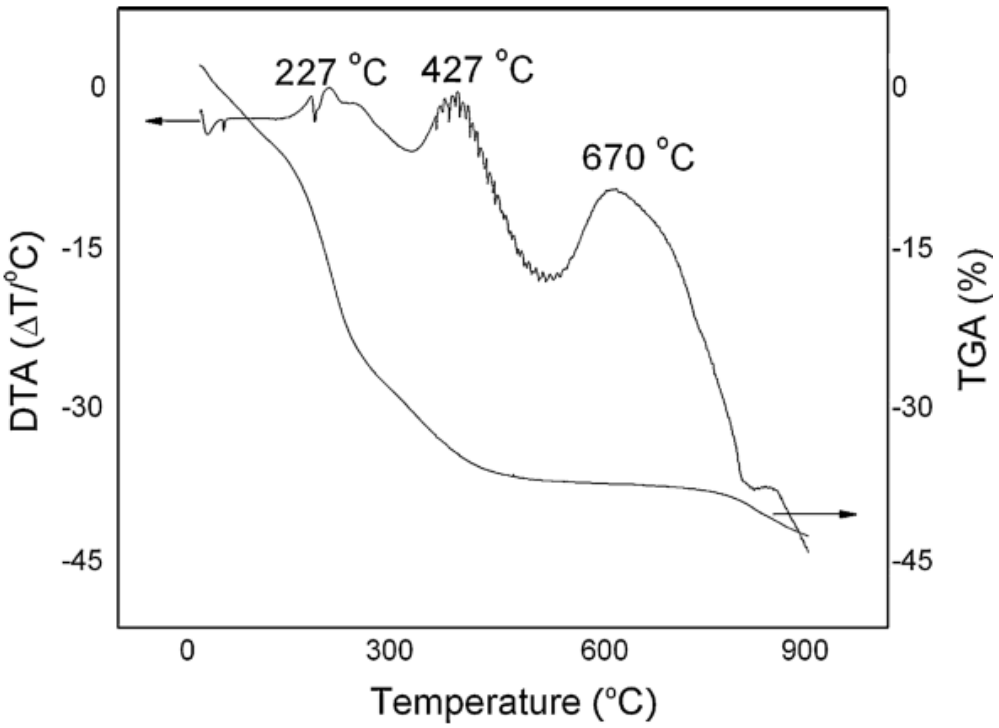

Figure 6-6 TGA and DTA results of PZT xerogel from room temperature to 1000°C with a heating rate of 2°C/min.

TGA and DTA curves of PZT xerogel are shown in Figure 6-6. TGA yielded a weight loss of 37% before 500°C, and then not much weight loss up to 900°C. In the DTA curve, the peak before 100°C was attributed to the organic solvent evaporation. The decomposition and combustion of the bound organic species in the xerogel contributed to the exothermic peaks before 450°C. The other peak around 670°C without significant weight loss indicated the formation of the perovskite phase, whereas the formation of pyrochlore phase occurred in the range from 427 to 670°C. Based on the DTA and TGA results, it was noted that the main weight loss occurred at 227 and 427°C, and thus a drying step at 250°C and a pyrolyzing step at 500°C were adopted in our fabrication process.

XRD measurement results are shown in Figure 6-7. It can be seen that only PZT and CFO phases exist and no other detectable impurity phases were presented in the film. The SEM micrographs of cross-sectional thick films are shown in Figure 6-8. PZT and CFO nanoparticles were mixed together and it was difficult to identify their layer boundaries as expected. It is worth noting that, as the thickness of films decreased the size of the crystal grains grew, and more pores appeared with increasing the annealing temperature. When the temperature was increased to 700°C and above, the Pt bottom electrode peeled off from substrate due to the hill-lop effect on the substrate and brought with invalid thickness estimation.

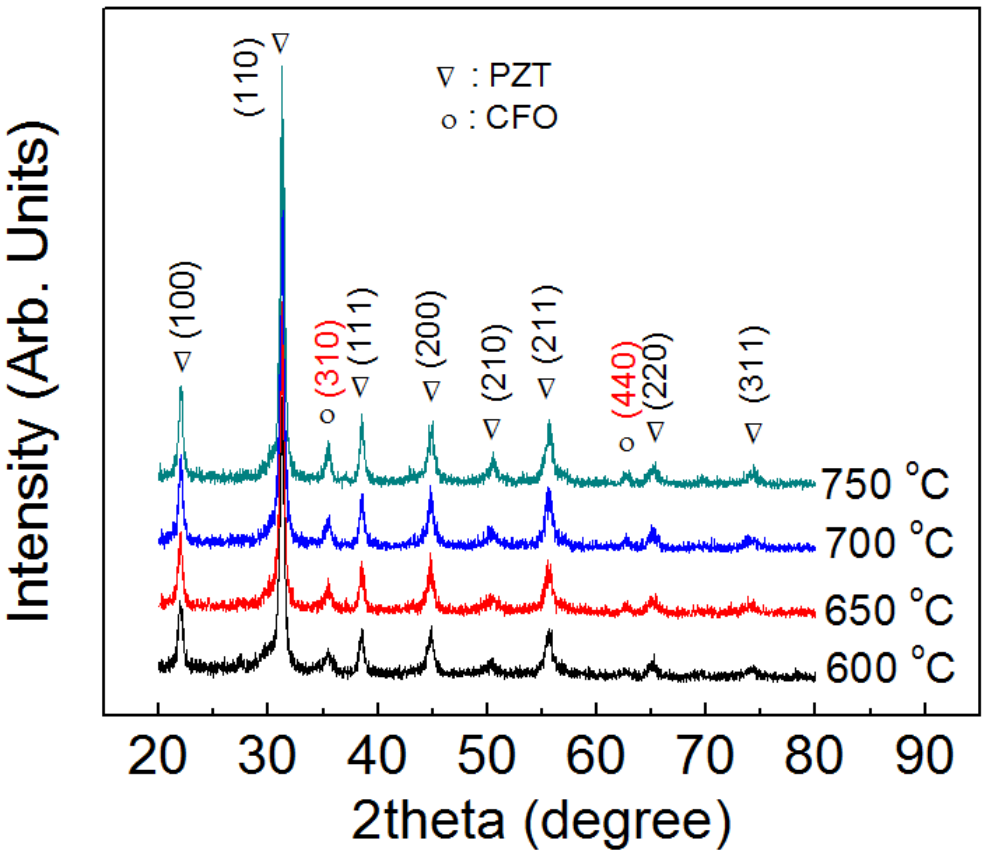

Figure 6-7 X-ray diffraction curves of CFO-PZT multiferroic thick films at different annealing temperatures.

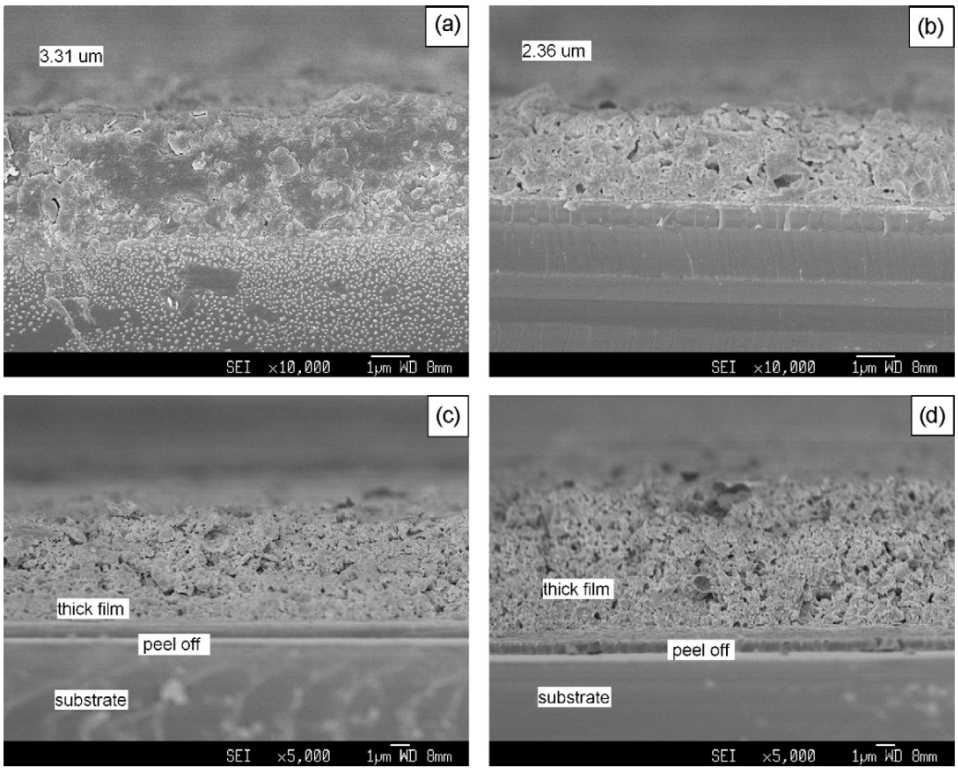

Figure 6-8 SEM cross-sectional microphotos of multiferroic thick films annealed at (a) 600°C, (b) 650°C, (c) 700°C, and (d) 750°C.

To characterize ferroelectric and ferromagnetic behaviors, ferroelectric polarization and coercive electric field and magnetic hysteresis loops are shown in Figure 6-9. It can be seen from Figure 6-9(a) that saturated polarization (P_s) and remanent polarization (P_r) decreased with the increasing annealing temperature and reached maxima of 33.3 μC/cm^2 and 17.3 μC/cm^2, respectively, at 600°C. This was attributed to the porous microstructure caused by the high annealing temperature, which brought down the densification of thick films and decreased their polarization. Due to the different electric field endurance, Figure 6-9(b) presents the typical ferroelectric hysteresis loop of the sample annealed at 600°C. The values of *Ps* and *Pr* are also larger than their counterparts of thin films [53], with the similar coercive electric field of 147.4

kV/cm. It indicates that the ferroelectric properties of multiferroic thin films could be improved in the form of thick film fabricated using our hybrid sol-gel and nanoparticle processing technique.

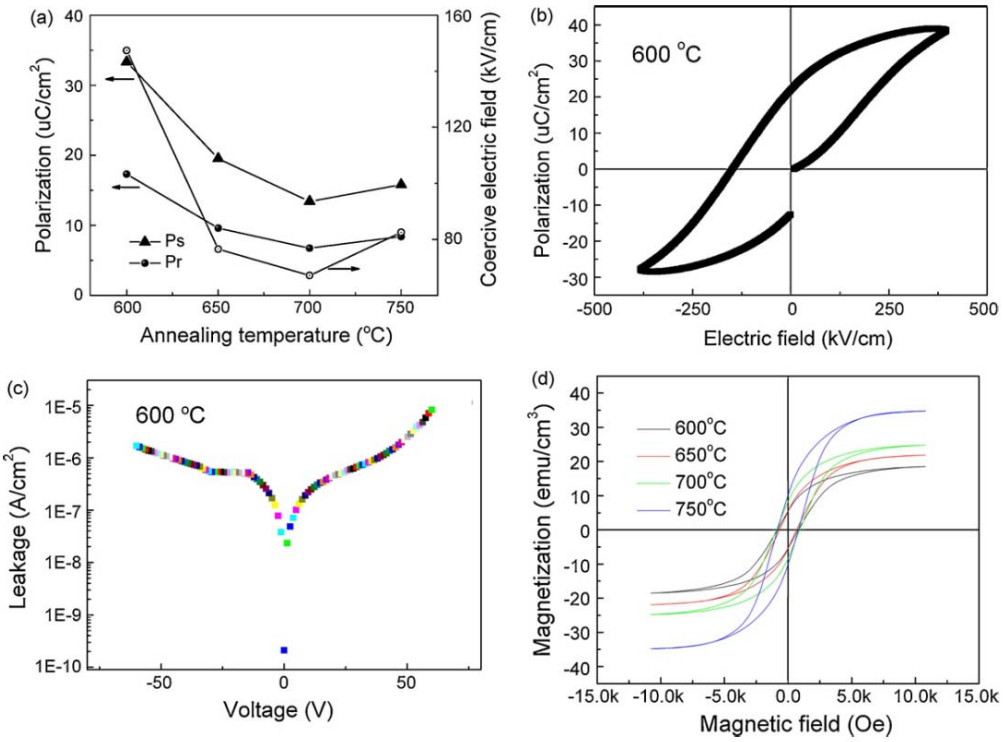

Figure 6-9 Ferroelectric parameters of the composite thick film: (a) Measured at room temperature and 100 Hz vs annealing temperature; (b) Typical ferroelectric hysteresis loop of the thick film annealed at 600°C; (c) Its leakage current density under external DC voltage, and (d) ferromagnetic hysteresis loops of multiferroic thick films annealed at different temperatures.

Figure 6-9(c) shows the leakage current density of the sample annealed at 600°C under external DC voltage. The average leakage current density was about 2×10^{-6} A/cm^2, even acceptable for MEMS design, thus excluding the possibility of the spurious hysteresis loop for the current thick films. Figure 6-9(d) shows the magnetic hysteresis loops of our multiferroic composite thick film at different annealing temperatures. With increasing annealing temperature,

saturated magnetization and remanent magnetization are enhanced from 18.5 emu/cm^3 and 5.5 emu/cm^3 at 600^{o}C to 34.8 emu/cm^3 and 10.2 emu/cm^3 at 750^{o}C, respectively (the volume considered in the calculation of these values was the total volume of the measured composite thick film). This is probably due to the fact that the increase of annealing temperature improved their grain volume and hence improved their magnetic behavior.

6.1.4 Brief summary

CFO-PZT multiferroic composite thick films were fabricated using hybrid sol-gel and nanoparticle processing, and the detailed process procedure and conditions were studied and presented. XRD results suggested the concurrence of only PZT and CFO phases without any other detectable impurities in the resultant multiferroic thick films. SEM cross-sectional micrographs of those thick films showed a nanoparticles-based internal microstructure dependent on the annealing temperatures in the bulk of films. The thick films exhibited simultaneous ferroelectric and ferromagnetic behaviors at room temperature, with the film annealed at 600^{o}C having the best multiferroic properties under experimental conditions.

6.2 Ferromagnetic, ferroelectric and dielectric properties of $CoFe_2O_4$-$Pb(Zr_{0.53}Ti_{0.47})O_3$ multiferroic composite thick films

In chapter 6.1, multiferroic CFO-PZT thick films have been prepared onto Pt/Ti/SiO_2/Si substrate and their structure and properties have been presented. However, the large porosity induced in our thick films annealed above 600^{o}C

due to the different thermal expansion coefficients between the CFO and PZT phases, degraded the multiferroic properties of these films. In this section, a CFO-PZT slurry layer was deposited in the central part of a PZT matrix. With the protection of PZT slurry layer on its two sides, microstructure and properties were expected to be improved. The specific coating sequence is shown in Figure 6-10, in which the heterogeneous CFO-PZT layer is placed at the center of the thick film to avoid its possible contact with the substrate that might induce a large leakage. The resultant films were then annealed at 650^{o}C for 1 hour in the air atmosphere. The thickness of the film measured using a surface profiler was about 3.55 μm.

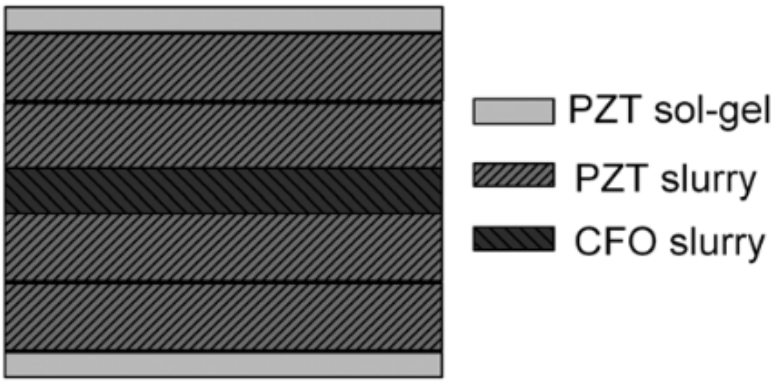

Figure 6-10 Diagram of designed layered CFO-PZT multiferroic thick films.

6.2.1 PHASE STRUCTURE AND MICROSTRUCTURE

Figure 6-11 shows the XRD patterns of the CFO-PZT multiferroic thick film. Both the PZT and CFO phases were observed. SEM cross-sectional micrographs of our multiferroic composite thick film and a PZT thick film prepared from the same processing are presented in Figure 6-12. Compared to the PZT thick films in Figure 6-12(b), some big grains with size between 150 and 400 nm which were not found in (b) can be seen in Figure 6-12(a) [marked

ones], CFO nanoparticles might play a role in this phenomenon. In addition, it should be highlighted that the CFO slurry-based film shown in Figure 6-10 was formed by dispersing CFO particles in PZT sol-gel solution, which caused the CFO nanoparticles to be then scattered in the PZT matrix. Therefore, there was no obvious boundary like that depicted in Figure 6-10.

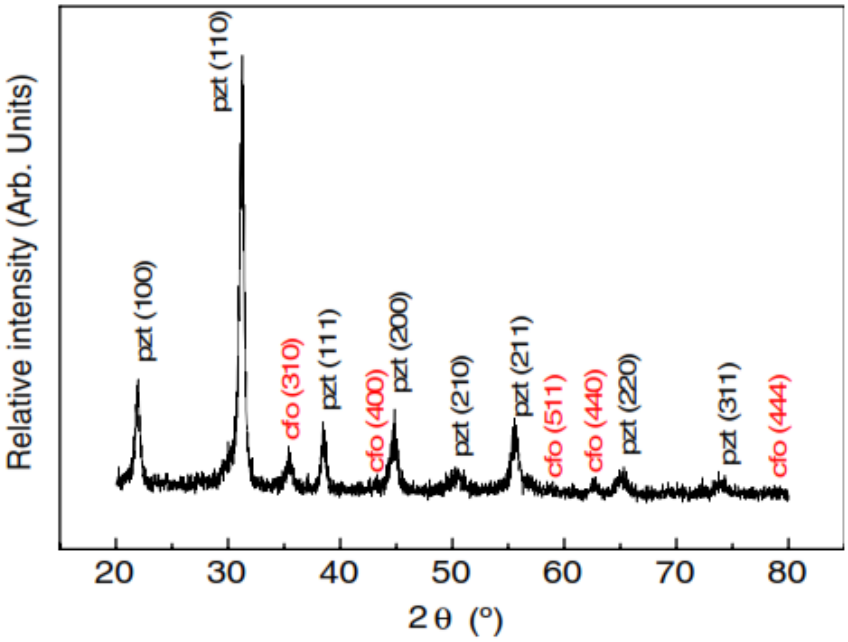

Figure 6-11 Typical XRD result of a CFO-PZT multiferroic thick film.

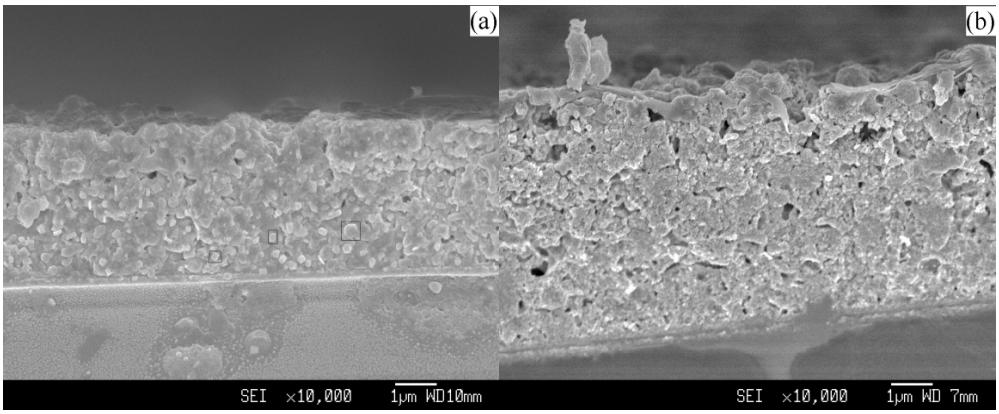

Figure 6-12 SEM pictures of cross-sections of CFO-PZT multiferroic thick film in (a) and PZT thick film in (b).

6.2.2 FERROMAGNETIC MECHANISM

Magnetic hysteresis loops of the multiferroic thick films are shown in Figure 6-13.

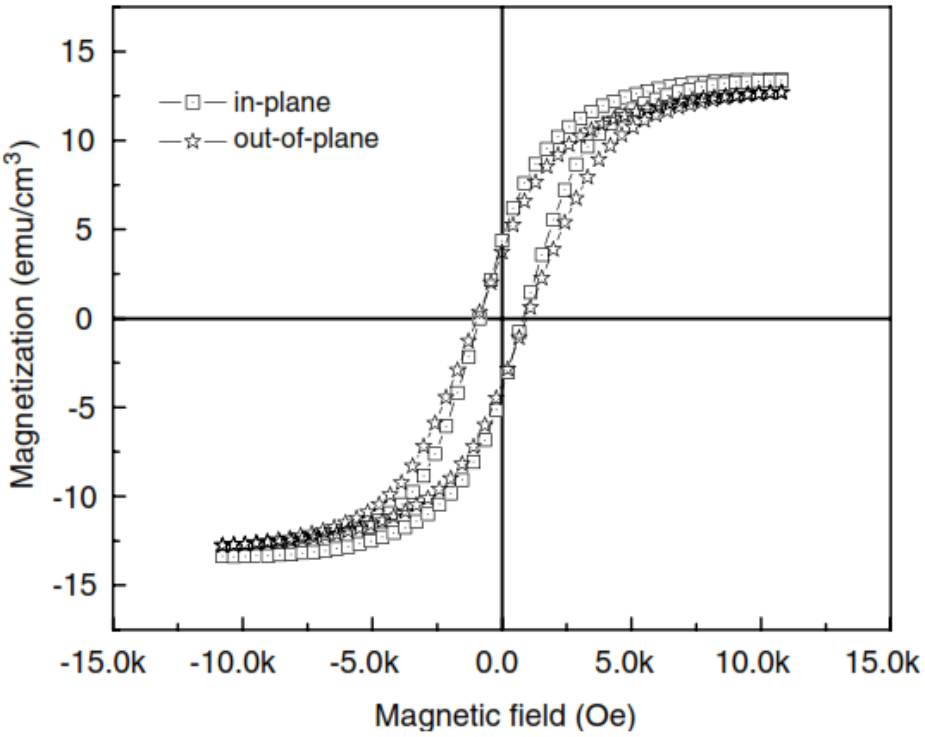

Figure 6-13 Magnetic hysteresis loops of CFO-PZT multiferroic thick films along in-plane and out-of-plane directions.

The CFO-PZT thick film reached a magnetized saturation in both in-plane and out-of-plane directions. The *Hc* of 831.4 Oe along the in-plane direction was smaller than that of out-of-plane direction (941.5 Oe). The possible reason is that it was easier to magnetize the film along the in-plane direction than along the out-of-plane direction due to the demagnetization effect. The remanent magnetization (*Mr*) and saturated magnetization (*Ms*) were 4.3 emu/cm^3 and 13.4 emu/cm^3 along the in-plane direction; while in the out-of-plane direction, they were 3.7 emu/cm^3 and 12.7 emu/cm^3, respectively. The

similar magnetization values with little different coercive fields in the two orthogonal directions indicate that the CFO nanoparticles in the PZT matrix have isotropic magnetic properties. Normally, strain or stress induced by lattice mismatch between substrate and film gives the main contributor to magnetic anisotropy in thin film [174, 175]. However, in the present CFO-PZT composite thick film, the CFO magnetic nanoparticles were distributed far away from the substrate, so the aforementioned effect is negligible. The isolated CFO nanograin islands with a 0-3 connection in the PZT matrix, such as the situation described in literature [107], could be the distributed form in this study. In order to obtain the mass fraction of CFO in the PZT matrix for a comparison, the effective *Ms* (defined as *Mse=measured Ms/mass fraction of CFO in composite thick films*) was calculated. Pure CFO thin films from sol-gel processing yielded a *Ms* of 320 emu/cm^3 [126]. Because the *Ms* is directly related to the percentage of magnetic material in the multiferroic samples, dividing 320 by 13.4 (the *Ms* along in-plane in the present work) results in the ratio of 23.9. It means that the volume fraction of CFO in this film is about 0.04 (1/23.9). According to Wan [81], the *Ms* and the volume fraction of CFO in their CFO-PZT film was 28.4 emu/cm^3 and 0.21, respectively. Therefore, the *Mse* of 13.4/0.04 for our thick films was far larger than that of 28.4/0.21 reported by Wan. According to reference [81], the low *Hc* of 330 Oe should be attributed to the large residual stress in CFO due to the lattice mismatch and thermal expansion coefficient difference between the PZT and CFO phases. Because of the enhanced film thickness and the reduced CFO ratio, the above mentioned reasons are not valid for our average *Hc.* Generally speaking, a high

coercivity can be obtained in a system with nano-structure or preferential orientation, such as thin films with preferred crystalline texturing, or nanoparticles with single domain diameter [155]. Similar shapes of the hysteresis loops measured for different directions of the applied magnetic field confirmed that there was no clear in-plane or out-of-plane magnetic anisotropy in our thick film. This implies that it possesses a random orientation of the CFO crystallites, which agrees well with the XRD result. Furthermore, the single domain diameter of the CFO was of about 40 nm [155], which is much smaller than the average diameter of about 300 nm of the CFO particles in our composite films. Therefore, the observed *Hc* in our composite thick film can mainly be attributed to the magnetic multi-domain configuration of the CFO particles in the composites [155, 156].

6.2.3 FERROELECTRIC MECHANISM

The ferroelectric behavior of the CFO-PZT thick films is shown in Figure 6-14(a), which was measured at room temperature. The asymmetric ferroelectric hysteresis loop was due to different top and bottom electrodes. A remanent polarization of 12.5 $\mu C/cm^2$ and a coercive electric field of 252.8 kV/cm were measured but the sample did not reach the polarization saturation. Figure 6-14(b) shows the ferroelectric hysteresis loops of CFO-PZT thick films for different frequencies. With increasing frequency, the loop becomes thinner due to the effect of capacitance at high frequency, but not because of the increase of leakage current which yields a fat Lissajous-like plot. Therefore, the hysteresis loops are not affected by loss or leakage current, but they are reliable ferroelectric loops. Compared with the CFO-PZT film assisted by PVP [81],

which showed a P_r of 14.6 μC/cm^2 and E_c of 43 kV/cm, the present CFO-PZT multiferroic thick film have smaller remanent polarization and larger coercive electric field.

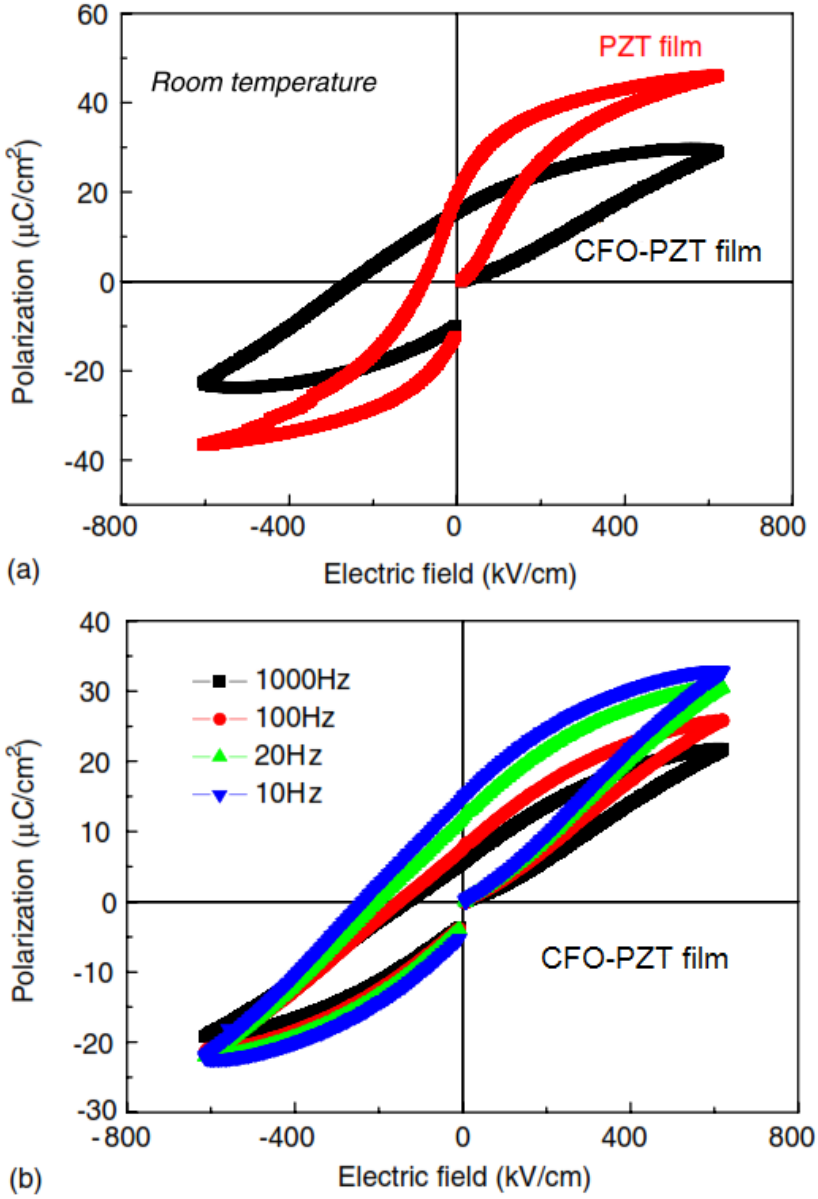

Figure 6-14 (a) Ferroelectric hysteresis loop of CFO-PZT thick film and pure PZT thick film measured at room temperature and 20 Hz, and (b) ferroelectric hysteresis loops of the CFO-PZT film under different frequencies.

On one hand, the addition of PVP is beneficial for avoiding film cracks, promoting film thickness, decreasing residual stress in thin films, and results in a good ferroelectric property [176-178]. It was the lack of PVP that caused the possible cracks in the composite thick film, and the cracks could be one of the reasons leading to the reduced *Pr* and enhanced *Ec*. The further optimization on composition and fabrication procedure is presented in the following section.

On the other hand, the nature of the non-ferroelectric CFO phase was to dilute the ferroelectric remanent polarization, and meanwhile, the hindered and pinned domain wall motion of ferroelectric regions due to the existence of CFO led to the increase of the coercive electric field. This was why the CFO-PZT has a different ferroelectric behavior compared to a PZT thick film as shown in Figure 6-14(a). Furthermore, compared with bi-layer CFO-PZT thin films [53], not only the remanent polarization of our CFO-PZT thick film was smaller, but also the coercive field. This was due to the clamping effect in the thin films from the substrate and the top CFO layer during the switching of ferroelectric domains. It could also be seen that the switching of ferroelectric domains and domain walls motion were more difficult in thin film than those in the composite thick films.

6.2.4 Brief summary

So far, a typical CFO-PZT thick film had been obtained by a hybrid sol-gel processing. Phase structure, microstructure, ferromagnetic and ferroelectric properties were characterized. XRD results indicated that PZT and CFO phases coexisted without any chemical reaction, and the SEM cross-sectional micro-photos of thick films exhibited a dense nanocomposite structure with less pores.

Both ferromagnetic and ferroelectric behaviors were observed and the related experimentally results were explained. In order to ensure more stable multiferroic properties for a possible ME coupling effect, structural optimization, and improving ferroelectric and ferromagnetic properties will be the next primary objectives, and their realization is presented in the following section 6.3.

6.3 Structural optimization of $CoFe_2O_4$-$Pb(Zr_{0.53}Ti_{0.47})O_3$ composite thick films by addition of polyvinylpyrrolidone (PVP)

It is known that a ME coupling effect in multiferroic materials needs at least three necessary factors: dense microstructure, large ferroelectric and ferromagnetic properties [12, 57]. Although multiferroic behavior had been observed in CFO-PZT composite thick films, the cracks that frequently appear in thick films need to be eliminated for reliable ferroelectric properties. Moreover, with the optimization of the film's microstructure, the magnetic phase content is also expected to be increased in order to enhance the ferromagnetic property. In this section, CFO-PZT multiferroic composite thick films with different CFO mass fractions were prepared onto $Pt/Ti/SiO_2/Si$ substrate by a hybrid sol-gel process and spin coating technique. Polyvinylpyrrolidone (PVP) was added into the sol-gel solution as an assist to enhance the film thickness, suppress cracks formation, and decrease the tensile stress during heat-treating procedure. Figure 6-15 shows the chemical structure

of PVP and its key properties. The present section is trying to exhibit the improvement of PVP on the microstructure of CFO-PZT thick films.

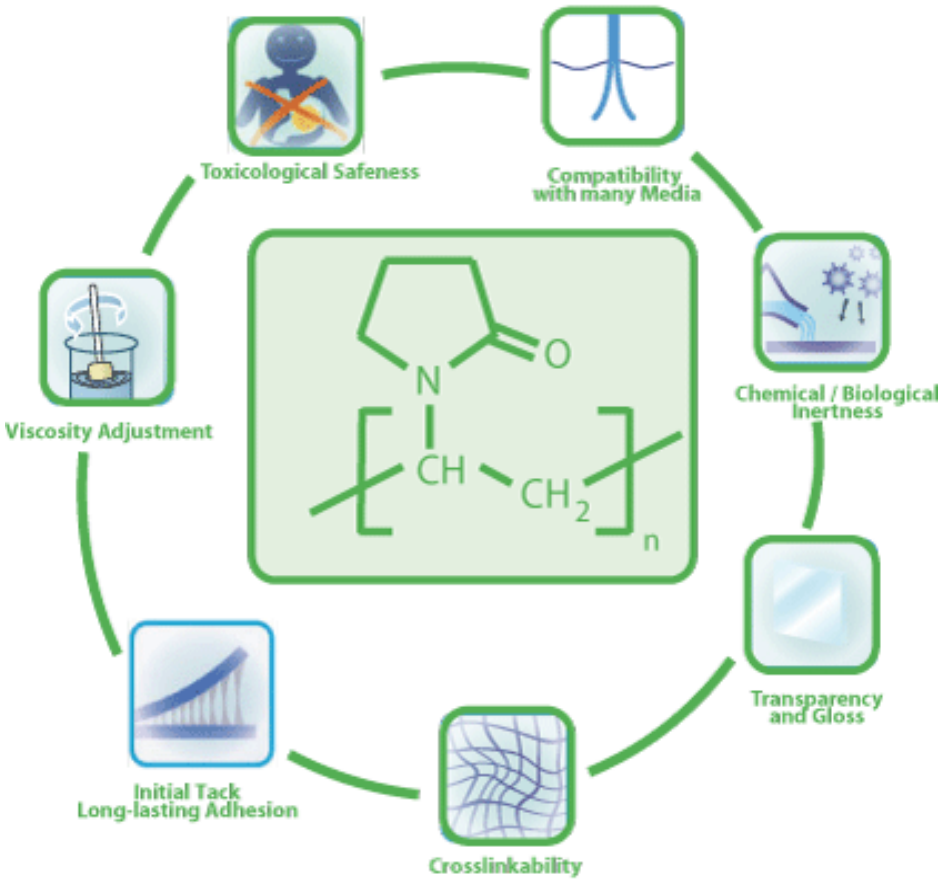

Figure 6-15 Chemical structure of PVP and its properties [179].

6.3.1 Deposition procedure

Tetraisopropyl titanate ($[(CH_3)_2CHO]_4Ti$), acetylacetone ($CH_3COCH_2COCH_3$), lead acetate ($(CH_3COO)_2Pb{\cdot}3H_2O$), zirconium acetylacetonate ($[CH_3COCH{=}C(O\text{-})CH_3]_4Zr$), polyvinylpyrrolidone, and 2-methoxyethanol ($CH_3OC_2H_4OH$) were used to prepare PZT sol-gel solution [56]. Modified CFO and PZT nanoparticles were prepared as mentioned before. Subsequently, CFO nanoparticles were dispersed into the collected PZT sol-gel solution with various mass ratios, ranging from 1/25 to 1/5, to form different

CFO-PZT composite slurries. In addition, PZT nanoparticles were also dispersed into PZT sol-gel solution as a mass ratio of 2: 3 to get the PZT slurry. Both kinds of slurries and PZT sol were deposited on the $Pt/Ti/SiO_2/Si$ substrate by spin coating to achieve the structure shown previously in Figure 6-10. PZT sol-gel solution was used as a buffer layer close to the substrate and also for a cap layer ending the coating process. The CFO-PZT slurry layer was deposited in the central part to avoid a possible surface leakage caused by the low resistivity of the CFO nanoparticles [147]. The coating speed and time was 3000 rpm and 30 s, respectively. The resultant films were then annealed at 650^oC for 1 hour in the air atmosphere. According to the different CFO content in PZT matrix, the films were marked as pure PZT, 1/25, 1/20, 1/15, 1/10, and 1/5, the values of the numerator and denominator indicating the mass ratio between CFO nanoparticles and PZT sol-gel solution in the middle layer of Figure 6-10. Furthermore, the thicknesses were measured via a surface profiler as 7.2 μm, 6.9 μm, 6.8 μm, 6.8 μm, 6.6 μm, and 6.2 μm.

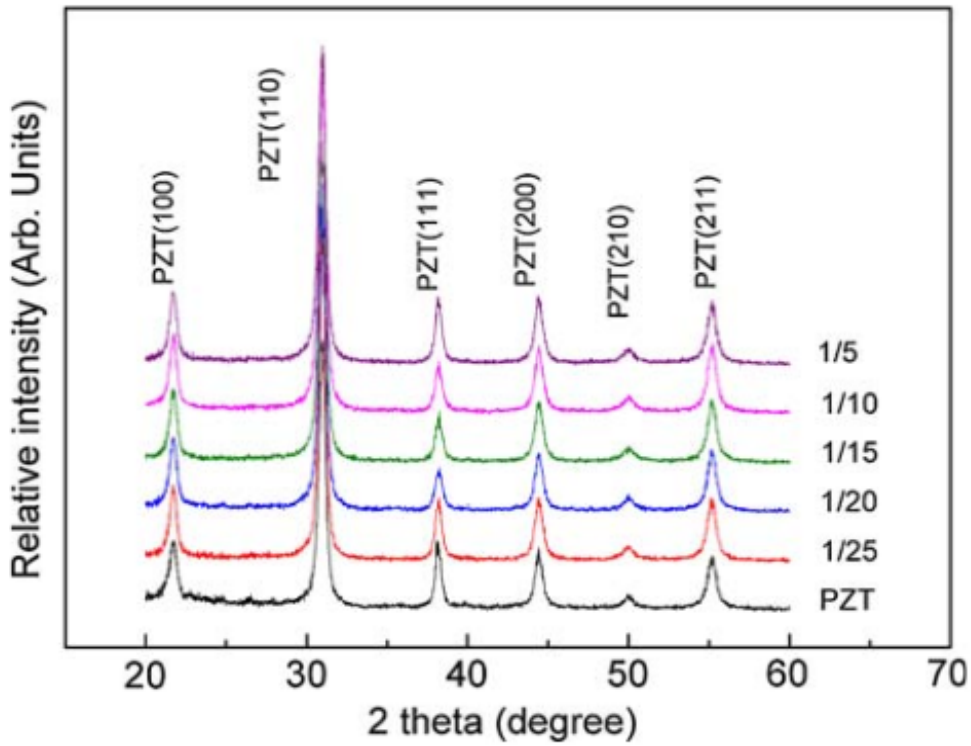

Figure 6-16 XRD patterns of CFO-PZT composite thick films.

6.3.2 Structural characterization

X-ray diffraction results can be seen in Figure 6-16. PZT perovskite phase was obviously observed, but there was no CFO spinel phase (magnetic behavior discussed below demonstrates the existence of CFO phase), indicating a deeply buried distribution of CFO in the PZT matrix. This was demonstrated in the following SEM results.

The typical cross-sectional pictures and topographies of multiferroic films are shown in Figure 6-17.

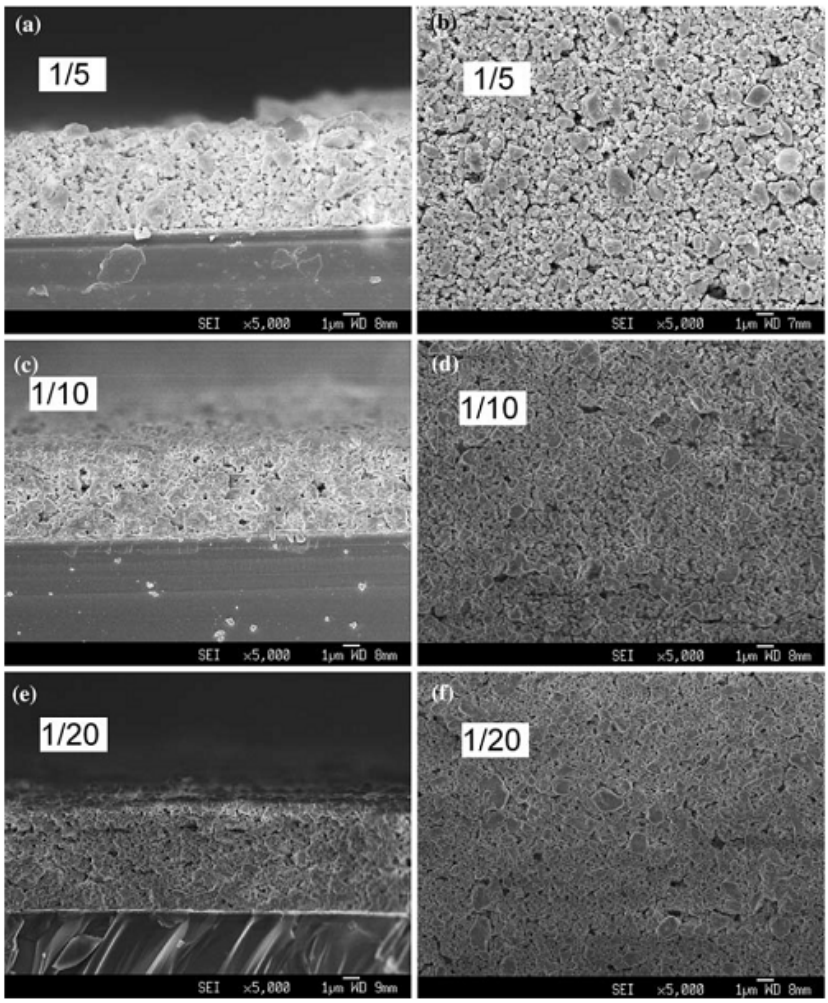

Figure 6-17 SEM morphologies and cross-sectional micrographs of typical CFO-PZT composite thick films.

Because the CFO content in the composites was not large and the top layer in the stacks was always made of PZT slurry and its sol-gel solution, it was reasonable to observe that all the films showed a similar surface morphology. Furthermore, the crack-free surface was attributed to the effect of PVP on the composite thick films due to its increasing structural relaxation of thick films through the retardation of the condensation reaction. Usually, the CFO-PZT composite film thickness exhibited a slightly decrease with increasing the mass fraction of CFO for multiferroic composites, indicating the effect of the CFO

composition on the multiferroic film thickness. However, the CFO-PZT thick film with PVP showed an increasing thickness nearly by 100%, which could be seen from the comparison between SEM result in Figure 6-12(a) and the present SEM cross-sectional result. This was also why X-ray does not detect the CFO phase in a deeper location of thick films.

6.3.3 Influence of magnetic phase content on ferromagnetic behavior

Magnetic hysteresis loops were measured along in-plane direction at room temperature. Up to a maximum external magnetic field of 11 kOe, the results are shown in Figure 6-18(a). It is clearly that *Ms* was proportional with the magnetic content. It is well known that the magnetic behavior in the multiferroic thick films is totally coming from the contribution of CFO nanoparticles. When the content of CFO nanoparticles was increased from 1/25 to 1/5, the *Ms* increased monotonously. According to the estimation method in Chapter 6.2, the present mass fraction of CFO in PZT matrix could be roughly estimated as 4.58%, 3.23%, 1.8%, 0.49%, and 0.36% for the thick films from 1/5 to 1/25. In addition, *Mr* also showed an increase trend with increasing the CFO ratio. However, this increase exhibited by *Mr* was more moderate and in general small *Mr* values were observed in the composite thick films, as it can be seen in Figure 6-18(b).

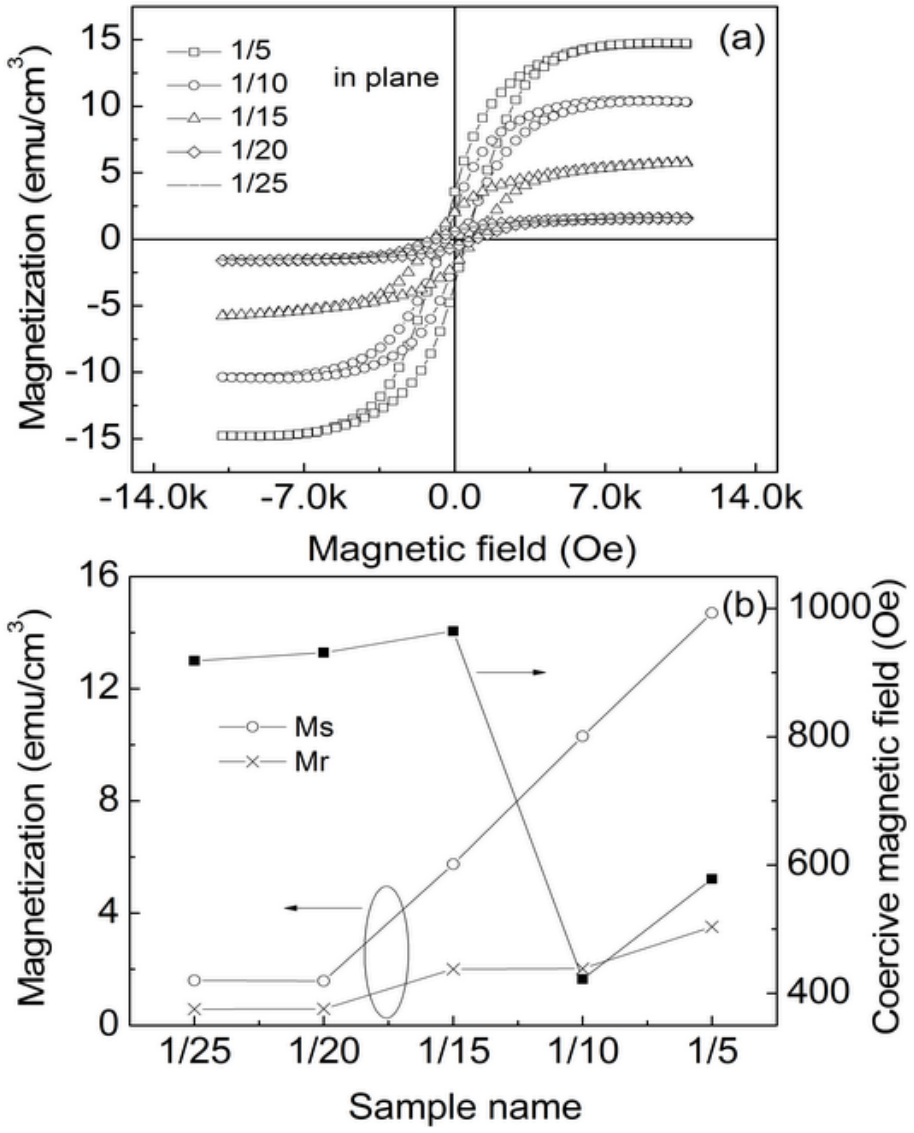

Figure 6-18 (a) Room temperature magnetic hysteresis loops of CFO-PZT composite thick films, and (b) the dependence of their magnetic parameters on the CFO ratio in the film.

In addition, the *Hc* values for CFO contents below 1.8% are very closing to each other, which might be attributed to their extremely low mass fractions in the PZT matrix. The *Hc* values for films with low CFO content would be more easily affected by the sample holder or measurement environments, possibly causing increased errors in determining real *Hc* values. That was also why these *Hc* values were even larger than those for the films with CFO

contents of 1/10 and 1/5. It is known that the *Hc* value reflects the effect induced by the magnetic domain walls and domain rotation. The presence of more magnetic domains in the composites determines a larger *Hc* value due to that more energy is needed to activate them to move. It was also why the *Hc* value for the film with a CFO content of 1/5 was larger than that for the film with a content of 1/10 due to its large CFO content.

6.3.4 Influence of magnetic phase content on ferroelectric behavior

Figure 6-19 shows the ferroelectric *P-E* curves of multiferroic thick films and pure PZT thick film at room temperature and at a frequency of 100 Hz.

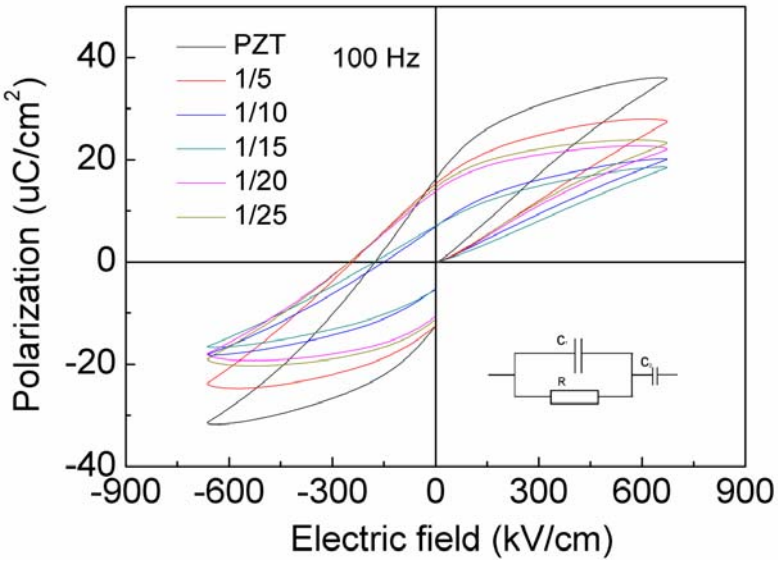

Figure 6-19 Room temperature ferroelectric hysteresis loops of CFO-PZT at 100 Hz, equivalent circuit is shown in inset.

All the thick films showed a normal hysteresis behavior. Their *Ps* and *Pr* values decreased with increasing the CFO content to 1.8%, and then increased as the CFO content further increased to 4.58%. The initial decrease of *Ps* and

Pr is attributed to the dilution of CFO in PZT in our composite thick films, as reported in CFO-PZT thin films [107]. On the other hand, it is known that CFO ferrite particles have low resistivity [147], hence a large concentration of CFO particles leads to a large conductivity of the final multiferroic thick films. This can be represented by an equivalent circuit in which a capacitance (PZT) is connected in parallel with an electric resistance (CFO), and both are connected in series with another capacitance, as seen in the inset of Figure 6-19. When an A.C. voltage was applied, not only the switched charge caused polarization in the capacitance part, but the charges passing through the electric conductivity also partially contributed to the overall polarization as a leaky one. As shown in Figure 6-19, with the further increase of CFO content, saturated and remanent polarization values showed some larger values.

6.3.5 LEAKAGE CURRENT

In order to demonstrate it, leakage current density of CFO-PZT composite thick films is shown in Figure 6-20. Compared with pure PZT thick films, the leakage current density in multiferroic thick films became large gradually with increasing CFO content and they also ascended rapidly with increasing the electric field strength. This behavior is due to the leakage-capacitance structure mentioned above. However, the average leakage values were below 10^{-5} A/cm^2 for the applied electric field below 500 kV/cm. Normally, the larger leakage currents in CFO-PZT thick films mainly results from several aspects: mixed valence for the magnetic ions (e.g. Fe^{2+} and Fe^{3+}), the effect of oxygen vacancies, or both. This explains the observed proportionality of the measured leakage with the CFO content in multiferroic films. Another reason for the

observed leakage behavior is the relatively large porosity in the thick films, which was also the main source for leakage in PZT thick films compared with the much denser PZT single crystal [180]. Large leakage currents usually led to a pseudo-hysteresis loop, such as the one observed in $BiFeO_3$ [181], and even the low electric field endurance [182]. Hence, minimizing the leakage ensures that what is measured is truly the real ferroelectric hysteresis loop rather than the losses in the films.

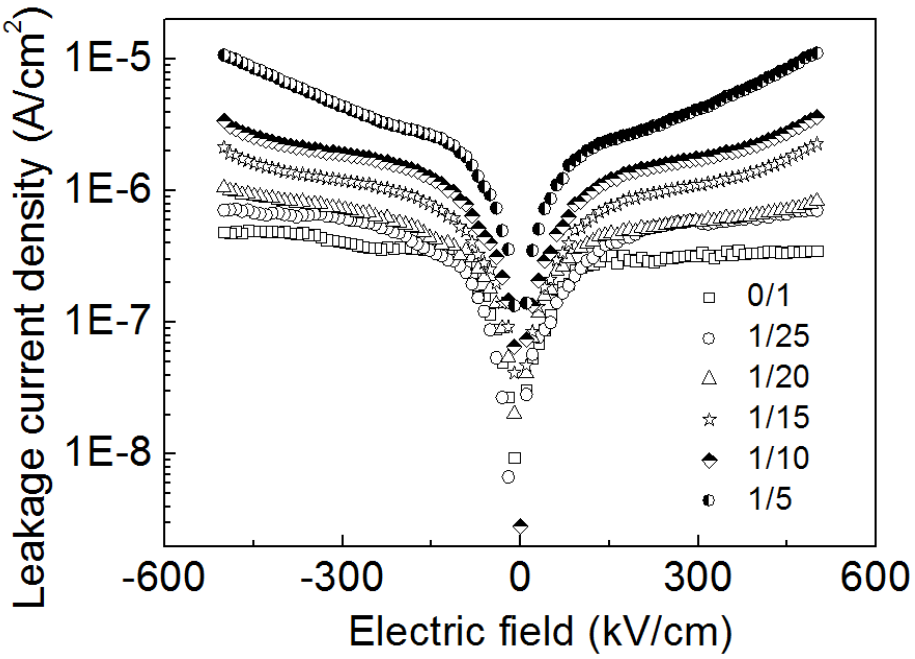

Figure 6-20 Leakage current densities of CFO-PZT composite thick films assisted by PVP at room temperature.

6.3.6 MAGNETOELECTRIC COUPLING EFFECT

From the results above, we can see that both ferromagnetic and ferroelectric properties have been observed simultaneously in all the multiferroic thick films. The influence of the CFO content on ferromagnetic and ferroelectric properties could be separated into two parts: for CFO contents

below 1.8% of CFO content, small *Ms* and *Mr* values were measured, while at the same time less leaky ferroelectric behavior was observed with decreased polarization should be attributed to the dilution of CFO content. However, when the CFO content was reaching 3.23% or more, the *Ms* and *Mr* were significantly larger. Meanwhile, a large CFO content also enhanced the leaky contribution to the ferroelectric behavior, causing larger *Ps* and *Pr* values. Gradually increasing leakage current densities demonstrated this point. Finally, for a critical CFO content of 1.8% in the composite thick film where the ferroelectric behavior was minimally affected by leakage, so that together with its ferromagnetic behavior and dense microstructure, a magnetoelectric coupling effect would be predicted. In order to demonstrate this point, the ME coupling effect of a typical CFO-PZT (sample 1/5) composite thick film was characterized. The dynamic and static ME effects were strongly dependent on their applied DC/AC magnetic field but their values were very low.

The DC ME response is shown in Figure 6-21(a) in a whole cyclic magnetic field. Apparent hysteresis behavior was observed. Furthermore, from initial zero point to the maximum positive magnetic field, the ME coefficient ($\alpha_E=\Delta V/H_{ac}$) exhibited a maximum at 4 kOe and then declined with further increasing magnetic field, which was similar with the trend in other reported multiferroic systems, such as CFO/PZT film/bulk ceramics, and even $BaTiO_3$-$BaFe_{12}O_{19}$ system [55, 81].

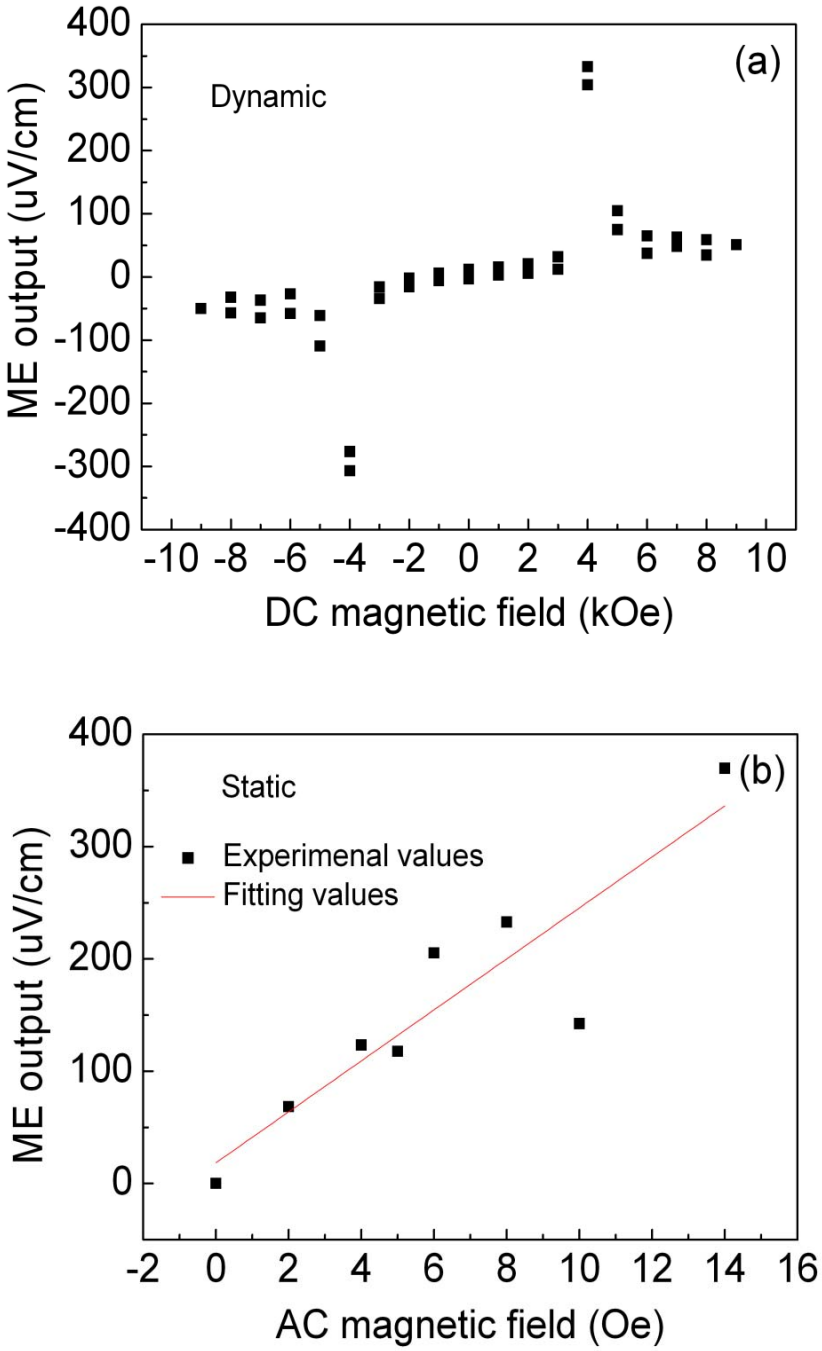

Figure 6-21 Dynamic and static ME coupling effect of CFO-PZT thick film with CFO content.

Normally, the ME effect depends on the applied frequency and ferrite content [64]: the larger the frequency or ferrite content, the stronger the ME effect. This was also why a CFO/PZT thin film with a CFO volume fraction of

25% had a large ME coefficient at 10 kHz [55]. In addition, the static ME output also showed a similarly linear proportionality with the strength of the applied A.C. magnetic field. The experimental and fitted values for the ME output are shown in Figure 6-21(b). These results show that as expected, a large A.C. magnetic field would produce a large strain, which is then passed to the PZT ferroelectric part across the CFO-PZT interface to induce a polarization. The deviation of experimental values from the fitted one might be attributed to the noisy effect from measurement system.

6.3.7 BRIEF SUMMARY

Crack-free CFO-PZT multiferroic composite thick films (above 5 μm) with CFO content ranging from 0.36% to 4.58% were deposited onto Pt/Ti/SiO_2/Si substrate by a hybrid sol-gel processing assisted by PVP. It was found that PVP is beneficial for a smooth surface as well as promoting the film thickness. Among all the samples, single PZT perovskite phase was observed from X-ray diffraction, and the lack of a spinel CFO phase was attributed to being deeply buried in the central part of the PZT matrix. Ferromagnetic and ferroelectric properties were obtained simultaneously at room temperature and both strongly dependent on the CFO content. A ME coupling effect in this thick film was predicted and demonstrated for a CFO content of 1.8%. However, the values observed were too low for the current CFO-PZT thick film to make it a good candidate for device applications. It is known that a large ferroelectric and ferromagnetic behavior as well as a well-controlled microstructure can predict a good ME effect [57]; however, without a good densification of the multiferroic film, just like the situation presented in this section, the induced ME coupling

was very weak. On one hand, too many pores were indicative of a loose contact between the ferroelectric and ferromagnetic grains. On the other hand, a too low ferrite content in the ferroelectric matrix also restricts the ME coupling effect due to their limited crossing interface. The following work will show how to improve the densification of multiferroic thick films as well as a good ferroelectric and ferromagnetic behavior.

6.4 Ferroelectric Properties Improvement of $CoFe_2O_4$-$Pb(Zr_{0.53}Ti_{0.47})O_3$ Multiferroic Composite Thick Films by Sol Infiltration

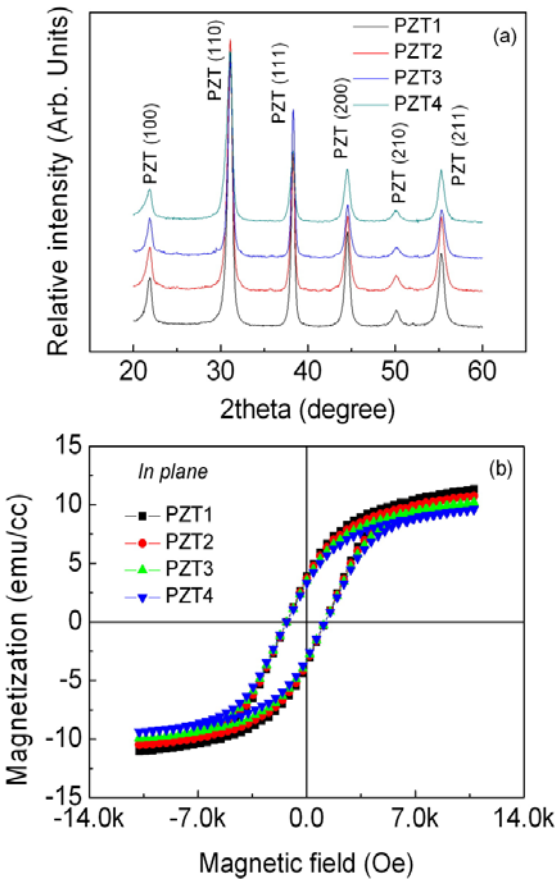

Figure 6-22 XRD patterns of PZT1, PZT2, PZT3 and PZT4 (a) and their magnetic hysteresis loops along in-plane direction at room temperature (b).

In this section, to achieve higher densification of the multiferroic thick films, PZT sol infiltration with 1 to 4 additional layers was introduced after each slurry layer coated. The resultant multiferroic composite thick films were annealed at 650^{o}C for 1 hour in air, and are denoted PZT1, PZT2, PZT3 and PZT4 in correspondence with the number of added to the infiltration layers.

6.4.1 Evidence of CFO phase

Like the films whose deposition was assisted by PVP, XRD patterns of PZT1, PZT2, PZT3 and PZT4 only showed the pure PZT perovskite phase, as it can be seen in Figure 6-22(a). The lack of the CFO spinel phase is attributed to its deeply buried distribution inside the PZT matrix. EDX results demonstrate the connectivity of CFO and PZT.

Table 6-1 EDX results of typical PZT4 on its surface and cross-section.

	Surface		Cross-section	
	Element (%)	Atomic (%)	Element (%)	Atomic (%)
O	16.54	62.20	17.91	70.54
Ti	6.88	9.14	7.26	7.06
Zr	15.73	10.99	14.28	9.22
Pb	60.86	17.67	59.48	12.07
Co	0.00	0.00	0.36	0.36
Fe	0.00	0.00	0.71	0.76
Total	100	100	100	100

Take PZT4 as example, whose EDX quantitative analysis of the existing chemical elements on surface and in cross-section can be seen in Table 6-1. Only four elements -Pb, Zr, Ti, and O- were detected, and their mass ratios

correspond to the chemical composition $Pb(Zr_{0.53}Ti_{0.47})O_3$, indicative of a pure ferroelectric layer on the surface. However, when we focused on its central part of the cross sectional picture, additional Co and Fe elements with an approximate mass ratio of 1: 2 were measured, revealing a chemical composition of $CoFe_2O_4$. The corresponding magnetic measurements of the CFO-PZT multiferroic thick films were performed at room temperature along in-plane direction. The measured magnetic hysteresis loops are shown in Figure 6-22(b) and they further confirmed the existence of the CFO phase in the film. Furthermore, the *Ms* values of these multiferroic thick films decreased slightly with increasing sol infiltration from 1 to 4 layers due to the reduced mass fraction of CFO ferrite particles in the PZT matrix.

6.4.2 Enhancement of ferroelectric properties

Figure 6-23(a) shows the ferroelectric hysteresis loops of multiferroic thick films measured at room temperature and under 100 Hz. All the loops have a slim shape and reach the saturation at a low electric field, indicating a typical soft ferroelectric behavior. With increasing sol infiltration layer from PZT1 to PZT4, the saturated polarization (*Ps*) and remanent polarization (*Pr*) of composite thick films were enhanced from 25.99 $\mu C/cm^2$ and 9.03 $\mu C/cm^2$ to 42.6 $\mu C/cm^2$ and 17.22 $\mu C/cm^2$, respectively, as shown in Figure 6-23(b). Similar improvement through sol infiltration was also reported on PZT thick film by Perez [173]. In addition, the coercive electric field (*Ec*) was reduced from 91 kV/cm to 73 kV/cm with increasing sol infiltration layers due to the depinning effect of defect dipoles in the composite thick films [183], and hence the ferroelectric domain wall motion and domain rotation would be easier.

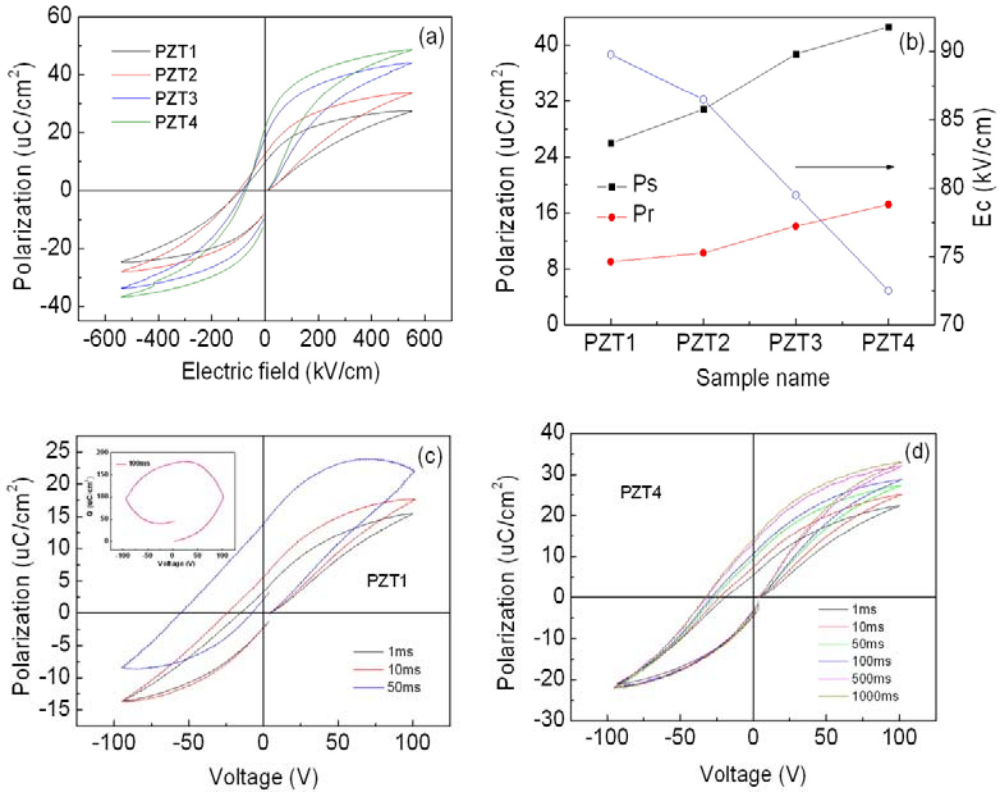

Figure 6-23 Ferroelectric hysteresis loops of PZT1, PZT2, PZT3 and PZT4 at room temperature and 100 Hz (a) and their ferroelectric parameters (b). Duration dependence of P-E curves of typical PZT1 (c) and PZT4 (d) composite thick films under 100 V of external voltage.

Moreover, duration (time of a cycle of applied electric field) dependence of *P-E* curves of typical PZT1 and PZT4 under 100 V of external voltage was investigated to further evaluate the influence of sol infiltration layers on the ferroelectric properties of the films, and the results are shown in Figure 6-23(c) and (d). It can be seen that the polarization and coercive electric field increase with prolonging duration of exposure to the external electric field. This is usually attributed to the space charges in the thick films, which would be pronounced at low frequency. In our case, due to a different polarization mechanism of CFO and PZT, a potential barrier might be formed at their

interface with accumulated interfacial charges. It is known that interfacial charge could enhance or degrade polarization depending on the polarization difference between neighboring layers [183]. When these charges accumulate and stay active for a longer duration, the dipolar effect would give way to them and give rise to a dilated hysteresis loop.

The increased coercive electric field is also related to these charges due to the large leakage current caused by them in composite thick films. Quantitatively, when 50 ms of duration was applied on the PZT1, the hysteresis loop became distorted and as the duration reached 100 ms, the dielectric behavior changed into a leaky one, as it can be seen in the inset of Figure 6-23(c), which exhibits a circular hysteresis loop which is known for always be indicative of leakage currents. However, as it can be seen in Figure 6-23(d), the loops shape of PZT4 are not affected up to duration as high as 1000 ms, indicative of a dipolar polarized predominating state.

The comparison of the hysteresis loops of the PZT1, PZT2, PZT3, and PZT4 films hence revealed that more sol infiltration could reduce the interfacial charges and improve ferroelectric behavior.

6.4.3 Suppressed leakage behavior

It is known that the enhancement of ferroelectric behavior is usually accompanied with suppressed leakage current density [184, 185]. Figure 6-24(a) shows the leakage current density (J) of PZT1, PZT2, PZT3, and PZT4 measured at room temperature. With increasing the number of sol infiltration layers from 1 to 4, the average J value decreased from 4×10^{-5} A/cm^2 to 2×10^{-6} A/cm^2. Besides the contribution of exchange between Fe^{2+} and Fe^{3+} to leakage,

another main contribution to a large leakage was the porous structure of the composite thick films. By introducing enough PZT sol layers in the thick films, the porous structure could be improved along with a reduced leakage current that would be very useful for MEMS device applications [186]. On the other hand, the reduced leakage current could also suppress the contribution of conductive loss to the ferroelectric hysteresis loops that might result in pseudo-ferroelectricity in multiferroic materials [187], and exhibit a true multiferroic behavior as well as the magnetoelectric coupling effect with its ferromagnetic property.

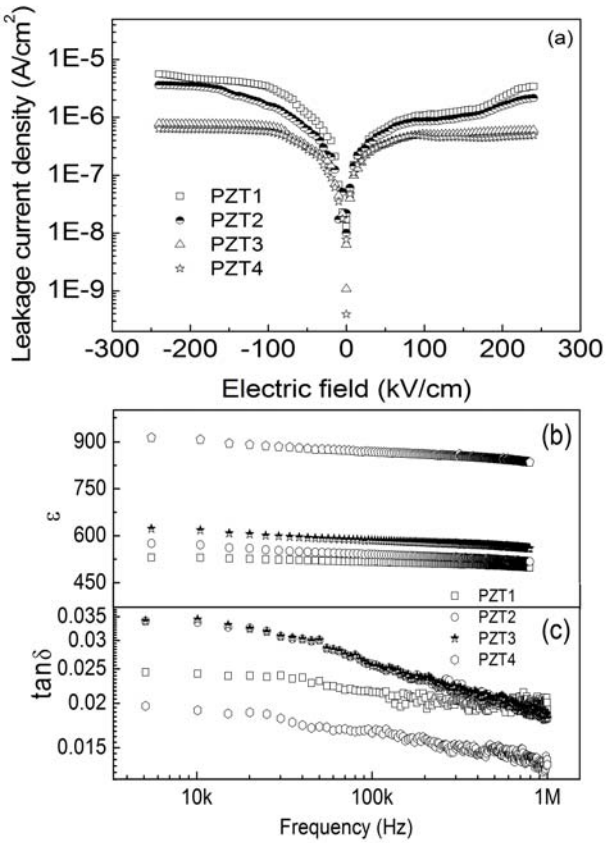

Figure 6-24 Leakage current densities of PZT1, PZT2, PZT3 and PZT4 at room temperature (a), as well as their dielectric constants (b), and losses (c) under different frequencies.

6.4.4 Enhancement of dielectric properties

In addition, the improvement of sol infiltration on dielectric properties of composite thick films was also remarkable. Figures 6-24(b) and (c) shows the frequency dependence of their dielectric constant (ε) and loss tangent ($tan\ \delta$) at room temperature. It can be clearly seen that the dielectric constants are nearly kept stable in the whole frequency range except for some small dielectric dispersion at low frequency similar to that of dielectric loss, in which some D.C. conductivity might be induced by existing mobile charge carriers [188]. The movement of these mobile charges is suppressed at high frequency, and hence the decreased dielectric loss is observed. For quantitatively clarifying the influence of sol infiltration on the dielectric properties of the films, the dielectric constant at 100 kHz was enhanced from 517 to 896 as the number of sol infiltration layers increased from 1 to 4, along with a reduced loss tangent value from 0.025 to 0.017. These results are also in agreement with the enhanced ferroelectric property since the dielectric constant was mainly contributed by ferroelectric polarization.

6.4.5 Thick film quality optimization comparison

Figure 6-25 compares the typical cross-sectional structure of PZT1 and PZT4. It can be seen that PZT1 films exhibits a porous microstructure, whereas the PZT4 films shows a dense structure due to sufficient sol infiltration. There was no remarkable thickness difference between PZT1 and PZT4, suggesting that most of the additional sol might infiltrate through the porous microstructure of these composite thick films. The infiltrated sol would promote densification process of the films and improve the mechanical contact between ferromagnetic

and ferroelectric grains accordingly. It should be noted that the magnetoelectric coupling effect in multiferroic materials is usually caused by the strain-transfer between the ferromagnetic and ferroelectric parts [12], hence the direct contact with one another is inevitable. Therefore, the PZT4 film with enhanced densification was believed to have the ability to induce a ME coupling effect based on the observed ferroelectric and ferromagnetic properties.

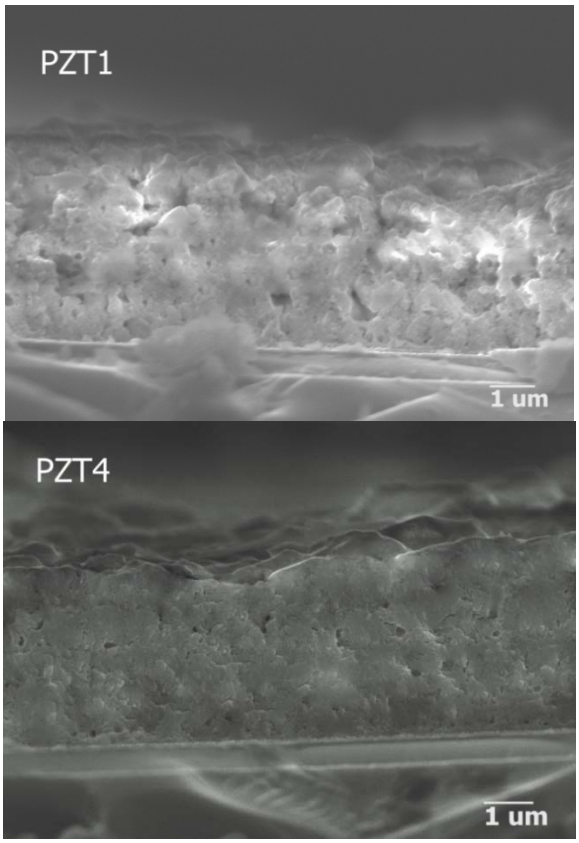

Figure 6-25 Typical cross-sectional pictures of PZT1 and PZT4.

6.4.6 BRIEF SUMMARY

Through introducing sufficient PZT sol infiltration in CFO-PZT multiferroic composite thick films during their sol-gel deposition process, their ferroelectric and dielectric properties were enhanced as well as a longer endurance to the external voltage was also achieved. *Ps* and *Pr* could reach 42.6

$\mu C/cm^2$ and 17.22 $\mu C/cm^2$ with 4 layers of PZT sol layers. The dielectric constant was also increased to 869 at 100 kHz with a reduced tangent loss of 0.017. All these effects were attributed to the optimized film densifications. However, the only shortcoming was that magnetic property decreased with increasing sol infiltration. Hence, the next part will be focused on the enhancement of ferromagnetic properties.

6.5 Ferromagnetic Properties enhancement of $CoFe_2O_4$-$Pb(Zr_{0.53}Ti_{0.47})O_3$ multiferroic composite thick films

Since PVP promoted the film thickness and avoided the cracks, while sol infiltration improved the densification of the thick films as well as their ferroelectric properties, the present section combines both of them together to enhance the ferromagnetic properties by increasing the magnetic content percentage based on a well-controlled microstructure.

6.5.1 Modification of slurry

PZT sol-gel solution was modified by PVP with a proper weight fraction and PZT slurry (Marked as P) kept the same ratio of PZT sol-gel solution and modified PZT particles as before. Modified CFO and PZT nanoparticles were mixed with a mass ratio of 1: 1 and then dissolved into the PZT sol-gel solution with a mass ratio of 2: 3 to form the new CFO slurry (marked as C). Both slurries (P and C) were deposited onto $Pt/Ti/SiO_2/Si$ substrate as PPPP, PPCC, and CCCC, see Figure 6-26. Additionally PCPC, CPCP, and CCPP were also prepared using both slurries. Between every two slurry layers several layers of PZT sol were coated to compensate the porosities of the thick films and

improve their densification. The resultant composite thick films were annealed at 650°C for 1 hour in air, and their thicknesses were subsequently measured with a surface profiler and all were above 5 μm.

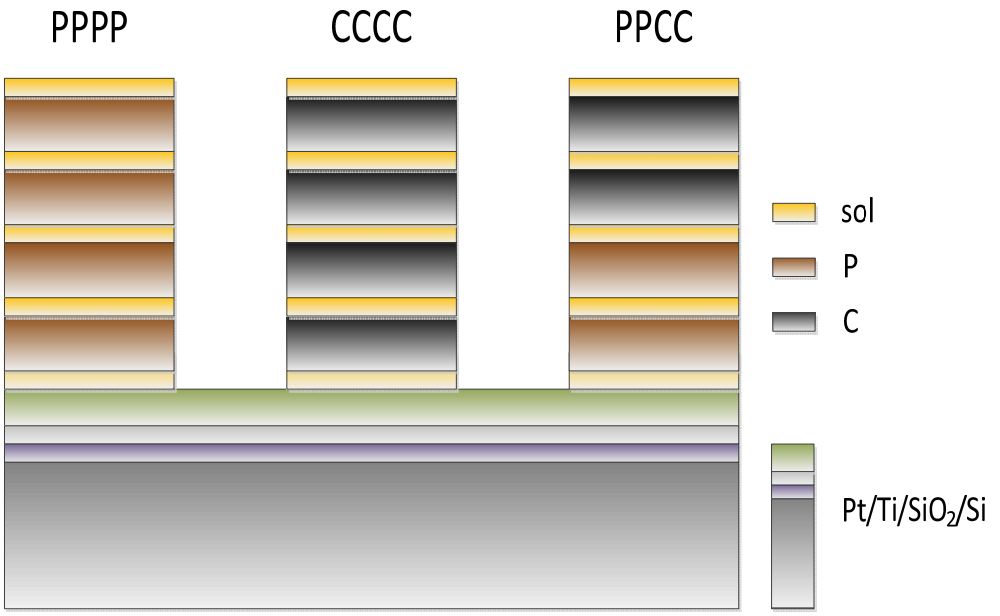

Figure 6-26 Schematic illustration of multiferroic CFO-PZT composite thick films: PZT slurry with additional PVP (P), CFO slurry (C) and standard PZT sol-gel.

6.5.2 Structural characterization

Figure 6-27(a) shows the X-ray diffraction (XRD) of three thick films. The well-defined peaks of the perovskite PZT and spinel CFO phase without any other impurity phase were identified in sample CCCC and PPCC. For the sample PPPP, only the peaks of the typical perovskite phase were observed. However, as can be seen in Figure 6-27(b), even if the CFO phase existed, no spinel peak was observed in CCPP. More specifically, the closer of CFO location to the surface, the stronger its spinel main peak, revealing an important effect of deposit sequence on magnetic phase detection. This phenomenon has also appeared and been discussed in the previous section.

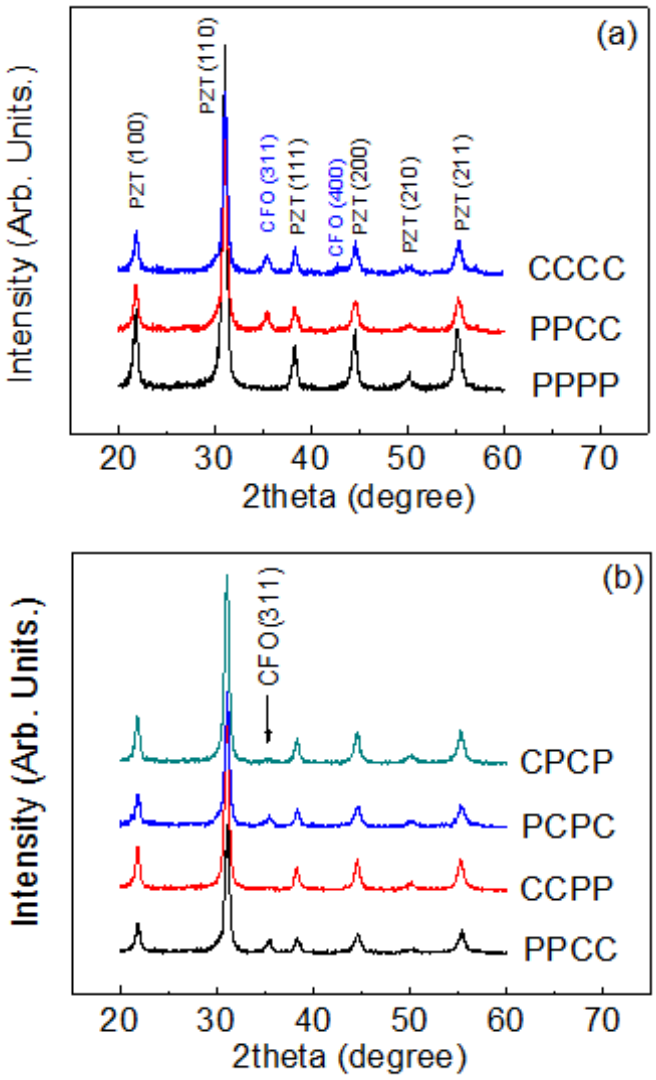

Figure 6-27 Influence of (a) magnetic phase content, and (b) deposit sequence reflected from XRD patterns.

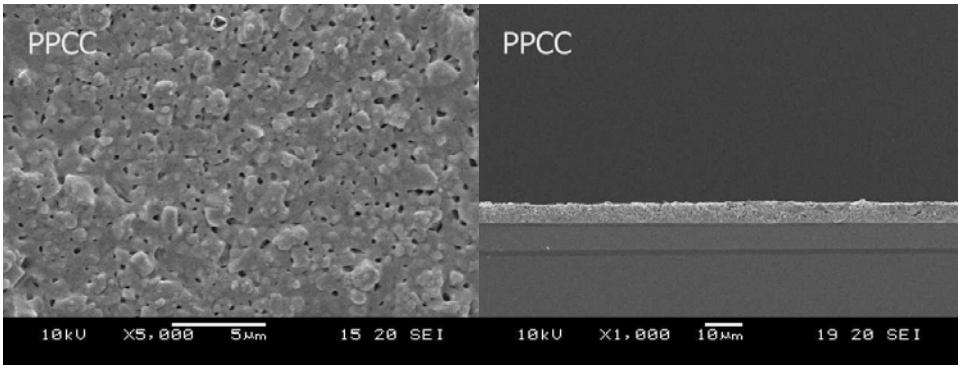

Figure 6-28 A typical and surface morphology and cross-sectional picture of sample PPCC.

Figure 6-28 exhibits a typical cross-sectional image and surface morphologies of the PPCC sample. It can be seen from the cross-sectional picture that the deposited films were uniform and no apparent projectors appeared on its surface, indicating a well composite structure for PZT and CFO. This was attributed to the modified CFO slurry.

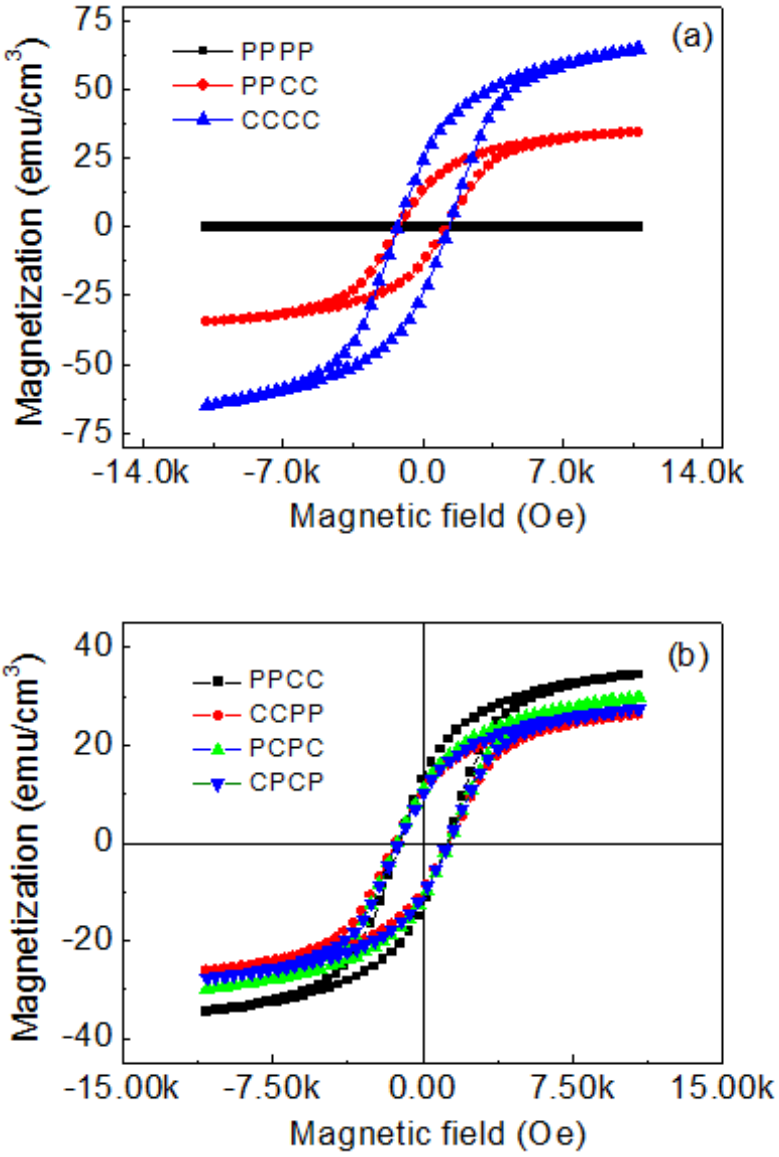

Figure 6-29 In-plane magnetic hysteresis loops of multiferroic CFO-PZT composite thick films measured at room temperature with: (a) different magnetic contents, and (b) different deposit sequences.

6.5.3 ENHANCEMENT OF FERROMAGNETIC PROPERTIES

Figure 6-29(a) shows the in-plane magnetic hysteresis loops of the three composite thick films at room temperature. They demonstrate the effect of the different CFO contents on the coercivity as well as saturation magnetization. Furthermore, the saturation magnetization was dramatically promoted compared with the results in previous sections. As it can be seen in Figure 6-29(a), no magnetic response was observed in sample PPPP. The coercive fields of sample CCCC and CCPP were the same of 1288 Oe, showing that the coercive field exhibits no dependence on the magnetic phase content. This value was close to that of pure CFO thin film [127], also indicative of a less effect from film thickness. However, the *Ms* values of in-plane hysteresis loops were 64.9 emu/cm^3 for the CCCC film and 34.5 emu/cm^3 for the PPCC film. According to the estimation method described in chapter 6.2, the mass fractions of CFO in PZT matrix are approximately estimated as 20 wt% and 8 wt% for the CCCC and PPCC film [129], which were far larger than the maximum magnetic content of the films presented in Chapter 6.3, indicating an enhancement of ferromagnetic properties. The *Hc* and *Ms* values extracted from Figure 6-29(b) for CCPP, CPCP, PCPC, and PPCC films are listed in Table 6-2. Based on the same composition, no change was observed for the *Hc* values of the films with different deposit sequences. However, when the "C" layer was closer to the film surface, its *Ms* value of film became larger, as seen in Table 6-2. This was in agreement with the case of multilayered CZFO-PZT thin films [57], because the closer the CFO layer is to the substrate, the stronger it is

constrained by the substrate and, thus, the lower the overall saturation magnetization of the composite thick film.

Table 6-2 Saturated magnetization, saturated polarization and remanent polarization of PPCC, PCPC, CPCP and CCPP.

	Ms (emu/cm^3)	*Hc* (Oe)	*Ps* (μC/cm^2)	*Pr* (μC/cm^2)
PPCC	34.5	1288	33.3	17.5
PCPC	29.7	1288	32.3	17.9
CPCP	27.5	1288	32.4	18.9
CCPP	26.1	1288	31.8	19.1

6.5.4 THE BALANCED FERROELECTRIC PROPERTIES

Since the ferromagnetic properties have been improved compared with the previous results, the other crucial issue that needs to be clarified is how the ferroelectric behavior was affected. Figure 6-30(a) presents ferroelectric hysteresis loops of the PPPP, PPCC and CCCC samples.

A typical soft ferroelectric hysteresis loop was observed for the PPPP sample. As for the PPCC, it was interesting that its saturated polarization and remanant polarization were larger than that of PPPP as well as having a larger coercive electric field under a similar external electric field. Compared with the typical soft ferroelectric loops previously shown in Chapter 6.4, it is easy to understand that a large leakage behavior from more magnetic content is responsible for this observed behavior [52, 189]. This is confirmed by the subsequent observation: with increasing the CFO content to nearly 20 wt%, a lossy ferroelectric loop was observed for the CCCC film, indicating an abundant magnetic content.

The influence of the deposition sequence on the ferroelectric properties of CFO-PZT thick films can be seen in Figure 6-30(b).

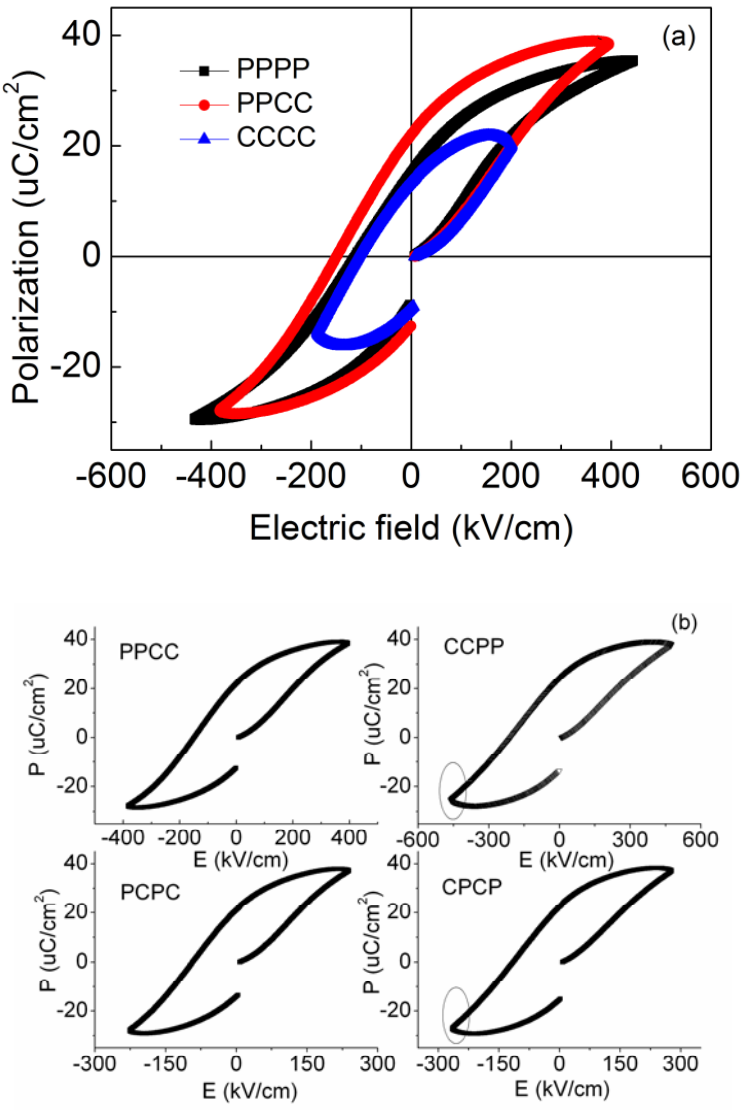

Figure 6-30 Influence of: (a) magnetic phase content, and (b) the deposition sequence on the room temperature ferroelectric hysteresis loops.

Complete hysteresis loops of PPCC, PCPC, CPCP, and CCCC with an approximate CFO content of 8 wt% are presented for detailed comparison. Compared with PPPP, the loops of these four samples had a larger area, and their polarization values extracted from these hysteresis loops had very close

values, as shown in Table 6-2. However, for the CCPP and CPCP films, the polarization values extracted from the hysteresis loops began to decline before reaching the maximum applied electric field, indicative of a typically leaky mechanism. This phenomenon became weak for the PPCC and PCPC films, especially when the bottom layer closest to the substrate had a richer content in ferroelectric phase, as can be seen in the loop of PPCC, where the polarization keeps rising for the maximum electric field. This was in agreement with the effect of the deposition sequence on ferroelectric properties of multilayered CZFO-PZT thin films [57]. According to literatures [187], the wider loop was generally attributed to the effect of space charges and the typical loop in such a case was usually like the one measured in our CCPP and CPCP samples. It is known that introducing low resistivity materials into ferroelectric materials will inevitably bring about space charge carriers, which is undesirable to ferroelectric or dielectric properties. However, by optimizing the deposition sequence, like the situation reported in CZFO-PZT thin film and our CFO-PZT thick film, the effect of space charges could be suppressed, and consequently, enhanced polarization values were achieved, as those measured for our PPCC and PCPC films.

6.5.5 Brief summary

Structural optimization of CFO-PZT composite thick films by introducing sol infiltration and PVP, resulted in the enhancement of the CFO magnetic content up to 20 wt% in the PZT matrix. Consequently, ferromagnetic properties were improved but the ferroelectric properties were severely degraded. However, when the magnetic content was controlled and limited

strictly at 8 wt%, and when a proper deposition sequence was employed to obtain PPCC, PCPC films, balanced ferroelectric and ferromagnetic properties were achieved. A significant ME coupling effect in these composite thick films can hence be predicted.

6.6 Dielectric relaxation and conductivity mechanism of $CoFe_2O_4$-$Pb(Zr_{0.53}Ti_{0.47})O_3$ composite thick films

So far, a promising ferromagnetic and ferroelectric behavior has been achieved in CFO-PZT composite thick films based on their improved densification [148, 151]. In order to develop a deeper understanding of this material system, especially the influence of low resistivity CFO on dielectric properties of multiferroic thick films, a detailed discussion on temperature and frequency dependent impedance spectroscopy results will be presented in this section.

6.6.1 Experimental procedure

The sample studied in this section was deposited as Figure 6-10 and showed a high film quality, as it can be seen in Figure 6-31. Impedance spectroscopy analysis of this film was carried out in the frequency range from 100 Hz to 1 MHz and in the temperature range from 25 to 275^{o}C. The A.C. conductivity of the composite thick films was estimated from the standard relation:

$$\sigma_{AC} = \omega \varepsilon' \varepsilon_0 \tan\delta \qquad (6\text{-}2)$$

where ε_0 and ε' are the permittivity of the free space and real part of measured dielectric permittivity, ω is the angular frequency and $\tan\delta$ is the loss tangent.

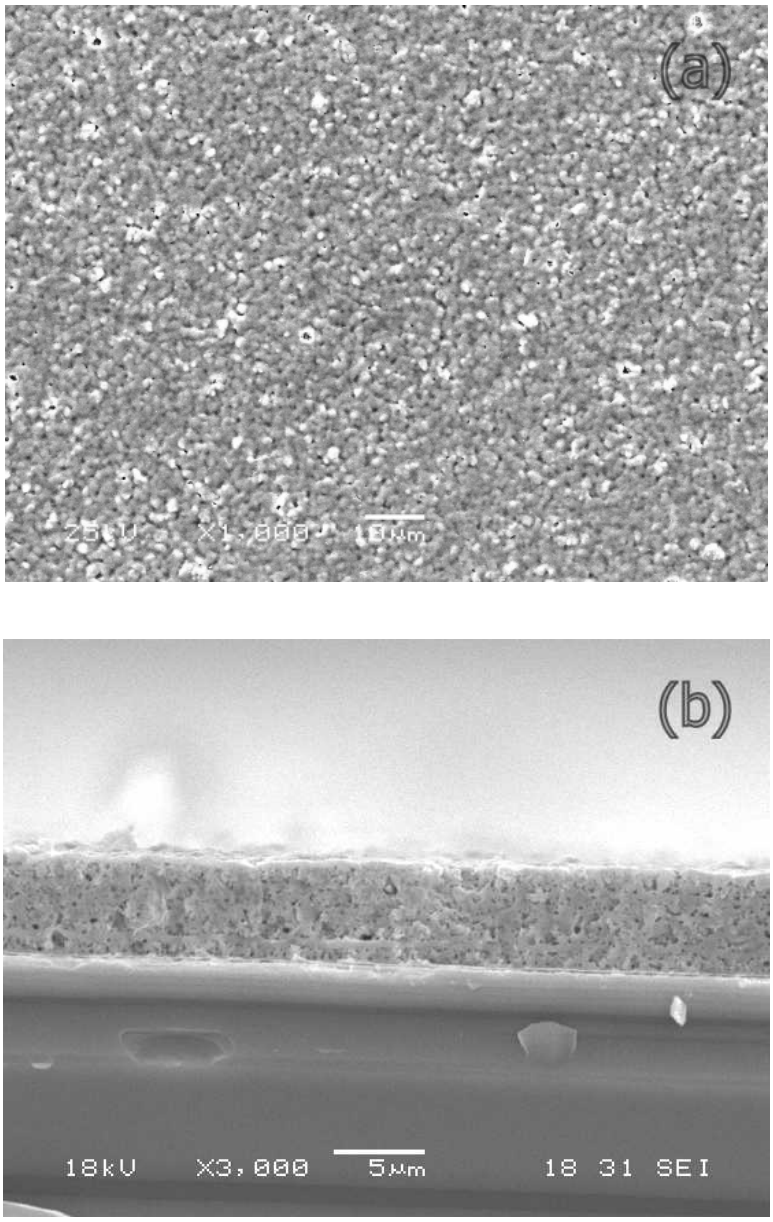

Figure 6-31 Surface morphology (a) and cross-sectional picture (b) of the studied CFO-PZT composite thick film.

6.6.2 IMPEDANCE SPECTRA

Figure 6-32 shows the frequency and temperature dependence of the real and imaginary part of impedance (Z' and Z'', respectively). Figure 6-32(a)

shows that the Z' value decreases with frequency and a weak relaxation peak (marked with arrows) is observed initially at 25^{o}C, which then moves to higher frequencies with increasing temperature and finally disappears beyond 125^{o}C. This corresponds to the faint relaxation behavior of Z'' observed in Figure 6-32(b) (marked with arrows), where the imaginary impedance decreases with frequency in an approximately linear manner below 225^{o}C due to the high sample resistance of composite thick film, which can track to the leakage at zero voltage in Figure 6-24. A typical relaxation peak smoothes into the frequency measurement range once the temperature reaches 275^{o}C, as exhibited in Figure 6-32(b).

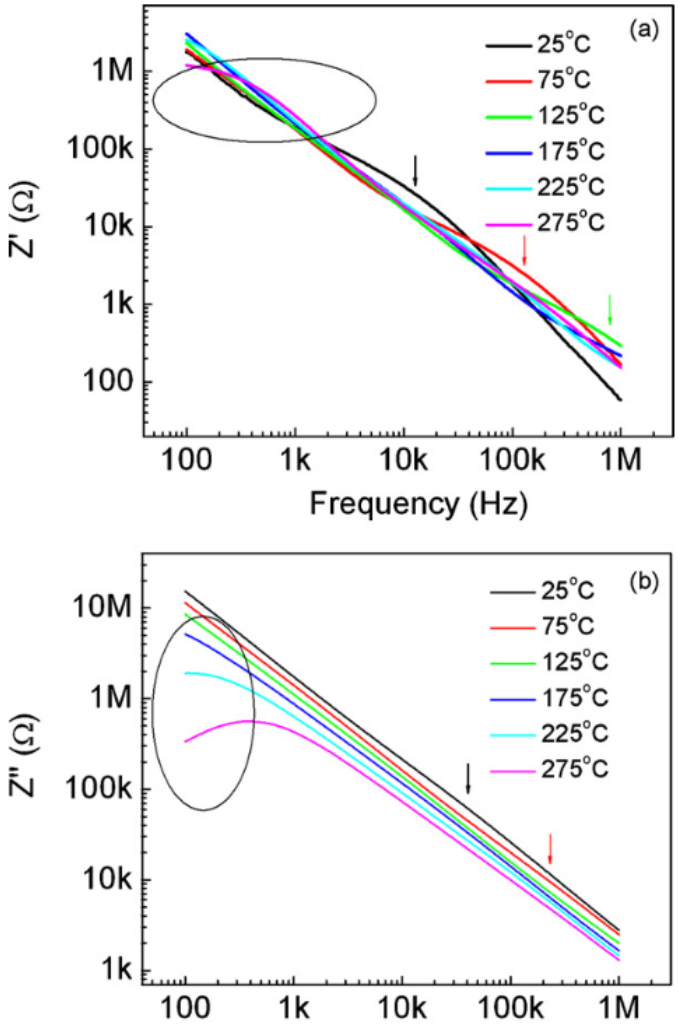

Figure 6-32 Temperature and frequency dependence of: (a) the real and (b) the imaginary part of the impedance of the CFO-PZT composite thick film.

This peak corresponds to another relaxation behavior indicated in Figure 6-32(a) at a similar low frequency range around 500 Hz. According to the Arrhenius law [190],

$$f_r = f'_1 \exp[-\frac{E_r}{k_B T}] \qquad (6\text{-}3)$$

where f'_1 is the relaxation frequency at an infinite temperature and E_r is the activation energy for the dielectric relaxation, the activation energy is estimated

as 0.58 eV. In addition, it was noted that the values were slightly reduced with increasing temperature, indicating a weak D.C. conductivity dependence on temperature. This was similar to the situation of the multilayered CFO-PZT thin film below 500 K [106].

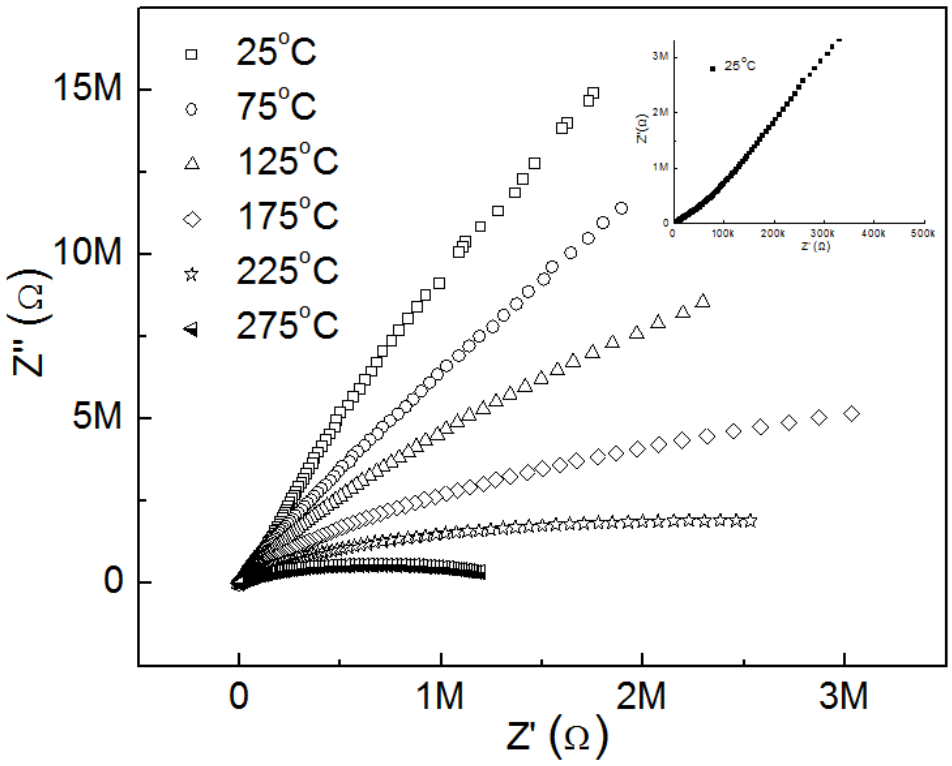

Figure 6-33 Nyquist plots of impedance data of CFO-PZT composite thick film at selected temperatures; inset one is the typical plot at 25°C.

Nyquist (or Cole-Cole) plots of impedance data at different temperatures are shown in Figure 6-33. At room temperature two poorly resolved semicircular arcs were observed: a small arc at high frequency (inset) which was largely obscured by a larger semicircular arc at low frequency. From 25 to 225°C, both semicircular arcs existed; but when the temperature reached 275°C, only a single broad semicircular arc was observed in the low frequency region without any additional contribution detected in the high frequency region. This

was because the time constant at high frequency decreased with temperature, leading to a loss of resolution obscuring the semicircular arc in the impedance plot at high temperature [157]. The size of the semicircular arcs observed in the impedance plots shown in Figure 6-33 were scaled according to the magnitude of their resistance. Each arc comprised of two parts, each corresponding to largely different magnitudes of R (often by orders of magnitude). Therefore, the larger resistive response dominated entirely, making the resolution of the smaller resistive response difficult. In such cases electric modulus data, where semicircular arc scales inversely to capacitance, are often more useful for resolving the different relaxations [191], and they are presented in the next sub-section.

6.6.3 ELECTRICAL MODULUS

The electric modulus was calculated from equation 5-4. The values of M' and M'' are shown in Figure 6-34(a), where the direction of increasing frequency was also indicated. Two very large semicircular arcs were observed separately below 125^{o}C and above 200^{o}C. A small semicircular arc was also observed over the whole temperature range. The low temperature large semicircular arc was induced by the grain effect, while the high temperature arc could be attributed to the grain boundary effect. It was noted that the magnitudes of the grain boundaries capacitance were comparable to the grain capacitance. This was due to the heterogeneous composite structure, which was also demonstrated in thickness dependent CFO-PZT multilayered thin films [106]. Additionally, when the temperature was increased beyond 125^{o}C, the grain effect had moved out of the frequency window; but the grain boundary

effect had not entered into this window until 200^{o}C. In this temperature range of 125-200^{o}C, it can be seen from Figure 6-34(b) that three effects were observed at 150^{o}C. Besides the high frequency degraded grain effect and the low frequency strengthened grain boundary effect, there was another effect in between them, which is not found in CFO-PZT thin films [106].

All these three effects were consistent with an equivalent circuit comprising three parallel *RC* elements, as shown in the inset in Figure 6-34(b). Here, the low frequency arc is modeled by the R_3C_3 response while R_1C_1 response models the high frequency arc. These responses are caused by the high frequency grain effect and the low frequency grain boundary effect, respectively. The R_2C_2 part of the circuit corresponds to the effect observed in the intermediate frequency range at 150^{o}C. Furthermore, this effect is gradually strengthened with increasing temperature, as is evident in Figure 6-34(a). The possible cause for this effect is an additional grain boundary effect, which can be explained as follows.

The composite thick film samples were designed as a sandwich structure, in which the central layer was the CFO-PZT heterogeneous composite layer, while the top and bottom ones were constituted by pure homogeneous PZT. The presence of grains from both materials (CFO-PZT and PZT) would make the composite thick film produce two different grain boundary effects. Moreover, The weaker R_2C_2 response should be attributed to the grain boundary effect between CFO and PZT grains, which is due to the lower CFO mass ratio in PZT matrix for CFO-PZT layer in this composite design.

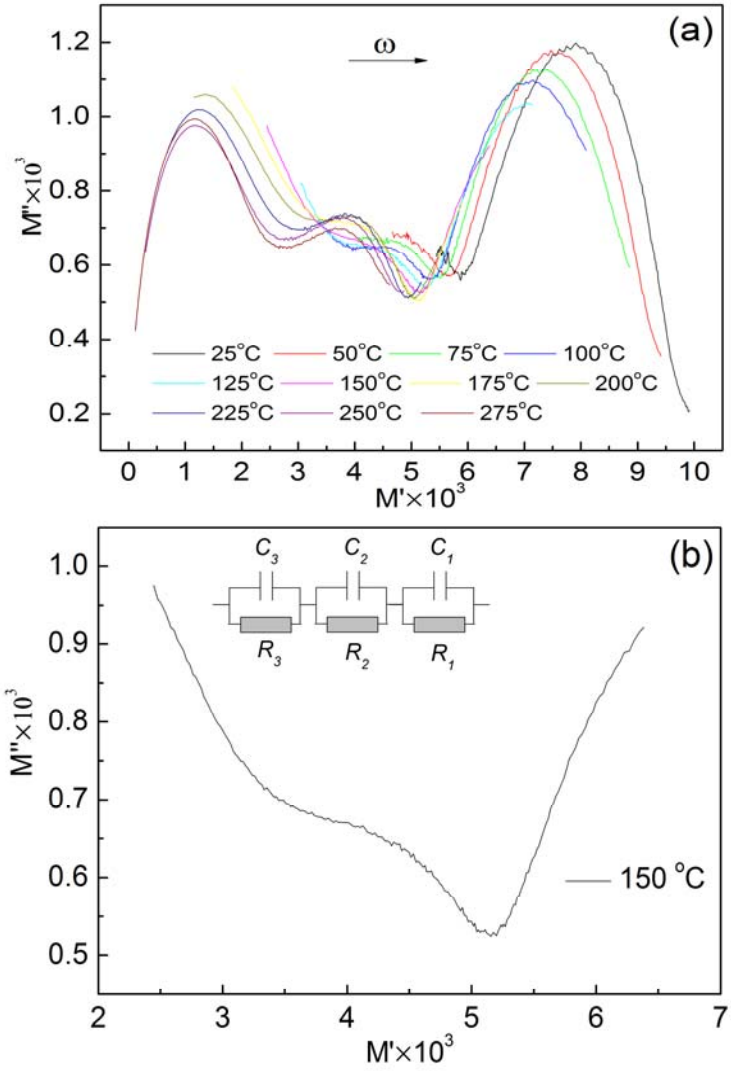

Figure 6-34 M' **vs.** M'' **plots with temperature as a parameter for: (a) The CFO-PZT composite thick film, and (b) detail of the curve at 150°C. The inset in (b) corresponds to the equivalent electric circuit.**

The value of C_2 could be extracted from the semicircular arc intercepts on the M' axis in Figure 6-34(b), while C_2 and f_{max} data were used to calculate R_2 using equation 6-4:

$$\omega\tau = 2\pi f_{\max} RC = 1, \qquad (6\text{-}4)$$

where f_{max} is the frequency of maxima of semicircular arcs and τ is the relaxation time. The calculated C_1 and R_1 were 142 pF and 295 kΩ respectively. At 150°C, it was not possible to calculate R_1 and R_3 exactly in the same manner as f_{max} for the semicircular arc corresponding to R_2C_2 as their maximum frequencies were beyond the measurable frequency range.

Figure 6-35 presents the frequency dependence of the imaginary electric modulus at all temperatures. It can be seen from Figure 6-35(a) that a well-defined relaxation peak appeared for all temperatures in the range 25-125°C. Meanwhile, a quasi-constant behavior was also observed at the low frequencies preceding the relaxation peak, which should be attributed to the CFO-PZT grain boundary effect due to the low resistivity of the CFO phase [128], leading to its easier thermal activation than the insulated PZT phase. Furthermore, both the relaxation peak and its preceding slowly-varying region shifted to higher frequencies with increasing temperature.

When the temperature reached 150°C, the high frequency relaxation peak has completely degraded and only its left wing was observed at this temperature, as seen in Figure 6-35(b). Furthermore, the quasi-constant plateau initially observed at low frequency gradually transformed into another peak with further increasing temperature, as can be seen in Figure 6-35(c), where it has totally formed into a very broad relaxation peak. Moreover, the third relaxation peak, which was even narrower than the first relaxation peak observed below 125°C, appeared into the frequency scanning range and shifted to high frequencies with further increasing temperature.

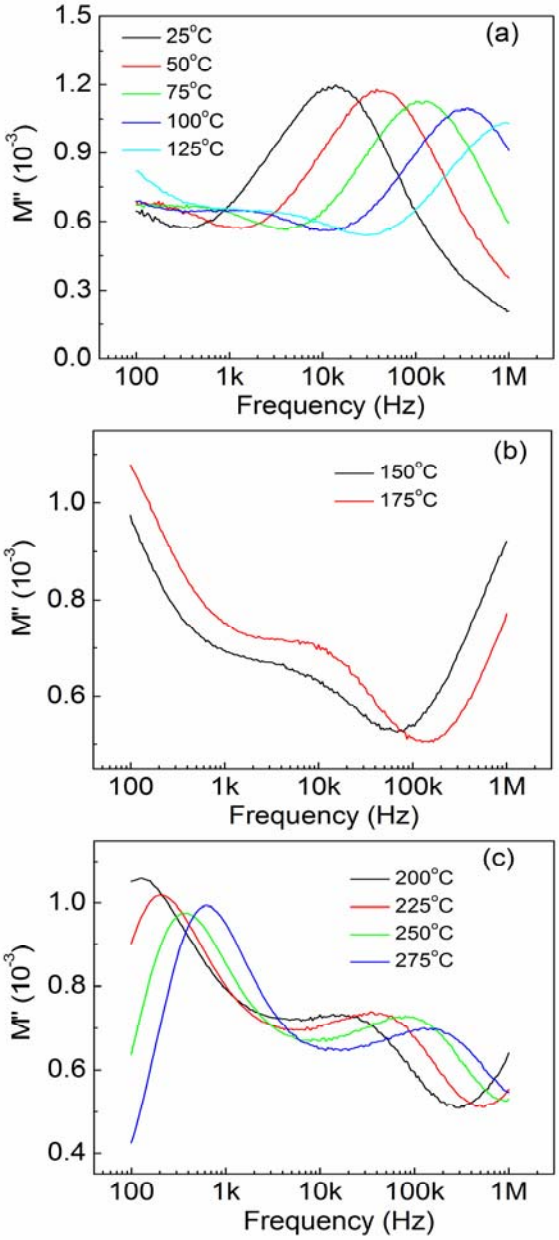

Figure 6-35 Temperature dependence of the imaginary electrical modulus spectral of CFO-PZT composite thick film: (a) from 25 to 125°C, (b) at 150 and 175°C, (c) between 200-275°C.

From the evolving process of these relaxation behaviors, we could see three responses in electric modulus spectra which were consistent with the observations in Figure 6-34. From 25 to 125°C, the first two responses coexisted: one was the high frequency relaxation peak; the other was quasi-

constant plateau that corresponds to a step-like relaxation behavior. At 150 and 175^{o}C, this latter relaxation behavior was dominant. Above 175^{o}C, another narrow low frequency relaxation peak appeared and predominated in the frequency window along with a strengthened step-like behavior at high frequencies. Both relaxation peaks mentioned (except the one due to the step-like behavior) actually corresponded to the two weak relaxation behaviors in the impedance spectra shown in Figure 6-32. This is similar to the situation of the CFO-PZT multilayered thin films [106], where a broad relaxation peak appears at low temperatures and high frequencies and another narrow relaxation peak is observed at high temperature and low frequencies in the modulus spectra, these two peaks are attributed to the grain effect and grain boundary effect, respectively. However, the step-like behavior communicating both relaxation peaks was not reported in earlier literature [106], and which is considered to be due to a heterogeneous CFO-PZT grain boundary effect.

The activation energies of these three features of interest were extracted from Figure 6-35 in terms of Arrhenius law. The value corresponding to the peaks shown in Figure 6-35(a) was 0.43 eV; while the calculated values for the low- and high-frequency peaks shown in Figure 6-35(c) were 0.65 eV and 0.47 eV, respectively. It can thus be concluded that the activation energy of $E_{ave} = 0.58$ eV estimated from the high temperature impedance relaxation shown in Figure 6-32, is the result of the contribution from both values of $E_{high} = 0.47$ eV and $E_{low} = 0.65$ eV, hence both types of grain boundary effects in modulus spectra should co-contribute to this average effect. The other activation energy of 0.43 eV calculated from the modulus spectra was due to

the grain effect, which was not expressed clearly in impedance spectra. Both activation energy values from the grain effect and average grain boundary effect are comparable with the values of 0.4187 eV and 0.5684 eV reported for three-layer CFO-PZT thin films [106]. This also confirms the results obtained in the present work.

6.6.4 DIELECTRIC BEHAVIOR

Real and imaginary dielectric constants (*ε' and ε''*) were plotted against the frequency at all temperatures, as shown in Figure 6-36. The results show that real dielectric constant increased with temperature but decreased with frequency. For example, at 1 MHz, the *ε'* value was increased from 215 to 455 when the temperature was raised from 25 to 275^{o}C, while at 100 Hz, the *ε'* value was increased dramatically from 385 to 1349 under the same temperature range. This indicated a strong low frequency dispersion phenomenon in the real dielectric constant. In addition, a dielectric relaxation behavior was observed at high frequencies but below 150^{o}C. The plots of the imaginary part of dielectric constant versus frequency were shown in Figure 6-36(b) for temperatures from 25 to 150^{o}C and in Figure 6-36(c) for temperatures from 175 to 275^{o}C. A peak was observed in *ε''* versus frequency plots at and below 150^{o}C [Figure 6-36(b)], which corresponded to the relaxation behavior in *ε'* curve. Above 175^{o}C, no peak in the *ε''* curve was observed in the measurable frequency range but several features were exhibited in Figure 6-36(c).

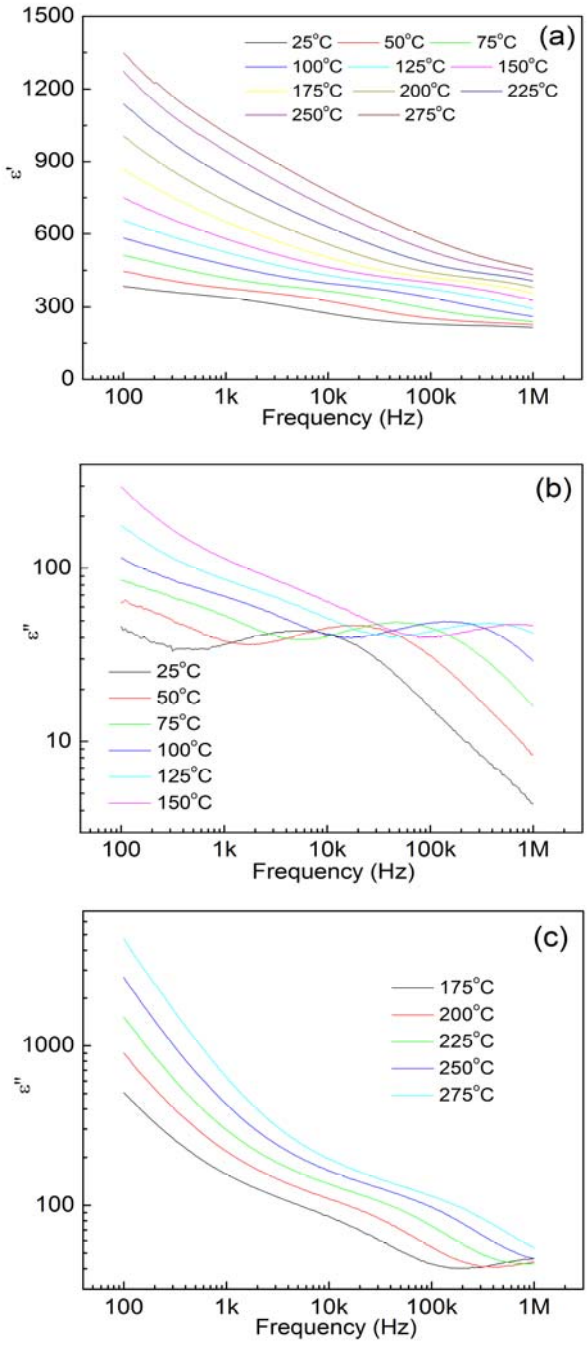

Figure 6-36 Temperature and frequency dependence of: (a) real dielectric permittivity (ε') of CFO-PZT composite thick film, (b) its dependent imaginary dielectric permittivity (ε'') from 25 to 150°C, and (c) from 175-275°C.

First, the slope of the straight line of log-log plot at low frequency side equaled -1, which was the natural result of the frequency independent

conduction. Second, a nearly constant loss region at intermediate frequencies indicated an increasing conductivity with frequency as explained by equation 6-2. Third, another nearly constant loss region at the high frequency side was indicative of another increasing conductivity region.

6.6.5 AC CONDUCTIVITY

Figure 6-37 shows the A.C. conductivity curves of the CFO-PZT composite thick film as a function of frequency at different temperatures. It can be seen from Figure 6-37 that conductivity value increased with frequency. Take the minimum and maximum measured temperature as examples. With increasing frequency, the conductivity values were increasing from $2.5*10^{-9}$ $\Omega^{-1}cm^{-1}$ and $2.6*10^{-7}$ $\Omega^{-1}cm^{-1}$ at 100 Hz to $2.5*10^{-6}$ $\Omega^{-1}cm^{-1}$ and $3.0*10^{-5}$ $\Omega^{-1}cm^{-1}$ at 1 MHz when temperature was raised from 25 to 275^{o}C, respectively. This behavior is due to a normal thermal mechanism. These conductivity values were slightly smaller than those of the multilayered CFO-PZT films [106], indicating a high quality of the present composite thick films.

Figure 6-37(a) shows two features at and below 125^{o}C. First, there was a strong rise at low frequencies, which was due to the grain boundary blocking effect. Second, the conductivity did not increase rapidly at high frequencies, but showed a temperature dependent dispersion behavior. This was due to the dielectric relaxation shown in Figure 6-36, which was ascribed to the bulk conductivity relaxation. The σ in the second feature could be described by the "universal dielectric response" (UDR) [192], see Equation 5-7. This equation is common for most disordered systems and amorphous semiconductors [192], as well as thermal assisted tunneling between localized states. In our system, it

might be ascribed to the polaron relaxation [190], where ion hopping was restricted by the low temperature and high frequency, which could not provide the ions with enough high energy or available time to hop out of their sites, resulting in the ions vibrating in their own sites iteratively.

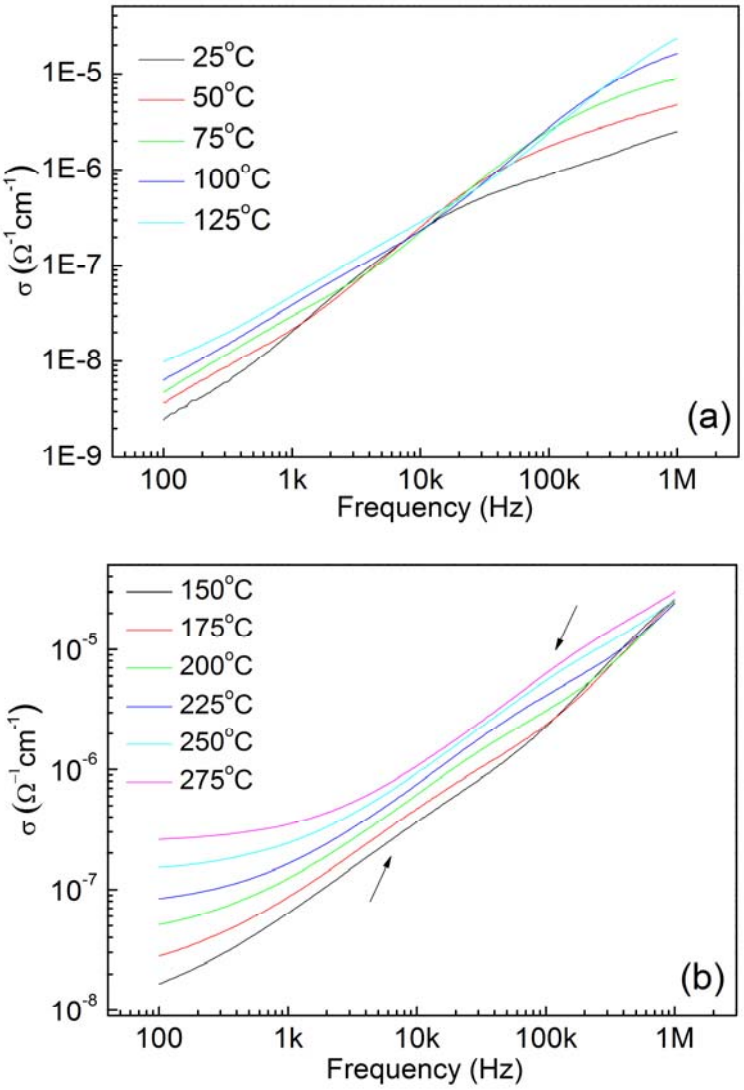

Figure 6-37 Temperature dependent A.C. conductivity spectra (σ') of CFO-PZT composite thick film from 25 to 150°C (a) and 175-275°C (b).

Figure 6-37(b) shows three features for the conductivity spectra above 150°C. The first is the tendency of the low frequency conductivity curves to

flatten with further increasing temperature, suggesting a D.C. conductivity behavior. It can be clearly seen that this frequency-independent conductivity strengthened with increasing temperature, which is consistent with the low frequency slope in the dielectric spectra [Figure 6-36(c)].

The second feature is a weak conductivity relaxation at intermediate frequencies (with ends marked by two arrows), which shifted to higher frequencies with increasing temperature.

The third feature is that the conductivity curves merged together at high frequencies but also showed a linearly increase with temperature. The whole conductivity curve was similar to that of CFO-PZT multilayered thin films below 500 K [106], but much attention was paid only to the conductivity behavior above 500 K in this paper. For our CFO-PZT composite thick film, the jump relaxation model [168] could explain its conductivity characteristics. The frequency independent plateau at low frequencies is attributed to the long-range translational motion of ions. According to this model, the conductivity at the low frequency region is associated with successful hops of the ions in the lattice to their closest vacant site neighborhood due to the long time available for this phenomenon to occur. Unfortunately, for the high frequency conductivity behavior, the time is insufficient for most of ions to hop from their own sites, so in this case the conductivity mechanism should be attributed to the vibrational relaxation caused by anharmonicity [193] where unsuccessfully ions jumps should be responsible. When the temperature was increased from 150 to 275^{o}C, the slope of the conductivity curve gradually decreased, indicative of a thermal

mechanism, i.e. more thermal energy was supplied to most of the ions and thus resulting in a larger number of successful hopping events.

6.6.6 BRIEF SUMMARY

Detailed dielectric studies of multiferroic $CoFe_2O_4$-$Pb(Zr_{0.53}Ti_{0.47})O_3$ composite thick films were conducted in this section. Impedance spectroscopy and electric modulus analysis indicated the contributions from grains and grain boundary effect at different frequencies and temperatures, resulting in two different grain boundary effects being observed in the dielectric modulus spectra. Activation energy calculated from two methods kept in good agreement with one another. Dielectric spectra revealed a polaron relaxation below 150^{o}C whereas above this temperature, D.C. conductivity region and two nearly constant loss regions were observed, which were also demonstrated in the A.C. conductivity spectra. Furthermore, ion hopping and transport were also revealed by A.C. conductivity analysis, jump relaxation mode was well used to clarify them.

CHAPTER 7 CONCLUSIONS AND RECOMMENDATIONS

7.1 CONCLUSIONS

This thesis aimed at fabricating CFO-PZT thick films and investigating their multiferroic behaviors for potential magnetoelectric (ME) application. The two basic requirements for such an application are: (a) the ferromagnetic and ferroelectric properties should be strong enough; (b) the resultant material should exhibit a dense microstructure. For which a convenient stress-driven ME voltage could be achieved. In order to understand this multiferroic system in detail and then achieve the significant ferromagnetic and ferroelectric properties in CFO-PZT thick films, the following research has been conducted and summarized in this chapter.

7.1.1 SCREEN PRINTED CFO-PZT THICK FILMS

CFO-PZT multiferroic thick films were initially prepared by means of screen printing method on alumina substrates, allowing a low sintering temperature. Both the ferromagnetic and ferroelectric properties of the final films were characterized at room temperature. Compared with CFO-PZT thin films previously reported in literature, our quantitative analysis revealed a poor multiferroic behavior due to the large porosities in the composite thick films, which severely diminished the expected ME coupling effect. Another method to prepare CFO-PZT thick films was hence developed.

7.1.2 HYBRID SOL-GEL PROCESSING

In order to replace the screen printed process, a hybrid fabrication technology was developed by combining CFO, PZT nanoparticles and sol-gel precursor to deposit CFO and PZT thick films individually on platinum coated silicon substrate through spin coating technique. CFO and PZT nanoparticles were produced by high energy ball milling. The sol-gel precursor was prepared below 300^{o}C. When these sol-gel precursors were dissolved into solution and deposited on SiO_2/Si wafer, pure CFO and PZT phases were obtained after annealing. With mixing the nano-sized particles and sol-gel solutions, uniform CFO and PZT thick films were prepared thereafter.

7.1.3 COATING OF CFO COMPOSITE THICK FILMS AND ELECTRICAL PROPERTIES

The phase structure and microstructure of the CFO thick films were evaluated after annealing between 550 and 700^{o}C by means of XRD and SEM techniques. Pure spinel phase was observed after annealing above 600^{o}C and the thickness of the films reached up to 10 μm. With increasing annealing temperature, both the saturation magnetization and magnetic coercive field increased. A dielectric relaxation was found in the frequency range 10 Hz to 10 kHz and strengthened with increasing annealing temperature. Complex Z'-Z'' plots revealed that the cause of this relaxation in all the samples was grain effect. Investigation on conductivity spectra via the universal dynamic response law revealed the appearance of the obvious electrode polarization effect at the annealing temperature of 700^{o}C and above. Further temperature and frequency dependent-impedance studies of the typical samples revealed other interesting

phenomena as well, such as double impedance relaxation and double D.C. plateau in the conductivity spectra. The governing physical mechanisms were also discussed in detail. The results of these studies of our CFO thick film indicated it is a potential good starting point for further investigations of the electric conductivity mechanism in other ferrites.

7.1.4 Deposition of CFO-PZT multiferroic thick films and optimizations

CFO-PZT composite thick films were prepared through the developed hybrid sol-gel processing. Their ferromagnetic and ferroelectric properties were characterized simultaneously at room temperature. Consistent optimizations through organic addition and sol infiltration were carried out. It was shown that organic PVP was beneficial for avoiding cracks and enhancing film thickness. Sufficient sol infiltration could enhance the ferroelectric and dielectric properties of CFO-PZT thick films due to its improvement on film densification. Ferromagnetic properties were also enhanced due to the structural and physical benefits derived from the PVP and sol infiltration. With dense microstructure and balanced ferroelectric and ferromagnetic properties, a ME coupling effect was highly expected in CFO-PZT composite thick films. In addition, the dielectric relaxation behavior of multiferroic thick films was also investigated, and the results indicated that it was weaker than that of pure CFO thick films. Dielectric studies were also conducted to understand these phenomena. The physical mechanisms were also discussed in detail in the thesis.

7.2 Recommendations

The results of our experiments included the development of a hybrid sol-gel fabrication process for magnetic and multiferroic thick films and their detailed characterizations. However, there are still several questions that need to be answered.

Although ferromagnetic and ferroelectric properties of multiferroic thick films have been characterized in this thesis, providing indirect evidence for the presence of the ME effect, the direct measurement data on the ME effect are still not sufficient. The reason is that a special measurement system exclusively dedicated for the characterization of multiferroic thick films should be set-up, calibrated and used instead of that employed for bulk materials. For example, the measured ME signal in CFO-PZT thick films [194], compared with those measured in bulk materials using the same set-up [11], is much lower, and therefore, the signal-to-noise (SIN) ratio is significantly reduced. Therefore, a lock-in amplifier with matched impedance should be added to the bulk measurement system. In addition, a shielded measurement environment is strictly demanded, and for this purpose a dedicated Faraday cage capable of low-frequency magnetic field shielding should be used.

Here, we recommend to build a ME measurement system for thick/thin films characterization which would detect the static effect of the electric field on the magnetization and the effect of the magnetic field on the polarization. The films during magnetic measurement need to be wire bonded to an A.C. generator providing the excitation signal for the study of the effect of the electric field on the magnetization. Similarly, the set-up should be able to generate a variable magnetic field necessary to measure the films magnetic and

ferroelectric hysteresis loops. Because the ME effect is a very important factor when studying the feasibility of ME applications, based on the achievement of good ferroelectric and ferromagnetic properties in the CFO-PZT composite thick films in this thesis, their dynamic ME effect should be characterized using a novel measurement system, shown in Figure 7-1.

A computer-controlled Helmholtz coil is mounted on the pole pieces of a D.C. electromagnet, which should generate a time-varying magnetic field. The time-varying D.C. magnetic field can be achieved by programming the output current to the delivered by the coil's power supply. Through this setup, the dynamic ME effect in films can be measured. Moreover, the linear and higher order ME coefficients can also be evaluated from the output voltage. The successful characterization of the ME effect by the above experimental setup will enable an easier evaluation of their potential ME application.

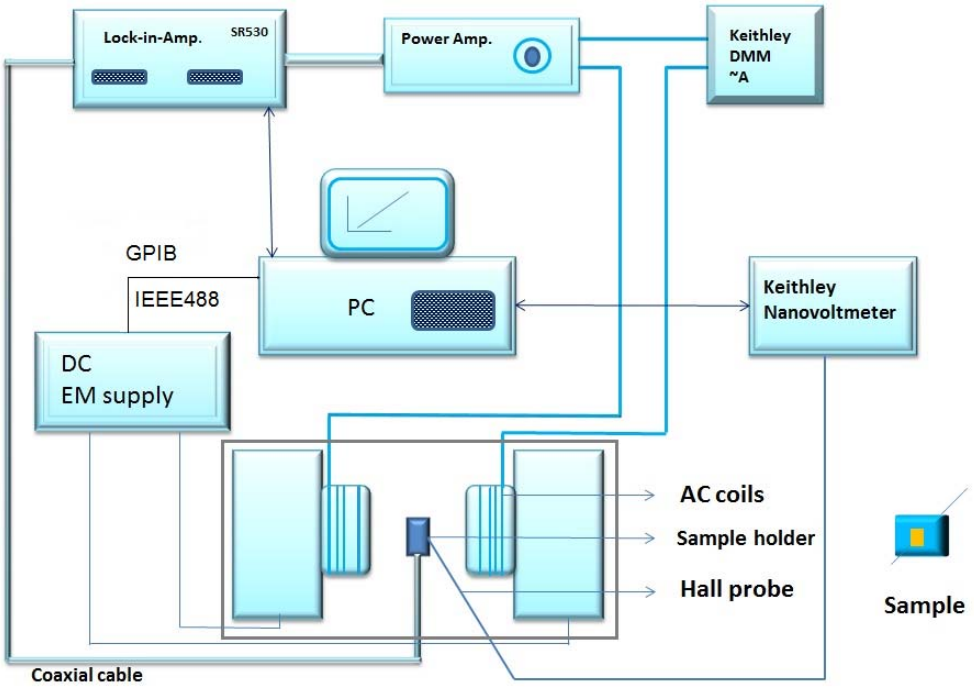

Figure 7-1 Block diagram of dynamic ME experimental setup [195].

PUBLICATIONS LIST

Book:

1. **W. Chen**, W. Zhu, and Z. H. Wang, "Fabrication and property optimization of multiferroic composite thick films", (2010) Book: The Sol-Gel Process: Uniformity, Polymers and Applications, ISBN: 978-1-61761-321-0, Nova Science Publisher, Inc. New York.
2. **W. Chen**, and W. Zhu, "Deposition of $CoFe_2O_4$ thick films and properties characterizations", (2011) Book: Ferroelectrics, ISBN: 978-953-307-557-0, InTech-Open Access Publisher, Rijeka.

Journal Paper:

1. **W. Chen** and W. G. Zhu, "Preparation of cobalt ferrite thick films and their magnetic and electrical properties", ***J. Am. Ceram. Soc.***, 94 (2011) 1096-1100.
2. **W. Chen**, X. F. Chen, L. L. Sun, O. K. Tan, and W. Zhu, "Preparation of $(Ni_{0.5}Zn_{0.5})Fe_2O_4/Pb(Zr_{0.53}Ti_{0.47})O_3$ thick films and their magnetic and ferroelectric properties", ***Mater. Chem. Phys.***, 127 (2011) 70-73.
3. **W. Chen**, C. X. Huang, T. S. Yan, W. Zhu, Z. P. Li, X. F. Chen, and O. K. Tan, "Synthesis of $CoFe_2O_4$-$Pb(Zr_{0.53}Ti_{0.47})O_3$ multiferroic composite thick films by low-sintering-temperature screen printing method", ***J. Adv. Dielectrics***, 1 (2011) 119-125.
4. **W. Chen**, W. Zhu, C. Ke, Z. Yang, L. Wang, X. F. Chen, and O. K. Tan, "Impedance spectroscopy and conductivity mechanism of $CoFe_2O_4$-

$Pb(Zr_{0.53}Ti_{0.47})O_3$ composite thick films", ***J. Alloys Compd.***, 508 (2010) 141-146.

5. **W. Chen**, W. Zhu, O. K. Tan, and X. F. Chen, "Frequency and temperature dependent impedance spectroscopy of cobalt ferrite composite thick films", ***J. Appl. Phys.***, 108 (2010) 034101-7.
6. **W. Chen**, W. G. Zhu, X. F. Chen, and Z. H. Wang, "Enhanced ferroelectric and dielectric properties of $CoFe_2O_4$-$Pb(Zr_{0.53}Ti_{0.47})O_3$ multiferroic composite thick films", ***J. Am. Ceram. Soc.***, 93 (2010) 796-799.
7. **W. Chen**, S. Shannigrahi, X. F. Chen, Z. H. Wang, W. Zhu, and O. K. Tan, "Multiferroic behavior and magnetoelectric effect in $CoFe_2O_4$/$Pb(Zr_{0.53}Ti_{0.47})O_3$ thick films", ***Solid State Commun.***, 150 (2010) 271-274.
8. **W. Chen**, X. F. Chen, Z. H. Wang, W. Zhu, and O. K. Tan, "Microstructure, ferromagnetic, and ferroelectric properties in polyvinylpyrrolidone-assisted $CoFe_2O_4$/$Pb(Zr_{0.53}Ti_{0.47})O_3$ multiferroic composite thick films", ***J. Mater. Sci.***, 44 (2009) 4939-4943.
9. **W. Chen**, Z. H. Wang, C. Ke, W. Zhu, and O. K. Tan, "Preparation and characterization of $Pb(Zr_{0.53}Ti_{0.47})O_3$/$CoFe_2O_4$ composite thick films by hybrid sol-gel processing", ***Mater. Sci. Eng. B***, 162 (2009) 47-52.
10. **W. Chen**, Z. H. Wang, W. Zhu, and O. K. Tan, "Ferromagnetic, ferroelectric and dielectric properties of $Pb(Zr_{0.53}Ti_{0.47})O_3$/$CoFe_2O_4$ multiferroic composite thick films", ***J. Phys. D***, 42 (2009) 075421-5.

BIBLIOGRAPHY

1. M. Fiebig, *"Revival of the magnetoelectric effect"*. J. Phys. D, 2005. **38**: p. R123-R152.
2. N. A. Spaldin and M. Fiebig, *"The renaissance of magnetoelectric multiferroics"*. Science, 2005. **309**: p. 391-392.
3. N. A. Hill, *"Why are there so few magnetic ferroelectrics?"*. J. Phys. Chem. B, 2000. **104**: p. 6694-6709.
4. H. Schmid, *"Multi-ferroic magnetoelectrics "*. Ferroelectr., 1994. **162**: p. 317-338.
5. E. Ascher, et al., *"Some properties of ferromagnetoelectric nickel-Iodine boracite, $Ni_3B_7O_{13}I$"*. J. Appl. Phys., 1966. **37**: p. 1404-1405.
6. J. Wang, et al., *"Epitaxial $BiFeO_3$ multiferroic thin film heterostructures"*. Science, 2003. **299**: p. 1719-1722.
7. T. Kimura, et al., *"Magnetic control of ferroelectric polarization"*. Nature, 2003. **426**: p. 55-58.
8. N. Hur, et al., *"Electric polarization reversal and memory in a multiferroic material induced by magnetic fields"* Nature, 2004. **429**: p. 392-395.
9. W. Prellier, M. P. Singh, and P. Murugavel, *"The single-phase multiferroic oxides: from bulk to thin film"*. J. Phys. Conden. Matt., 2005. **17**: p. R803-R832.
10. S. W. Cheong and M. Mostovoy, *"Multiferroics: a magnetic twist for ferroelectricity"*. Nat. Mater., 2007. **6**: p. 13-20.

11. C. W. Nan, et al., *"Multiferroic magnetoelectric composites: Historical perspective, status, and future directions"*. J. Appl. Phys., 2008. **103**: p. 031101-35.

12. W. Eerenstein, N. D. Mathur, and J. F. Scott, *"Multiferroic and magnetoelectric materials"*. Nature, 2006. **442**: p. 759-765.

13. T. Lottermoser, et al., *"Magnetic phase control by an electric field"*. Nature, 2004. **430**: p. 541-544.

14. G. Giovannetti, et al., *"Multiferroicity in rare-earth nickelates $RNiO_3$"*. Phys. Rev. Lett., 2009. **103**: p. 156401-4.

15. K. F. Wang, J. M. Liu, and Z. F. Ren, *"Multiferroicity: the coupling between magnetic and polarization orders"*. Adv. Phys., 2009. **58**: p. 321-448.

16. G. Catalan and J. F. Scott, *"Physics and applications of bismuth ferrite"*. Adv. Mater., 2009. **21**: p. 2463-2485.

17. G. Srinivasan, *"Magnetoelectric composites"*, in *Annu. Rev. Mater. Res.* 2010. p. 153-178.

18. J. Ma, et al., *"Recent progress in multiferroic magnetoelectric composites: from bulk to thin Films"*. Adv. Mater., 2011. **23**: p. 1062-1087.

19. R. A. Islam and S. Priya, *"Effect of piezoelectric grain size on magnetoelectric coefficient of $Pb(Zr_{0.52}Ti_{0.48})O_3$-$Ni_{0.8}Zn_{0.2}Fe_2O_4$ particulate composites"*. J. Mater. Sci., 2008. **43**: p. 3560-3568.

20. R. A. Islam, et al., *"Giant magnetoelectric effect in sintered multilayered composite structures"*. J. Appl. Phys., 2008. **104**: p. 044103-5.

21. J. Ryu, et al., *"Magnetoelectric effect in composites of magnetostrictive and piezoelectric materials"*. J. Electroceram., 2002. **8**: p. 107-119.

22. K. Mori and M. Wuttig, *"Magnetoelectric coupling in terfenol-D/polyvinylidenedifluoride composites"*. Appl. Phys. Lett., 2002. **81**: p. 100-101.

23. S. X. Dong, et al., *"Magnetoelectric effect in Terfenol-D/Pb(Zr,TiO)$_3$/u-metal laminate composites"*. Appl. Phys. Lett., 2006. **89**: p. 122903-3.

24. Z. Fang, et al., *"Enhancing the magnetoelectric response of metglas/polyvinylidene fluoride laminates by exploiting the flux concentration effect"*. Appl. Phys. Lett., 2009. **95**: p. 112903-3.

25. H. Greve, et al., *"Giant magnetoelectric coefficients in (Fe90Co10)(78)Si12B10-AlN thin film composites"*. Appl. Phys. Lett., 2010. **96**: p. 182501-3.

26. J. X. Zhang, et al., *"The effect of magnetic nanoparticles on the morphology, ferroelectric, and magnetoelectric behaviors of CFO/P(VDF-TrFE) 0-3 nanocomposites"*. J. Appl. Phys., 2009. **105**: p. 054103-6.

27. S. X. Dong, et al., *"Piezoelectric ultrasonic micromotor with 1.5 mm diameter"*. IEEE Trans. Ultrason. Ferroelectr. Freq. Control, 2003. **50**: p. 361-367.

28. S. X. Dong, et al., *"A small, linear, piezoelectric ultrasonic cryomotor"*. Appl. Phys. Lett., 2005. **86**: p. 053501-3.

29. S. X. Dong, et al., *"A piezoelectric single crystal traveling wave step motor for low-temperature application"*. Appl. Phys. Lett., 2008. **92**: p. 153504-3.

30. S. X. Dong, et al., *"Giant magnetoelectric effect (under a dc magnetic bias of 2 Oe) in laminate composites of FeBSiC alloy ribbons and $Pb(Zn_{1/3},Nb_{2/3})O_3$-7%$PbTiO_3$ fibers".* Appl. Phys. Lett., 2007. **91**: p. 022915-3.

31. S. X. Dong, et al., *"Extremely low frequency response of magnetoelectric multilayer composites".* Appl. Phys. Lett., 2005. **86**: p. 102901-3.

32. S. X. Dong, et al., *"Fe-Ga/$Pb(Mg_{1/3}Nb_{2/3})O_3$-$PbTiO_3$ magnetoelectric laminate composites".* Appl. Phys. Lett., 2005. **87**: p. 222504-3.

33. S. X. Dong, et al., *"Multimodal system for harvesting magnetic and mechanical energy".* Appl. Phys. Lett., 2008. **93**: p. 103511-3.

34. S. X. Dong, et al., *"Magnetoelectric gyration effect in $Tb_{1-x}Dy_xFe_{2-y}$/$Pb(Zr,Ti)O_3$ laminated composites at the electromechanical resonance".* Appl. Phys. Lett., 2006. **89**: p. 243512-3.

35. S. X. Dong, et al., *"Strong magnetoelectric charge coupling in stress-biased multilayer-piezoelectric/magnetostrictive composites".* J. Appl. Phys., 2007. **101**: p. 124102-4.

36. S. X. Dong, et al., *"Enhanced magnetoelectric effect in three-phase $MnZnFe_2O_4$/$Tb_{1-x}Dy_xFe_{2-y}$/$Pb(Zr,Ti)O_3$ composites".* J. Appl. Phys., 2006. **100**: p. 124108-4.

37. S. X. Dong, et al., *"Near-ideal magnetoelectricity in high-permeability magnetostrictive/piezofiber laminates with a (2-1) connectivity".* Appl. Phys. Lett., 2006. **89**: p. 252904-3.

38. S. X. Dong, et al., *"Small dc magnetic field response of magnetoelectric laminate composites".* Appl. Phys. Lett., 2006. **88**: p. 082907-2.

39. S. X. Dong, et al., *"Magnetostrictive and magnetoelectric behavior of Fe-20 at. % Ga/Pb(Zr,Ti)O_3 laminates".* J. Appl. Phys., 2005. **97**: p. 103902-6.

40. S. X. Dong, et al., *"A strong magnetoelectric voltage gain effect in magnetostrictive-piezoelectric composite".* Appl. Phys. Lett., 2004. **85**: p. 3534-3536.

41. S. X. Dong, J. F. Li, and D. Viehland, *"Circumferentially magnetized and circumferentially polarized magnetostrictive/piezoelectric laminated rings".* J. Appl. Phys., 2004. **96**: p. 3382-3387.

42. S. X. Dong, J. F. Li, and D. Viehland, *"Vortex magnetic field sensor based on ring-type magnetoelectric laminate".* Appl. Phys. Lett., 2004. **85**: p. 2307-2309.

43. S. X. Dong, J. F. Li, and D. Viehland, *"A longitudinal-longitudinal mode Terfenol-D/Pb($Mg_{1/3}Nb_{2/3}$)O_3-$PbTiO_3$ laminate composite".* Appl. Phys. Lett., 2004. **85**: p. 5305-5306.

44. S. X. Dong, J. F. Li, and D. Viehland, *"Characterization of magnetoelectric laminate composites operated in longitudinal-transverse and transverse-transverse modes".* J. Appl. Phys., 2004. **95**: p. 2625-2630.

45. S. X. Dong, J. F. Li, and D. Viehland, *"Voltage gain effect in a ring-type magnetoelectric laminate".* Appl. Phys. Lett., 2004. **84**: p. 4188-4190.

46. S. X. Dong, J. F. Li, and D. Viehland, *"Ultrahigh magnetic field sensitivity in laminates of TERFENOL-D and Pb($Mg_{1/3}Nb_{2/3}$)O_3-$PbTiO_3$ crystals".* Appl. Phys. Lett., 2003. **83**: p. 2265-2267.

47. C. A. F. Vaz, et al., *"Magnetoelectric coupling effects in multiferroic complex oxide composite structures"*. Adv. Mater., 2010. **22**: p. 2900-2918.

48. T. Kimura, et al., *"Magnetocapacitance effect in multiferroic $BiMnO_3$"*. Phys. Rev. B, 2003. **67**: p. 180401-4.

49. Z. H. Wang, J. M. Miao, and W. G. Zhu, *"Micromachined ultrasonic transducers and arrays based on piezoelectric thick film"*. Appl. Phys. A, 2008. **91**: p. 107-117.

50. J. P. Zhou, Z. C. Qiu, and P. Liu, *"Electric and magnetic properties of $Pb(Zr_{0.52}Ti_{0.48})O_3$-$CoFe_2O_4$ particle composite thin film on the $SrTiO_3$ substrate"*. Mater. Res. Bull., 2008. **43**: p. 3514-3520.

51. R. J. Lin, T. B. Wu, and Y. H. Chu, *"Interface effects on the magnetoelectric properties of (00l)-oriented $Pb(Zr_{0.5}Ti_{0.5})O_3/CoFe_2O_4$ multilayer thin films"*. Scr. Mater., 2008. **59**: p. 897-900.

52. C. H. Sim, A. Z. Z. Pan, and J. Wang, *"Thickness and coupling effects in bilayered multiferroic $CoFe_2O_4/Pb(Zr_{0.52}Ti_{0.48})O_3$ thin films"*. J. Appl. Phys., 2008. **103**: p. 124109-7.

53. H. C. He, et al., *"Orientation-dependent multiferroic properties in $Pb(Zr_{0.52}Ti_{0.48})O_3$-$CoFe_2O_4$ nanocomposite thin films derived by a sol-gel processing"*. J. Appl. Phys., 2008. **103**: p. 034103-5.

54. N. Ortega, et al., *"Multiferroic properties of $Pb(Zr,Ti)O_3/CoFe_2O_4$ composite thin films"*. J. Appl. Phys., 2006. **100**: p. 126105-3.

55. J. P. Zhou, et al., *"Dielectric, magnetic, and magnetoelectric properties of laminated $PbZr_{0.52}Ti_{0.48}O_3/CoFe_2O_4$ composite ceramics"*. J. Appl. Phys., 2006. **100**: p. 094106-6.

56. W. Zhu, et al., *"Low temperature processing of nanocrystalline lead zirconate titanate (PZT) thick films and ceramics by a modified sol-gel route".* Jpn. J. Appl. Phys., 2002. **41**: p. 6969-6975.

57. H. C. He, et al., *"Ferroelectric and ferromagnetic behavior of $Pb(Zr_{0.52}Ti_{0.48})O_3$-$Co_{0.9}Zn_{0.1}Fe_2O_4$ multilayered thin films prepared via solution processing".* Adv. Funct. Mater., 2007. **17**: p. 1333-1338.

58. H. Zheng, et al., *"Multiferroic $BaTiO_3$-$CoFe_2O_4$ nanostructures".* Science, 2004. **303**: p. 661-663.

59. R. E. Newnham, D. P. Skinner, and L. E. Cross, *"Connectivity and piezoelectric-pyroelectric composites".* Mater. Res. Bull., 1978. **13**: p. 525-536.

60. P. R. Solomon, *"Voltage associated with the coupled motion of flux in type-I superconductors".* Phys. Rev. Lett., 1966. **16**: p. 50-52.

61. A. M. J. G. Vanrun, D. R. Terrell, and J. H. Scholing, *"In situ grown eutectic magnetoelectric composite material: Physical properties".* J. Mater. Sci., 1974. **9**: p. 1710-1714.

62. J. V. D. Boomgaard, et al., *"Insitu grown eutectic magnetoelectric composite material: Composition and unidirectional solidification"* J. Mater. Sci., 1974. **9**: p. 1705-1709.

63. J. V. D. Boomgaard and R. A. J. Born, *"A sintered magnetoelectric composite material $BaTiO_3$-$Ni(Co,Mn)Fe_2O_4$".* J. Mater. Sci., 1978. **13**: p. 1538-1548.

64. C. W. Nan, *"Magnetoelectric effect in composites of piezoelectric and piezomagnetic phases".* Phys. Rev. B, 1994. **50**: p. 6082-6088.

65. C. W. Nan and D. R. Clarke, *"Effective properties of ferroelectric and/or ferromagnetic composites: A unified approach and its application"*. J. Am. Ceram. Soc., 1997. **80**: p. 1333-1340.

66. Y. Benveniste, *"Magnetoelectric effect in fibrous composites with piezoelectric and piezomagnetic phases"*. Phys. Rev. B, 1995. **51**: p. 16424-27.

67. L. J. Li and J. Y. Li, *"Electromagnetic fields induced in a uniaxial multiferroic material by a point source or an ellipsoidal inclusion"*. Phys. Rev. B, 2006. **73**: p. 184416-7.

68. J. H. Huang, *"Analytical predictions for the magnetoelectric coupling in piezomagnetic materials reinforced by piezoelectric ellipsoidal inclusions"*. Phys. Rev. B, 1998. **58**: p. 12-15.

69. M. I. Bichurin, et al., *"Theory of magnetoelectric effects at magnetoacoustic resonance in single-crystal ferromagnetic-ferroelectric heterostructures"*. Phys. Rev. B, 2005. **72**: p. 060408-4.

70. G. Srinivasan, et al., *"Magnetoelectric bilayer and multilayer structures of magnetostrictive and piezoelectric oxides"*. Phys. Rev. B, 2001. **64**: p. 214408-6.

71. J. H. Ryu, et al., *"Effect of the magnetostrictive layer on magnetoelectric properties in lead zirconate titanate/terfenol-D laminate composites"*. J. Am. Ceram. Soc., 2001. **84**: p. 2905-2908.

72. C. W. Nan, M. Li, and J. H. Huang, *"Calculations of giant magnetoelectric effects in ferroic composites of rare-earth-iron alloys and ferroelectric polymers"*. Phys. Rev. B, 2001. **63**: p. 144415-9.

73. C. W. Nan, et al., *"Possible giant magnetoelectric effect of ferromagnetic rare-earth-iron-alloys-filled ferroelectric polymers".* Appl. Phys. Lett., 2001. **78**: p. 2527-2529.

74. J. Ryu, et al., *"Piezoelectric and magnetoelectric properties of Lead Zirconate Titanate/Ni-Ferrite particulate composites".* J. Electroceram., 2001. **7**: p. 17-24.

75. J. Y. Zhai, et al., *"Coupled magnetodielectric properties of laminated $PbZr_{0.53}Ti_{0.47}O_3/NiFe_2O_4$ ceramics".* J. Appl. Phys., 2004. **95**: p. 5685-5690.

76. X. M. Chen, et al., *"Dielectric and magnetoelectric characterization of $CoFe_2O_4/Sr_{0.5}Ba_{0.5}Nb_2O_6$ composites".* J. Appl. Phys., 2004. **96**: p. 6520-6522.

77. S. Q. Ren, et al., *"$BaTiO_3/CoFe_2O_4$ particulate composites with large high frequency magnetoelectric response".* J. Mater. Sci., 2005. **40**: p. 4375-4378.

78. V. M. Petrov, et al., *"Theory of magnetoelectric effects in ferrite piezoelectric nanocomposites".* Phys. Rev. B, 2007. **75**: p. 224407-6.

79. G. Srinivasan, et al., *"Magnetoelectric interactions in hot-pressed nickel zinc ferrite and lead zirconante titanate composites".* Appl. Phys. Lett., 2004. **85**: p. 2550-2552.

80. Q. H. Jiang, et al., *"Magnetoelectric composites of nickel ferrite and lead zirconnate titanate prepared by spark plasma sintering".* J. Eur. Ceram. Soc., 2007. **27**: p. 279-284.

81. J. G. Wan, et al., *"Magnetoelectric $CoFe_2O_4$-lead zirconate titanate thick films prepared by a polyvinylpyrrolidone-assisted sol-gel method"*. Appl. Phys. Lett., 2006. **89**: p. 122914-3.

82. V. Corral-Flores, et al., *"Enhanced magnetoelectric effect in core-shell particulate composites"*. J. Appl. Phys., 2006. **99**: p. 08J503-3.

83. G. Srinivasan, I. V. Zavislyak, and A. S. Tatarenko, *"Millimeter-wave magnetoelectric effects in bilayers of barium hexaferrite and lead zirconate titanate"*. Appl. Phys. Lett., 2006. **89**: p. 152508-3.

84. H. Zheng, et al., *"Three-dimensional heteroepitaxy in self-assembled $BaTiO_3$-$CoFe_2O_4$ nanostructures"*. Appl. Phys. Lett., 2004. **85**: p. 2035-2037.

85. J. G. Wan, et al., *"Magnetoelectric $CoFe_2O_4$-$Pb(Zr,Ti)O_3$ composite thin films derived by a sol-gel process"*. Appl. Phys. Lett., 2005. **86**: p. 122501-3.

86. J. P. Zhou, et al., *"Magnetoelectric $CoFe_2O_4/Pb(Zr_{0.52}Ti_{0.48})O_3$ double-layer thin film prepared by pulsed-laser deposition"*. Appl. Phys. Lett., 2006. **88**: p. 013111-3.

87. M. P. Singh, et al., *"Correlation between structure and properties in multiferroic $La_{0.7}Ca_{0.3}MnO_3/BaTiO_3$ superlattices"*. J. Appl. Phys., 2006. **99**: p. 024105-8.

88. H. C. He, et al., *"Multiferroic $Pb(Zr_{0.52}Ti_{0.48})O_3$-$Co_{0.9}Zn_{0.1}Fe_2O_4$ bilayer thin films via a solution processing"*. Appl. Phys. Lett., 2006. **89**: p. 052904-3.

89. T. Wu, et al., *"Observation of magnetoelectric effect in epitaxial ferroelectric film/manganite crystal heterostructures"*. Phys. Rev. B, 2006. **73**: p. 134416-6.

90. W. Eerenstein, et al., *"Giant sharp and persistent converse magnetoelectric effects in multiferroic epitaxial heterostructures"*. Nat. Mater., 2007. **6**: p. 348-351.

91. G. Liu, C. W. Nan, and J. Sun, *"Coupling interaction in nanostructured piezoelectric/magnetostrictive multiferroic complex films"*. Acta Mater., 2006. **54**: p. 917-925.

92. C. G. Duan, S. S. Jaswal, and E. Y. Tsymbal, *"Predicted magnetoelectric effect in Fe/$BaTiO_3$ multilayers: Ferroelectric control of magnetism"*. Phys. Rev. Lett., 2006. **97**: p. 047201-4.

93. J. X. Zhang, et al., *"Phase-field model for epitaxial ferroelectric and magnetic nanocomposite thin films"*. Appl. Phys. Lett., 2007. **90**: p. 052909-3.

94. X. Y. Lu, et al., *"Coupling interaction in 1-3-type multiferroic composite thin films"*. Appl. Phys. Lett., 2007. **90**: p. 133124-3.

95. C. W. Nan, et al., *"Magnetic-field-induced electric polarization in multiferroic nanostructures"*. Phys. Rev. Lett., 2005. **94**: p. 197203-4.

96. R. Ramesh and N. A. Spaldin, *"Multiferroics: progress and prospects in thin films"*. Nat. Mater., 2007. **6**: p. 21-29.

97. F. Zavaliche, et al., *"Electric field-induced magnetization switching in epitaxial columnar nanostructures"*. Nano Lett., 2005. **5**: p. 1793-1796.

98. F. Zavaliche, et al., *"Electrically assisted magnetic recording in multiferroic nanostructures"*. Nano Lett., 2007. **7**: p. 1586-1590.

99. C. Y. Deng, et al., *"Magnetic-electric properties of epitaxial multiferroic $NiFe_2O_4$-$BaTiO_3$ heterostructure"*. J. Appl. Phys., 2007. **102**: p. 074114-5.

100. K. Srinivas, et al., *"Electromechanical coefficients of magnetoelectric PZT-$CoFe_2O_4$ composite"*. Mod. Phys. Lett. B, 2000. **14**: p. 663-674.

101. H. M. Zheng, et al., *"Self-assembled growth of $BiFeO_3$-$CoFe_2O_4$ nanostructures"*. Adv. Mater., 2006. **18**: p. 2747-2752.

102. G. C. Sih and Z. F. Song, *"Magnetic and electric poling effects associated with crack growth in $BaTiO_3$-$CoFe_2O_4$ composite"*. Theor. Appl. Fract. Mech., 2003. **39**: p. 209-227.

103. H. P. Zhou, et al., *"Flower-like $Pb(Zr_{0.52}Ti_{0.48})O_3$ nanoparticles on the $CoFe_2O_4$ seeds"*. J. Cryst. Growth, 2008. **310**: p. 508-512.

104. S. H. Xie, et al., *"Multiferroic $CoFe_2O_4$-$Pb(Zr_{0.52}Ti_{0.48})O_3$ nanofibers by electrospinning"*. Appl. Phys. Lett., 2008. **92**: p. 062901-3.

105. N. Ortega, et al., *"Maxwell-Wagner space charge effects on the $Pb(Zr,Ti)O_3$-$CoFe_2O_4$ multilayers"*. Appl. Phys. Lett., 2007. **91**: p. 102902-3.

106. N. Ortega, et al., *"Impedance spectroscopy of multiferroic $PbZr_xTi_{1-x}O_3/CoFe_2O_4$ layered thin films"*. Phys. Rev. B, 2008. **77**: p. 014111-10.

107. M. Liu, et al., *"A modified sol-gel process for multiferroic nanocomposite films"*. J. Appl. Phys., 2007. **102**: p. 083911-3.

108. K. S. Chang, et al., *"Exploration of artificial multiferroic thin-film heterostructures using composition spreads"*. Appl. Phys. Lett., 2004. **84**: p. 3091-3093.

109. L. Li, Y. Q. Lin, and X. M. Chen, *"$CoFe_2O_4/Pb(Zr_{0.52}Ti_{0.48})O_3$ disk-ring magnetoelectric composite structures"*. J. Appl. Phys., 2007. **102**: p. 064103-4.

110. Z. X. Pan, et al., *"Directed fabrication of radially stacked multifunctional oxide heterostructures using soft electron-beam lithography"*. Small, 2006. **2**: p. 274-280.

111. L. Q. Weng, et al., *"Synthesis of lead zirconate titanate-cobalt ferrite magnetoelectric particulate composites via an ethylenediaminetetraacetic acid-citrate gel process"*. Scr. Mater., 2007. **56**: p. 465-468.

112. Z. H. Hua, et al., *"Sol-gel template synthesis and characterization of magnetoelectric $CoFe_2O_4/Pb(Zr_{0.52}Ti_{0.48})O_3$ nanotubes"*. Mater. Chem. Phys., 2008. **107**: p. 541-546.

113. J. X. Zhang, et al., *"A novel nanostructure and multiferroic properties in $Pb(Zr_{0.52}Ti_{0.48})O_3/CoFe_2O_4$ nanocomposite films grown by pulsed-laser deposition"*. J. Phys. D, 2008. **41**: p. 235405-7.

114. C. H. Sim, Z. Z. Pan, and J. Wang, *"Residual stress and magnetic behavior of multiferroic $CoFe_2O_4/Pb(Zr_{0.52}Ti_{0.48})O_3$ thin films"*. J. Appl. Phys., 2009. **105**: p. 084113-7.

115. A. R. Iordan, et al., *"In situ preparation of $CoFe_2O_4$-$Pb(Zr,Ti)O_3$ multiferroic composites by gel-combustion technique"*. J. Eur. Ceram. Soc., 2009. **29**: p. 2807-2813.

116. J. X. Zhang, J. Y. Dai, and H. L. W. Chan, *"Interfacial engineering and coupling of electric and magnetic properties in*

$Pb(Zr_{0.53}Ti_{0.47})O_3/CoFe_2O_4$ multiferroic epitaxial multilayers". J. Appl. Phys., 2010. **107**: p. 104105-8.

117. G. H. Haertling, *"Ferroelectric ceramics: History and technology"*. J. Am. Ceram. Soc., 1999. **82**: p. 797-818.

118. B. Jaffe, W. R. Cook, and H. Jaffe, *"Piezoelectric Ceramics"*. 1971: London.

119. Glodman, A., *Handbook of Modern Ferromagnetic Materials*. 1999: Kluwer Academic Publishers.

120. T. Yamamoto, et al., *"Microstructures and dielectric properties at the morphotropic phase boundry (MPB) of $PbTiO_3$-$PbZrO_3$ system"*. Ferroelectr., 1988. **81**: p. 1295-1298.

121. W. G. Liu and W. G. Zhu, *"Preparation and orientation control of $Pb_{1.1}(Zr_{0.3}Ti_{0.7})O_3$ thin films by a modified sol-gel process"*. Mater. Lett., 2000. **46**: p. 239-243.

122. A. Niazi, P. Poddar, and A. K. Rastogi, *"A precision, low-cost vibrating sample magnetometer"*. Curr. Sci., 2000. **79**: p. 99-109.

123. M. Dawber, K. M. Rabe, and J. F. Scott, *"Physics of thin-film ferroelectric oxides"*. Rev. Mod. Phys., 2005. **77**: p. 1083-1130.

124. M. E. Lines and A. M. Glass, *"Principles and Applications of Ferroelectrics and Related materials"*. 1967, Clarendon, Oxford.

125. C. Brunetti and R. W. Curtis, *"Printed-circuit techniques"*. Proc. IRE, 1948. **36**: p. 121-161.

126. S. D. Sathaye, et al., *"Modification of spin coating method and its application to grow thin films of cobalt ferrite"*. J. Mater. Sci., 2003. **38**: p. 29-33.

127. J. G. Lee, et al., *"Magnetic properties of $CoFe_2O_4$ thin films prepared by a sol-gel method"*. J. Appl. Phys., 1998. **84**: p. 2801-2804.

128. I. H. Gul and A. Maqsood, *"Structural, magnetic and electrical properties of cobalt ferrites prepared by the sol-gel route"*. J. Alloys Compd., 2008. **465**: p. 227-231.

129. W. Chen, et al., *"Ferromagnetic, ferroelectric and dielectric properties of $Pb(Zr_{0.53}Ti_{0.47})O_3/CoFe_2O_4$ multiferroic composite thick films"*. J. Phys. D, 2009. **42**: p. 075421-5.

130. J. W. Zhai, et al., *"Enhanced dielectric tunability properties of $Ba(Zr_xTi_{1-x})O_3$ thin films using seed layers on $Pt/Ti/SiO_2/Si$ substrates"*. Ceram. Int., 2008. **34**: p. 905-910.

131. S. G. Lee, *"Effects of sol infiltration on the screen-printed lead zirconate titanate thick films"*. Mater. Lett., 2007. **61**: p. 1982-1985.

132. B. D. Stojanovic, et al., *"Screen printed PLZT thick films prepared from nanopowders"*. J. Eur. Ceram. Soc., 2007. **27**: p. 4359-4362.

133. Z. H. Wang, et al., *"Dense PZT thick films derived from sol-gel based nanocomposite process"*. Mater. Sci. Eng. B, 2003. **99**: p. 56-62.

134. N. Ponpandian and A. Narayanasamy, *"Influence of grain size and structural changes on the electrical properties of nanocrystalline zinc ferrite"*. J. Appl. Phys., 2002. **92**: p. 2770-2778.

135. V. Sepelak, et al., *"Structural disorder in the high-energy milled magnesium ferrite"*. J. Appl. Phys., 2000. **88**: p. 5884-5893.

136. A. Dias and R. L. Moreira, *"Chemical, mechanical and dielectric properties after sintering of hydrothermal nickel-zinc ferrites"*. Mater. Lett., 1999. **39**: p. 69-76.

137. N. Sivakumar, et al., *"Dielectric relaxation behaviour of nanostructured Mn-Zn ferrite"*. J. Phys. D, 2008. **41**: p. 245001-5.

138. N. Sivakumar, et al., *"Influence of thermal annealing on the dielectric properties and electrical relaxation behaviour in nanostructured $CoFe_2O_4$ ferrite"*. J. Phys. Condens. Matter, 2007. **19**: p. 386201-11.

139. H. Perron, et al., *"Structural investigation and electronic properties of the nickel ferrite $NiFe_2O_4$: a periodic density functional theory approach"*. J. Phys. Condens. Matter, 2007. **19**: p. 346219-10.

140. Y. Kitamoto, et al., *"Co ferrite films with excellent perpendicular magnetic anisotropy and high coercivity deposited at low temperature"*. J. Appl. Phys., 1999. **85**: p. 4708-4710.

141. W. F. J. Fontijn, et al., *"A consistent interpretation of the magneto-optical spectra of spinel type ferrites"*. J. Appl. Phys., 1999. **85**: p. 5100-5105.

142. B. G. Toksha, et al., *"Structural investigations and magnetic properties of cobalt ferrite nanoparticles prepared by sol-gel auto combustion method"*. Solid State Commun., 2008. **147**: p. 479-483.

143. S. Komarneni, et al., *"Microwave-hydrothermal synthesis of nanophase ferrites"*. J. Am. Ceram. Soc., 1998. **81**: p. 3041-3043.

144. V. V. Paike, et al., *"Synthesis of spinel $CoFe_2O_4$ via the co-precipitation method using tetraalkyl ammonium hydroxides as precipitating agents"*. J. Am. Ceram. Soc., 2007. **90**: p. 3009-3012.

145. S. D. Bhame and P. A. Joy, *"Effect of sintering conditions and microstructure on the magnetostrictive properties of cobalt ferrite"*. J. Am. Ceram. Soc., 2008. **91**: p. 1976-1980.

146. I. H. Gul, W. Ahmed, and A. Maqsood, *"Electrical and magnetic characterization of nanocrystalline Ni-Zn ferrite synthesis by co-precipitation route"*. J. Magn. Magn. Mater., 2008. **320**: p. 270-275.

147. M. George, et al., *"Finite size effects on the electrical properties of sol-gel synthesized $CoFe_2O_4$ powders: deviation from Maxwell-Wagner theory and evidence of surface polarization effects"*. J. Phys. D, 2007. **40**: p. 1593-1602.

148. W. Chen, et al., *"Enhanced ferroelectric and dielectric properties of $CoFe_2O_4$-$Pb(Zr_{0.53}Ti_{0.47})O_3$ multiferroic composite thick films"*. J. Am. Ceram. Soc., 2010. **93**: p. 796-799.

149. C. G. Zhong, et al., *"Thickness and magnetic field dependence of ferroelectric properties in multiferroic $BaTiO_3$-$CoFe_2O_4$ nanocomposite films"*. J. Appl. Phys., 2009. **105**: p. 044901-6.

150. I. H. Gul, et al., *"Structural, magnetic and electrical properties of $Co_{1-x}Zn_xFe_2O_4$ synthesized by co-precipitation method"*. J. Magn. Magn. Mater., 2007. **311**: p. 494-499.

151. W. Chen, et al., *"Preparation and characterization of $Pb(Zr_{0.53}Ti_{0.47})O_3/CoFe_2O_4$ composite thick films by hybrid sol-gel processing"*. Mater. Sci. Eng. B, 2009. **162**: p. 47-52.

152. N. C. Pramanik, et al., *"Preparation and magnetic properties of the $CoFe_2O_4$ thin films on Si substrate by sol-gel technique"*. J. Mater. Sci., 2005. **40**: p. 4169-4172.

153. A. Lisfi and C. M. Williams, *"Magnetic anisotropy and domain structure in epitaxial $CoFe_2O_4$ thin films"*. J. Appl. Phys., 2003. **93**: p. 8143-8145.

154. Z. L. Wang, et al., *"Preparation of ferrite MFe_2O_4 (M =Co,Ni) ribbons with nanoporous structure and their magnetic properties"*. J. Phys. Chem. B, 2008. **112**: p. 11292-11297.

155. J. H. Yin, et al., *"Nanocrystalline Co-ferrite films with high perpendicular coercivity"*. Appl. Phys. Lett., 2006. **88**: p. 162502-3.

156. J. G. Lee, et al., *"Magnetic properties of $CoFe_2O_4$ powders and thin films grown by a sol-gel method"*. J. Magn. Magn. Mater., 1998. **177**: p. 900-902.

157. A. Srivastava, A. Garg, and F. D. Morrison, *"Impedance spectroscopy studies on polycrystalline $BiFeO_3$ thin films on Pt/Si substrates"*. J. Appl. Phys., 2009. **105**: p. 054103-6.

158. J. G. Wu and J. Wang, *"Multiferroic behavior and impedance spectroscopy of bilayered $BiFeO_3/CoFe_2O_4$ thin films"*. J. Appl. Phys., 2009. **105**: p. 124107-6.

159. N. Hirose and A. R. West, *"Impedance spectroscopy of undoped $BaTiO_3$ ceramics"*. J. Am. Ceram. Soc., 1996. **79**: p. 1633-1641.

160. A. R. James, C. Prakash, and G. Prasad, *"Structural properties and impedance spectroscopy of excimer laser ablated Zr substituted $BaTiO_3$ thin films"*. J. Phys. D, 2006. **39**: p. 1635-1641.

161. N. Ponpandian, P. Balaya, and A. Narayanasamy, *"Electrical conductivity and dielectric behaviour of nanocrystalline $NiFe_2O_4$ spinel"*. J. Phys. Condens. Matter, 2002. **14**: p. 3221-3237.

162. N. Sivakumar, et al., *"Grain size effect on the dielectric behavior of nanostructured $Ni_{0.5}Zn_{0.5}Fe_2O_4$"*. J. Appl. Phys., 2007. **101**: p. 084116-6.

163. F. D. Lin, Y. J. Wang, and M. Lonergan, *"Ion transport in polyacetylene ionomers"*. J. Appl. Phys., 2008. **104**: p. 103517-8.

164. M. M. Ahmad, Y. Yamane, and K. Yamada, *"Structure, ionic conduction, and giant dielectric properties of mechanochemically synthesized $BaSnF_4$"*. J. Appl. Phys., 2009. **106**: p. 074106-7.

165. S. Dutta, et al., *"Microstructural studies of $(PbLa)(ZrTi)O_3$ ceramics using complex impedance spectroscopy"*. J. Appl. Phys., 2004. **96**: p. 1607-1613.

166. S. M. Abbas, et al., *"Electromagnetic and microwave absorption properties of $(Co^{2+}$-$Si^{4+})$ substituted barium hexaferrites and its polymer composite"*. J. Appl. Phys., 2007. **101**: p. 074105-6.

167. S. M. Patange, et al., *"Electrical and magnetic properties of Cr^{3+} substituted nanocrystalline nickel ferrite"*. J. Appl. Phys., 2009. **106**: p. 023914-7.

168. A. K. Jonscher, *"The "Universal" dielectric response"*. Nature, 1977. **267**: p. 673-679.

169. K. Funke, *"Jump relaxation in solid electrolytes"*. Prog. Solid State Chem., 1993. **22**: p. 111-195.

170. M. Marczak and H. Diesinger, *"Traveling wave dielectrophoresis micropump based on the dispersion of a capacitive electrode layer"*. J. Appl. Phys., 2009. **105**: p. 124511-7.

171. A. W. Imre, M. Schonhoff, and C. Cramer, *"Unconventional scaling of electrical conductivity spectra for PSS-PDADMAC polyelectrolyte complexes"*. Phys. Rev. Lett., 2009. **102**: p. 255901-4.

172. B. L. Ahn, et al., *"Influence of precursor solution coating parameters on structural and dielectric properties of PZT thick films".* J. Mater. Sci., 2008. **43**: p. 3408-3411.

173. J. Perez, et al., *"Electrical properties of lead zirconate titanate thick films prepared by hybrid sol-gel method with multiple infiltration steps".* Mater. Phys. Chem., 2007. **101**: p. 280-284.

174. J. X. Zhang, et al., *"Magnetoelectric coupling in $CoFe_2O_4/SrRuO_3/Pb(Zr_{0.52}Ti_{0.48})O_3$ heteroepitaxial thin film structure".* Appl. Phys. Lett., 2008. **92**: p. 022901-3.

175. W. Huang, et al., *"Strain induced magnetic anisotropy in highly epitaxial $CoFe_2O_4$ thin films".* Appl. Phys. Lett., 2006. **89**: p. 262506-3.

176. H. Kozuka, et al., *"Crack-free, thick ceramic coating films via non-repetitive dip-coating using polyvinylpyrrolidone as stress-relaxing agent".* J. Sol-Gel Sci. Technol., 2000. **19**: p. 205-209.

177. G. T. Park, et al., *"Piezoelectric and ferroelectric properties of 1-um-thick lead zirconate titanate film fabricated by a double-spin-coating process".* Appl. Phys. Lett., 2004. **85**: p. 2322-2324.

178. A. Yamano and H. Kozuka, *"Effects of the heat-treatment conditions on the crystallographic orientation of $Pb(Zr,Ti)O_3$ thin films prepared by polyvinylpyrrolidone-assisted sol-gel method".* J. Am. Ceram. Soc., 2007. **90**: p. 3882-3889.

179. BASF, *Polyvinylpyrrolidone Center*, P.K. Properties, Editor. 2011.

180. F. X. Cheng, et al., *"Chemical synthesis and magnetic study of nanocrystalline thin films of cobalt spinel ferrites".* Solid State Commun., 1998. **107**: p. 471-476.

181. C. C. Lee and J. M. Wu, *"Studies on leakage mechanisms and electrical properties of doped $BiFeO_3$ films"*. Electrochem. Solid-State Lett., 2007. **10**: p. G58-G61.

182. J. S. Lee and S. K. Joo, *"Analysis of grain-boundary effects on the electrical properties of $Pb(Zr,Ti)O_3$ thin films"*. Appl. Phys. Lett., 2002. **81**: p. 2602-2604.

183. I. B. Misirlioglu, et al., *"Space charge contribution to the apparent enhancement of polarization in ferroelectric bilayers and multilayers"*. Appl. Phys. Lett., 2007. **91**: p. 022911.

184. C. W. Ahn, et al., *"Enhanced ferroelectric properties of $LiNbO_3$ substituted $Na_{0.5}K_{0.5}NbO_3$ lead-free thin films grown by chemical solution deposition"*. Appl. Phys. Lett., 2008. **93**: p. 212905-3.

185. G. D. Hu, et al., *"Low leakage current and enhanced ferroelectric properties of Ti and Zn codoped $BiFeO_3$ thin film"*. Appl. Phys. Lett., 2008. **92**: p. 192905-3.

186. Z. H. Wang, J. M. Miao, and W. G. Zhu, *"Piezoelectric thick films and their application in MEMS"*. J. Eur. Ceram. Soc., 2007. **27**: p. 3759-3764.

187. J. F. Scott, *"Ferroelectrics go bananas"*. J. Phys. Conden. Matt., 2008. **20**: p. 021001-2.

188. A. Khodorov, et al., *"Impedance spectroscopy study of a compositionally graded lead zirconate titanate structure"*. J. Appl. Phys., 2007. **102**: p. 114109-7.

189. S. Y. Tan, et al., *"Synthesis and characterization of composite $MgFe_2O_4$-$BaTiO_3$ multiferroic system"*. J. Appl. Phys., 2008. **103**: p. 094105-4.

190. L. Zhang and Z. J. Tang, *"Polaron relaxation and variable-range-hopping conductivity in the giant-dielectric-constant material $CaCu_3Ti_4O_{12}$"*. Phys. Rev. B, 2004. **70**: p. 174306-6.

191. F. D. Morrison, D. C. Sinclair, and A. R. West, *"Characterization of lanthanum-doped barium titanate ceramics using impedance spectroscopy"*. J. Am. Ceram. Soc., 2001. **84**: p. 531-538.

192. S. R. Elliott, *"Ac conduction in amorphous-chalcogenide and pnictide semiconductors"*. Adv. Phys., 1987. **36**: p. 135-218.

193. C. Leon, et al., *"Origin of constant loss in ionic conductors"*. Phys. Rev. Lett., 2001. **86**: p. 1279-1282.

194. W. Chen, et al., *"Multiferroic behavior and magnetoelectric effect in $CoFe_2O_4$/$Pb(Zr_{0.53}Ti_{0.47})O_3$ thick films"*. Solid State Commun., 2010. **150**: p. 271-274.

195. M. M. Kumar, et al., *"An experimental setup for dynamic measurement of magnetoelectric effect"*. Bull. Mater. Sci., 1998. **21**: p. 251-255.